Computational Design, Fabrication, and Characterization of Microarchitectured Solid Oxide Fuel Cells with Improved Energy Efficiency

A Dissertation
Presented to
The Academic Faculty

by

Chan Yoon

In Partial Fulfillment
of the Requirements for the Degree
Doctor of Philosophy in the
George W. Woodruff School of Mechanical Engineering

Georgia Institute of Technology
August 2010

Computational Design, Fabrication, and Characterization of Microarchitectured Solid Oxide Fuel Cells with Improved Energy Efficiency

Approved by:

Dr. Suman Das, Advisor
School of Mechanical Engineering
Georgia Institute of Technology

Dr. William Wepfer
School of Mechanical Engineering
Georgia Institute of Technology

Dr. Suresh Sitaraman
School of Mechanical Engineering
Georgia Institute of Technology

Dr. Meilin Liu
School of Materials Science and Engineering
Georgia Institute of Technology

Dr. John Halloran
School of Materials Science and Engineering
University of Michigan

Date Approved: June 16, 2010

To my family

ACKNOWLEDGEMENTS

I would like to thank my faculty advisor, Dr. Suman Das, for his valuable guidance, direction, support, and faith during this rather long journey. I would also like to thank my thesis committee members, Dr. William Wepfer, Dr. Suresh Sitaraman, Dr. Meilin Liu, and Dr. John Halloran, for their constant consideration and assistance. Especially, Dr. John Halloran proposed the idea and concept of microarchitectured solid oxide fuel cells. Dr. Meilin Liu and Dr. Mingfei Liu assisted me to perform solid oxide fuel cell fabrication and performance test. I really thank them for great help.

To Dr. Yuan Dajun and Dr. Rui Guo, I am so thankful to them for helping me use femtosecond laser. I am very thankful to my labmates, who always encouraged and helped me in my research.

To both my wife Hyejin and my daughter Hannah, I extend my thanks for their patience, understanding and emotional support. I would like to thank my parents, Geun and Eunsoo, for their support and dedication. My father and mother have always put me first in their lives, and have been a constant source of emotional support throughout the years of my education. To my sister, Jin, thank her for love, patience, and encouragement.

TABLE OF CONTENTS

LIST OF TABLES

LIST OF FIGURES

SUMMARY

Electrodes in a solid oxide fuel cell (SOFC) must possess both adequate porosity and electronic conductivity to perform their functions in the cell. They must be porous to permit rapid mass transport of reactant and product gases and sufficiently conductive to permit efficient electron transfer. However, it is nearly impossible to simultaneously control porosity and conductivity using conventional design and fabrication techniques. In this dissertation, computational design and performance optimization of microarchitectured SOFCs is first investigated in order to achieve higher power density and thus higher efficiency than currently attainable in state-of-the-art SOFCs. This involves a coupled multiphysics simulation of mass transport, electrochemical charge transfer reaction, and current balance as a function of SOFC microarchitecture. Next, the fabrication of microarchitectured SOFCs consistent with the computational designs is addressed based on anode-supported SOFC button cells using the laser ablation technique. Finally, the performance of a fabricated SOFC unit cell is characterized and compared against the performance predicted by the computational model. The results show that the performance of microarchitectured SOFCs was improved against the baseline structure and measured experimental data were well matched to simulation results.

CHAPTER 1

INTRODUCTION

The objective of this chapter is to introduce the basic concept of a solid oxide fuel cell (SOFC), fabrication techniques for SOFCs, SOFC performance, and literature survey on microarchitectures in SOFC electodes. Section 1.5 provides an outline for this dissertation.

1.1. The Solid Oxide Fuel Cell (SOFC)

A solid oxide fuel cell (SOFC) is an energy conversion device which converts the chemical energy of gaseous fuels directly into electrical energy [1]. In principle, the SOFC consists of three main components: an anode also called the fuel electrode, a cathode also called the air electrode, and an electrolyte.

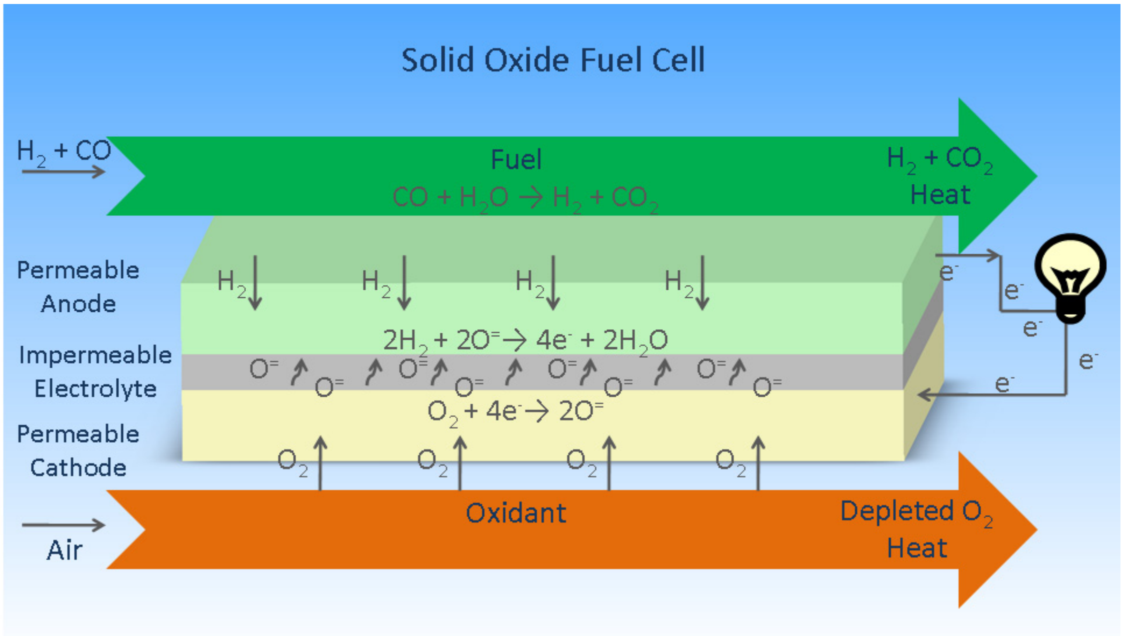

Figure 1.1 Operating principle of a SOFC.

The cell is constructed with two porous electrodes which sandwich an electrolyte, as shown in Figure 1.1. Air flows along the cathode. At the cathode-electrolyte interface, molecular oxygen is reduced to oxygen ions using electrons supplied from an external circuit. The oxygen ions diffuse into the electrolyte material and migrate to the other side of the cell where they encounter the anode. Hydrogen fuel is fed into the anode of the fuel cell. By burning fuel containing hydrogen on one side of the electrolyte, the concentration of oxygen is dramatically reduced. Since there is a large amount of oxygen ions on the other side of the electrolyte, an oxygen concentration gradient is created across the electrolyte, which attracts oxygen ions from the cathode to the anode. The oxygen ions encounter the fuel at the anode-electrolyte interface and react catalytically, giving off water, carbon dioxide, heat, and most importantly electrons. The electrons are transported through the anode to the external circuit and back to the cathode, providing a source of useful electrical energy in an external circuit. The operating temperature of typical SOFCs is currently between 600 and 1000°C.

The electrochemically active components of SOFCs have multifunctional performance requirements. The electrolyte should be a fully dense ionic conductor to prevent short circuiting of the reacting gases through it, and it must be thin to minimize resistive losses in the cell [1]. The anode and cathode layers of a SOFC must possess both electronic conductivity and porosity to allow electron transport between the electrode-electrolyte interface and the external circuit, and to facilitate mass transport of reactant and product gases. The anode structure is typically fabricated with a porosity of 20% to 40%. Similar to the anode, the cathode is a porous structure with a porosity of 20% to 40%. Furthermore, both the anode and cathode must be electronically conductive since the anode should easily transport electrons from the anode-electrolyte interface to the open circuit, while the cathode should transport electrons from the open circuit to the cathode-electrolyte interface.

The material most often used as the electrolyte is yttria-stabilized zirconia (YSZ) due to its chemical and mechanical stability over a wide range of oxygen partial pressures and temperatures. Other alternative electrolytes are Samarium-doped ceria (SDC), and Gadolinium-doped ceria (GDC). The anode must be electronically conductive, be able to catalyze the oxidation of the fuel, and have a similar coefficient of thermal expansion (CTE) to that of the electrolyte. Anodes are typically fabricated from composite powder mixtures of electrolyte material (YSZ) and nickel-oxide NiO (the nickel oxide subsequently gets reduced to nickel metal during first start-up of the fuel cell operation), which serves to prevent sintering of the metal particles and to provide a CTE comparable to that of the electrolyte. Nickel provides electronic conductivity and catalytic activity. The cathode is typically an oxide material that catalyses the reduction of oxygen, and facilitates the transport of the ionic species to the electrolyte. Because most metals are oxidized in the presence of air at high temperature, the required cathode properties are typically achieved with lanthanum manganite ($LaMnO_3$), a p-type perovskite. Typically, it is doped with rare earth elements such as Strontium (Sr), Cerium (Ce), and Praseodymium (Pr) to enhance its electronic conductivity. Most often, it is doped with Strontium and referred to as LSM. Finally, the cathode material must have a coefficient of thermal expansion (CTE) that is a reasonable match with that of the electrolyte. The triple phase boundary (TPB) of a fuel cell is the area of contact between the three phases necessary for electrochemical reactions at the electrode-electrolyte interface: the ion conducting phase, the electron conducting phase, and the gas phase. A good fuel cell maximizes the TPB area, allowing the reaction to occur in more sites, thus maximizing current flow. In practice, this is achieved by the use of composite structures containing both ionically and electronically conducting materials.

Carbon monoxide (CO) and hydrocarbons such as methane (CH4) can be used as fuels in SOFCs. It is feasible that the water-gas shift involving CO ($CO + H_2O \rightarrow H_2 + CO_2$) and steam reforming of CH_4 ($CH_4 + H_2O \rightarrow 3H_2 + CO$) could occur at the high temperature environment of SOFCs to produce H_2 that is easily oxidized at the anode. The direct oxidation of CO in fuel cells is also well established [2].

Two popular design configurations for SOFCs have emerged: a planar design (Figure 1.2) and a tubular design (Figure 1.3). In the planar design, the components are assembled in flat stacks, with air and fuel flowing through channels built into the cathode and anode. In the tubular design, components are assembled in the form of a hollow tube, with the cell constructed in layers around a tubular cathode; air flows through the inside of the tube and fuel flows around the exterior.

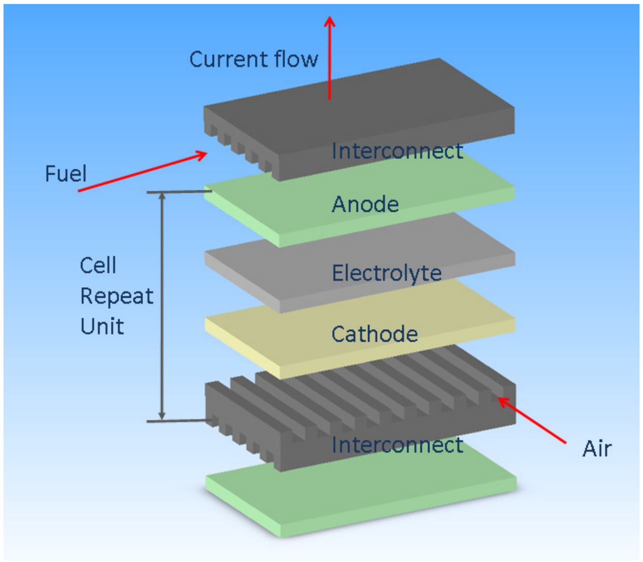

Figure 1.2 Configuration for a planar design SOFC.

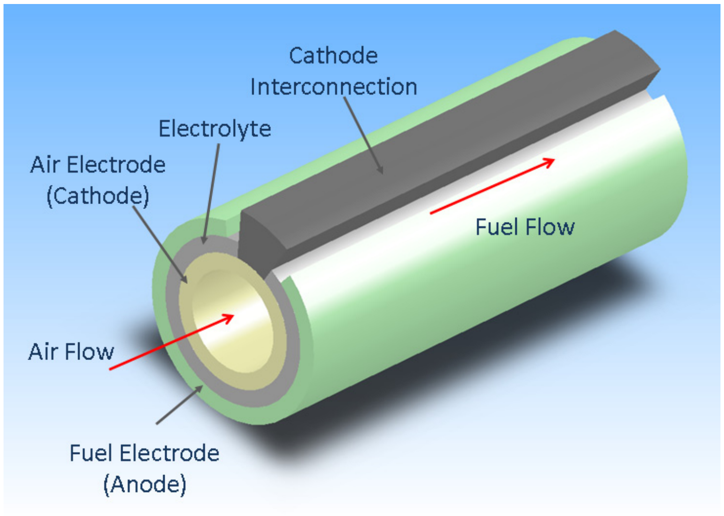

Figure 1.3 Configuration for a tubular design SOFC.

The planar-type SOFC is easier to stack in order to enhance the efficiency of the system, while tubular SOFC designs offer advantages over planar designs with good thermal shock resistance, high mechanical strength, easy sealing, and high volume manufacturing ability [3-8]. A disadvantage of the tubular design is the lower volumetric power packing density. As a result, for a given stack power, planar SOFC stacks will be smaller than tubular SOFC stacks.

1.2. Advantages of a SOFC over the Other Fuel Cells

The generation of energy by clean, efficient and environmentally-friendly means is one of the major challenges faced by the world. Fuel cells convert gaseous fuels (hydrogen, natural gas, gasified coal) via an electrochemical process directly into electricity, and are efficient and environmentally clean, since no combustion is required. Fuel cells are not constrained by the maximum Carnot cycle efficiency as are combustion engines, and pollutant output from fuel cells is significantly lower than that found in conventional technologies. A fuel cell operates like a battery, but does not need to be recharged, and it continuously produces power, when supplied with fuel and oxidant [9].

Attempts to develop fuel cells as power sources have been made over many years. Fuel cells are generally classified by the chemical characteristics of the electrolyte used as the ionic conductor in the cell, as shown in Table 1.1. The first two types (PEMFC and PAFC) are characterized by their low to medium temperature of operation (60-200°C), and their relatively low electrical generation efficiencies (40-50% when operated on readily available fuels such as methanol and hydrocarbons, 50% when using pure hydrogen fuel). The latter two types (MCFC and SOFC) are characterized by their high temperature of operation (600-1000°C), their ability to utilize methane directly in the fuel cell, and thus their high inherent generation efficiency (45-60% for common fuels such as natural gas, 90% with heat recovery) [10].

Table 1.1 Types of fuel cells [10].

	Polymer Electrolyte Membrane Fuel Cell (PEMFC)	Phosphoric Acid Fuel Cell (PAFC)	Molten Carbonate Fuel Cell (MCFC)	Solid Oxide Fuel Cell (SOFC)
Electrolyte	Ion exchange membrane	Liquid phosphoric acid	Molten carbonate salt	Ceramic as stabilized zirconia and doped perovskite
Operating Temperature	60-100°C	150-200°C	630-650°C	600-1000°C
Fuel	Less pure hydrogen from hydrocarbons or methanol	Hydrogen from hydrocarbons and alcohol	Hydrogen, carbon monoxide, natural gas, propane, marine diesel	Natural gas or propane
Oxidant	O_2/Air	O_2/Air	CO_2/O_2/Air	O_2/Air
Efficiency	40-50%	40-50%	50-60%	45-60%

A Solid Oxide Fuel Cell (SOFC) has several advantages over the other types of fuel cells for the following reasons. SOFCs are the most efficient (fuel input to electricity output) fuel cell electricity generators currently being developed world-wide. They are flexible in the choice of fuel such as carbon-based fuels like natural gas. In addition, SOFCs are most suited to applications in the distributed generation (i.e. stationary power) market since their high conversion efficiency provides the greatest benefit when fuel costs are higher, due to long fuel delivery systems to customer premises. SOFCs have a modular and solid state construction and do not present any moving parts; thereby, they are quiet enough to be installed indoors. The high operating temperature of SOFCs produces high quality heat by-products which can be used for co-generation, or for use in combined cycle applications. Furthermore, SOFCs do not contain noble metals that could be problematic in high volume manufacture due to resource availability and price issues. SOFCs do not have problems with electrolyte management (liquid electrolytes, for example, are corrosive and difficult to handle). SOFCs have extremely low emissions by eliminating the danger of carbon monoxide in exhaust gases, as any CO produced is converted to CO_2 at the high operating temperature. SOFCs have a potential long life expectancy of more than 40000-80000 h [10].

1.3. Fabrication Techniques for SOFCs

A number of fabrication techniques to produce SOFC components have been investigated. Conventional techniques to fabricate SOFCs includes chemical vapor deposition (CVD), physical vapor deposition (PVD), electrochemical vapor deposition (EVD), electrophoresis deposition (EPD), atmospheric plasma spraying (APS), vacuum plasma spraying (VPS), sputtering, flame coating, laser ablation, sol-gel coat, and ceramic forming techniques such as tape casting, tape calendaring, screen printing, and dry press formation.

1.3.1. Plasma Spraying

Plasma spraying of ceramics is a widely used process. Common applications include applying thermal barrier coatings for engine components and imparting corrosion protection and wear-resistance to pumps and printing presses. It is also used to apply thin coatings with specific insulating or conducting properties to resistors, to apply self-lubricating coatings, and to apply color deposits. Plasma spraying is a one step high temperature process, which may not need to be followed by a separate sintering step. The atmospheric plasma spray process (APS) is the most common variant, conducted under normal atmospheric conditions. Another variant of plasma spraying is conducted in protective environments using vacuum chambers and is referred to as vacuum plasma spraying (VPS). Plasma spraying has been considered as a method for depositing both electrodes and electrolyte layers in SOFCs [11].

The plasma spray process (Figure 1.4) is basically the spraying of molten or heat softened material onto a surface to provide a coating. Material in the form of powder is injected into a very high temperature plasma flame, where it is rapidly heated and accelerated to a high velocity. The hot material impacts on the substrate surface and rapidly cools, forming a coating. This plasma spray process, carried out correctly, is called a "cold process" (relative to the substrate material being coated) as the substrate temperature can be kept low during processing, avoiding damage, metallurgical changes, and distortion to the substrate material. APS is widely used in manufacturing SOFCs, but the operating cost is very high.

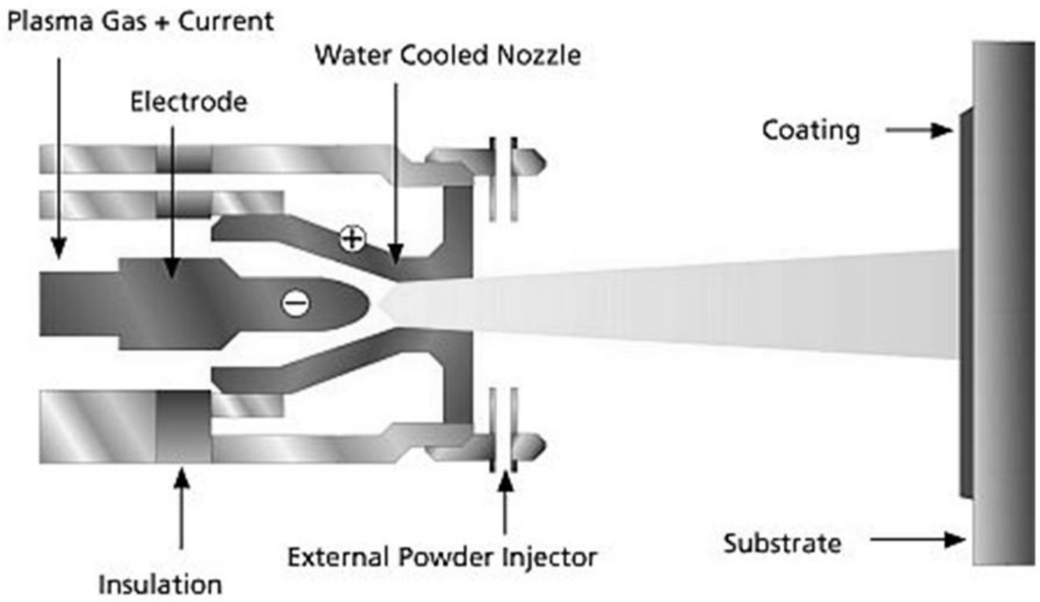

Figure 1.4 Schematic diagram for plasma spraying process (http://www.plasmacoat.co.uk).

1.3.2. Electrochemical Vapor Deposition (EVD)

The process of electrochemical vapor deposition (EVD), shown in Figure 1.5, was developed by Siemens Westinghouse Company. It is the key fabrication technique in the seamless tubular SOFC technology. All layers of tubular SOFCs are made by EVD. Dense layers of YSZ (40µm thick) have been fabricated by EVD on porous substrates [12].

The EVD process, a modified chemical vapor deposition (CVD) technique, involves growing a dense layer of electron- or ion-conducting oxide on a porous substrate by exploiting the electrochemical potential energy as the driving force. An oxide layer is deposited by EVD in two stages: a pore closure CVD stage (stage 1) and a scale growth EVD stage (stage 2) [13]. Stage 2 involves the growth of YSZ over the closed pores by a Wagner oxidation process [14]. The oxide growth arises due to the presence of a large oxygen activity gradient across the substrate. In this stage, H_2O is reduced at the water vapor side of the growing oxide scale to produce oxygen ions. The oxygen ions diffuse through the film to the metal chloride gas phase side since oxygen ions are generally more mobile than metal ions. Under operating conditions of the EVD process, the thickness and uniformity of the layer are affected by the reaction temperature, flow velocity, relative concentrations of steam and metal chloride, and pore size of substrate, which should be strictly controlled [13].

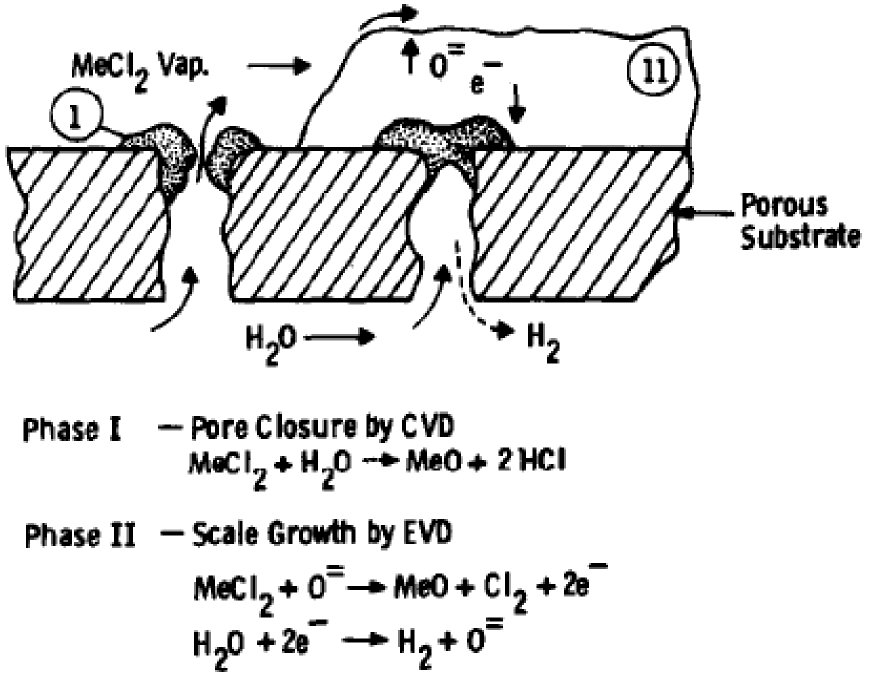

Figure 1.5 Principle of electrochemical vapor deposition [13].

The EVD technology can produce thin and good gas-resistant layers, which have good conduction and coherence between the layers. However, the EVD process must operate at high temperature, more than 1000°C, and requires high vacuum and a suitable substrate. The equipment is complex and needs to be controlled strictly. Therefore, the efficiency is low. It is difficult to manufacture a large-scale product at low cost.

1.3.3. Sol-gel Process

The sol-gel process, shown in Figure 1.6, involves the deposition of a layer from a colloidal dispersion [15]. The sol-gel process is a versatile solution process for making ceramic and glass materials. In general, the sol-gel process involves the transition of a system from a liquid "sol" (mostly colloidal) into a solid "gel" phase.

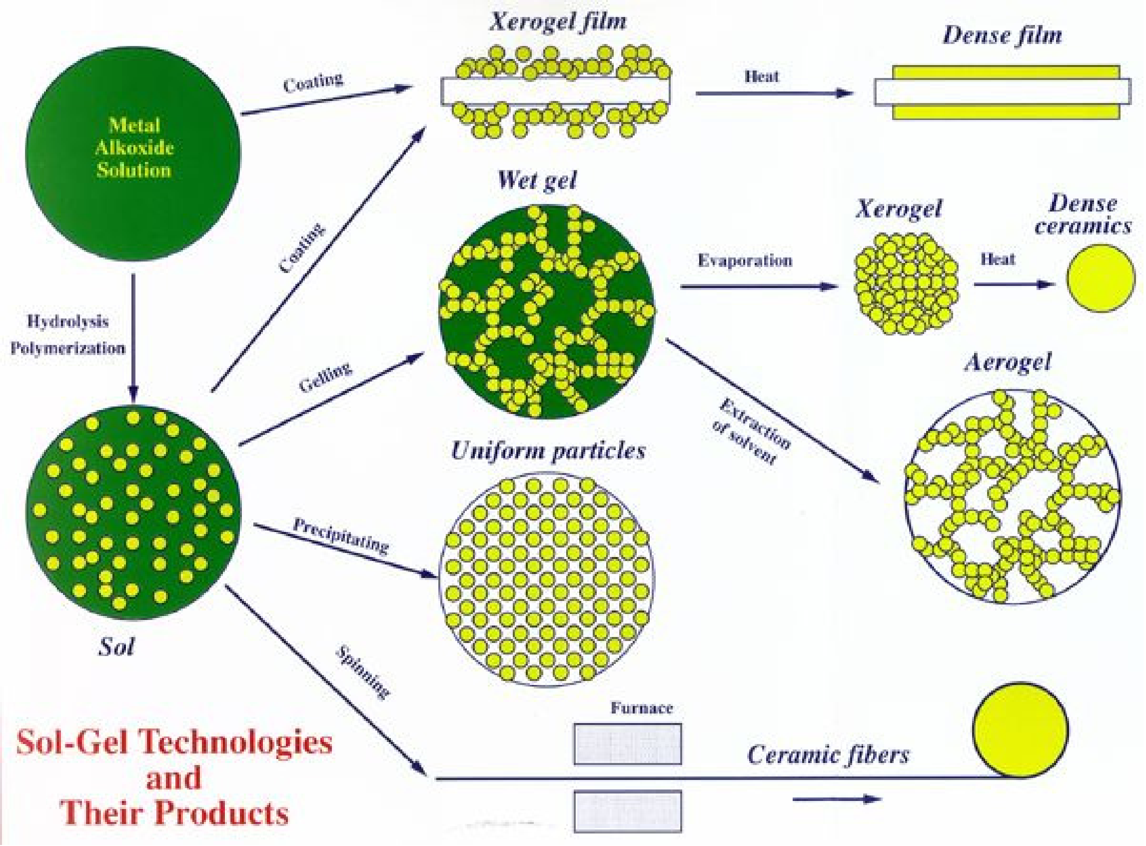

Figure 1.6 Sol-gel technology and their products (http://www.chemat.com).

Applying the sol-gel process, it is possible to fabricate ceramic or glass materials in a wide variety of forms: ultra-fine or spherical shaped powders, thin film coatings, ceramic fibers, microporous inorganic membranes, monolithic ceramics and glasses, or extremely porous aerogel materials.

Thin films can be produced on a piece of substrate by spin-coating or dip-coating. When the sol is cast into a mold, a wet gel will form. With further drying and heat-treatment, the gel is converted into dense ceramic or glass articles. Using the sol-gel technique, YSZ films have been deposited on porous LSM cathode substrates [16].

1.3.4. Ceramic Forming Techniques

All components of SOFCs are typically ceramic materials. An oxide layer is deposited by ceramic forming techniques in four steps: manufacturing suitable powder, preparing the slurries, shaping the layers by tape casting, tape calendaring, or screen printing, and sintering.

Tape casting is a common process for producing thin ceramic sheets or ceramic loaded polymer sheets for use in the electronics industry. Tape casting is commonly used for preparing the "green" or unsintered electrolyte, and often used for preparing the anode and cathode layers as well. Ceramic powder and solvent are mixed to form a slurry, which is treated with various additives and binders, homogenized, and then pumped directly to a tape-casting machine. There the slurry is continuously cast onto the surface of a moving carrier film. The edge of a smooth knife, generally called a doctor blade, spreads the slurry onto the carrier film at a specified thickness, thereby generating a flexible tape. Heat lamps gently evaporate the solvent, and then cut to size with an auto punch or other green-machining device. If needed, multiple layers (cathode, electrolyte, and anode) can be cast on top of one another, laminated together, and then co-sintered in a furnace.

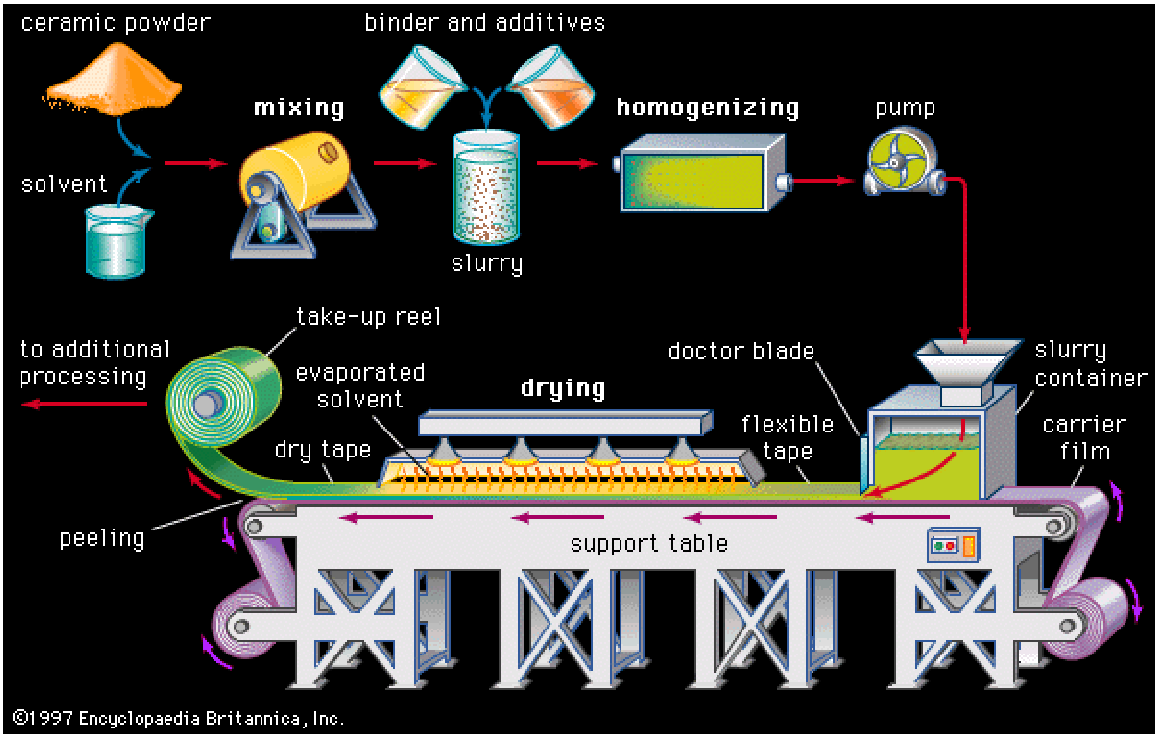

Figure 1.7 Schematic diagram for tape casting process (http://www.britannica.com).

Tape calendaring is a processing method most frequently used in the paper industry and for rubber and plastic sheets. Binders and plasticizers are added to the ceramic oxide to form a doughy consistency (roughly 20 wt% additives). This material is then squeezed between two rollers, forming a thin tape.

Screen printing is an inexpensive method of applying thin layers on a substrate. In many SOFC designs, the anode and cathode layers are screen-printed onto the electrolyte, and the resulting multiple layers are then sintered. Screen printing ink is applied to the substrate by placing a screen over the material. Ink with a paint-like consistency is placed onto the top of the screen. Ink is then forced through the fine mesh openings using a squeegee that is drawn across the screen, applying pressure thereby forcing the ink through the open areas of the screen. Ink will pass through only in areas where no stencil is applied, thus forming an image on the printing substrate.

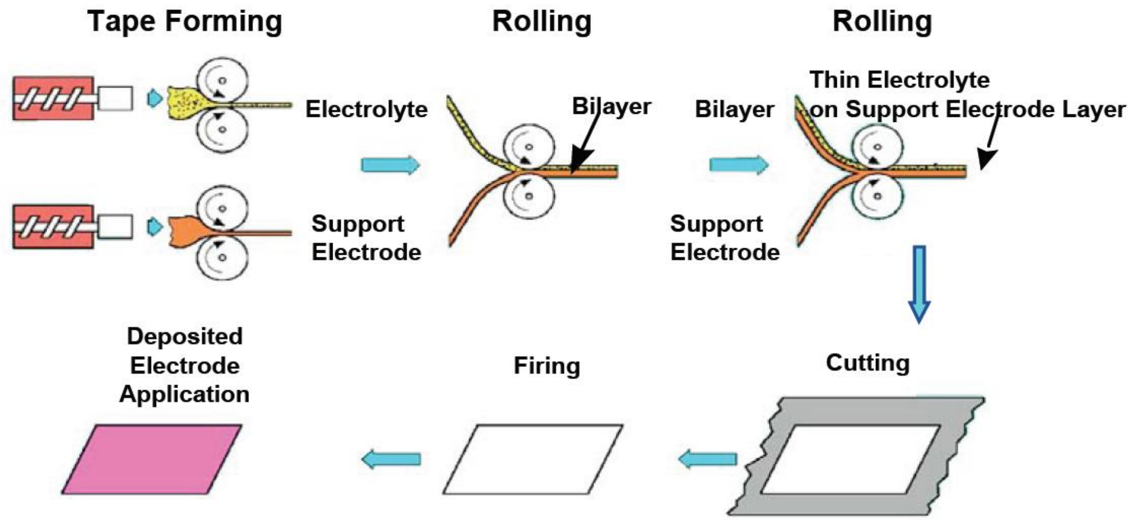

Figure 1.8 Schematic diagram for SOFC fabrication using tape calendaring process [17].

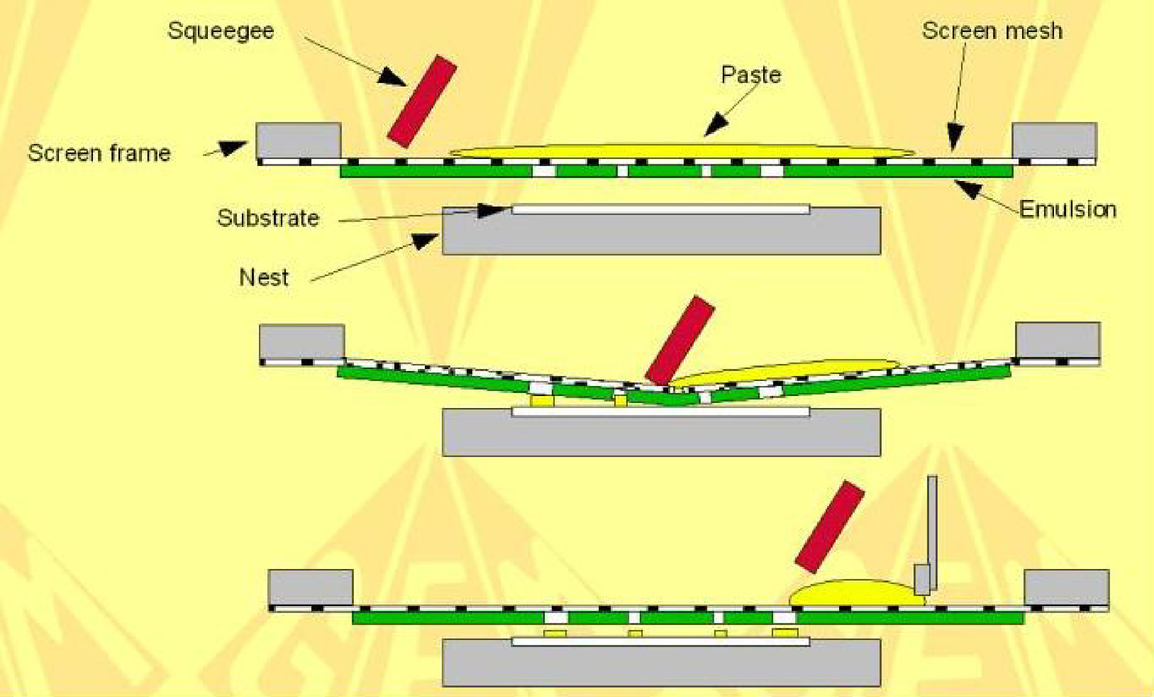

Figure 1.9 Schematic diagram for screen printing process (http://www.g-e-m.com).

1.4. SOFC Performance

A schematic representation of a current-voltage (i-V) curve for a SOFC is shown in Figure 1.10. The open cell voltage is lowered when the cell is loaded, and a typical i-V curve is obtained.

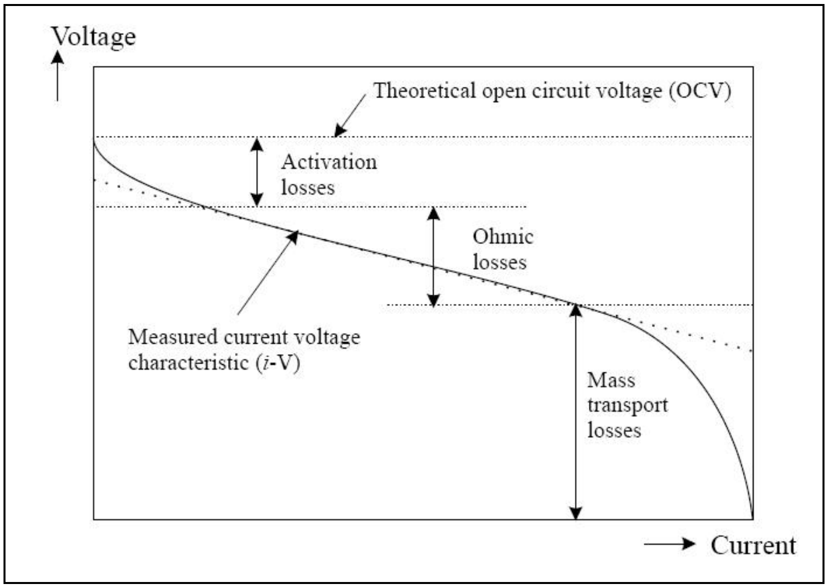

Figure 1.10 Current-voltage curve for a fuel cell.

The cell voltage can be expressed as $E_{cell} = E_{Nernst} - \eta$ where E_{Nernst} is the open cell voltage given by:

$$E_{Nernst} = E^0 + \frac{RT}{2F} \ln \frac{P_{H_2} P_{O_2}^{1/2}}{P_{H_2O}} \tag{1.1}$$

where E^0 is the standard electrode potential, R is the universal gas constant, T is the temperature, F is the Faraday's constant, and P_x is the partial pressure of species x. The Nernst potential is the cell voltage determined from reversible thermodynamic properties. As the cell begins to supply current to an external load, it moves away from a state of equilibrium, and the operating voltage drops due to irreversibilities associated with internal charge transfer, conduction, and diffusion processes. These irreversibilities are individually categorized as activation, ohmic, and concentration polarization (also often called mass transport losses), respectively. These polarizations can be considered as voltage losses and are given as follows:

$$\eta = \eta_{act} + \eta_{ohm} + \eta_{conc} \tag{1.2}$$

Activation polarization (η_{act}) or charge transfer is due to the energy barrier that must be surpassed before an electrochemical reaction can take place. Because the reaction rate increases with increasing temperature, the activation loss decreases with increasing temperature. At the high operating temperature of SOFC's, the activation loss or charge transfer is usually small.

Ohmic polarization (η_{ohm}) is caused by the ohmic resistance of the cell materials and is linearly dependent on the current and current path. Both electrodes contribute through their resistance towards electron conduction and the electrolyte contributes through its resistance towards ion transport. Because both the electrolyte and electrodes obey Ohm's law, the ohmic losses can be expressed by the equation

$$\eta_{ohm} = iR \tag{1.3}$$

where i is the current flowing through the cell, and R is the total cell resistance, which includes electronic, ionic, and contact resistance:

$$R = R_{electronic} + R_{ionic} + R_{contact} \tag{1.4}$$

Concentration polarization (η_{conc}) is the voltage loss due to resistance towards diffusion of the gaseous species in the electrodes. The gases entering the SOFC normally flow over the electrodes in a laminar manner. Diffusion therefore must take care of the transport of the reacting species through the electrodes to and from the TPBs. At high current densities, the relatively slow diffusion processes may limit the electrochemical conversion. Additionally, as the electrochemical reactions proceed, the reaction products formed at the anode dilute the fuel, and the diffusion resistance increases. Diffusion or concentration polarization occurs, for instance, when reaction products are removed slower than the formation of these products, or when the reactant feed is lower than the transport that may be reached on the basis of the discharge current of the cell, i.e., the reactant conversion has reached 100%.

1.5. Literature Survey

The current scientific literature on areas central to this doctoral dissertation deals with various aspects and is rather expansive. The following sub-sections intend to give a literature review of the following key areas: research on fabrication and SOFC modeling of microarchitectures in SOFC electodes.

1.5.1. Fabrication of Microarchitectures in SOFC Electrodes

Functionally graded materials (FGM) have been applied to SOFC and have provided the possibility to enhance the cell performance [18-22]. The purpose of grading is to optimize the electronic/ionic conductivity, to increase the electrochemical reactivity of the electrode, or to minimize the mass transport resistance to gas mixtures.

Hart et al. fabricated functionally graded SOFC cathodes from the mixtures of strontium-doped LSM and gadolinia-doped ceria (CGO) using slurry spraying techniques [18]. Similar samples were also prepared from the mixtures of LSM and YSZ. The first layer comprises a mixture of 50 wt% LSM and 50 wt% YSZ or CGO and the second layer consists of 100 wt% LSM. The cathodes incorporating CGO into the structure gave improved performance over those fabricated using YSZ.

Holtappels et al. presented the multilayered cathodes composed of LSM and YSZ [19]. Some cathodes additionally carried a number of layers with a graded transition from LSM to strontium doped lanthanum cobaltite (LSC) to add an electronically highly efficient current collector. The cathodes were prepared by spray printing and low temperature sintering. The multilayered cathodes gave improved electrochemical performances compared to that of conventional cathodes.

Liu et al. fabricated nanostructured composite cathodes graded in both composition and microstructure using combustion CVD process [20]. The first layer comprises a 10 μm thick fine-grained 60 wt% LSM and 40 wt% GDC on the YSZ electrolyte. The second layer consists of 30 wt% LSM, 30 wt% LSC and 40 wt% GDC. Sequentially, a coarse layer of 60 wt% LSC and 40 wt% GDC was deposited on top of the cathode, as shown in Figure 1.11. The functionally graded structures of these cathodes dramatically increased the rates of electrode reactions and enhanced the transport of oxygen molecules to the active reaction sites. As a result, low interfacial polarization resistances and high power densities were achieved.

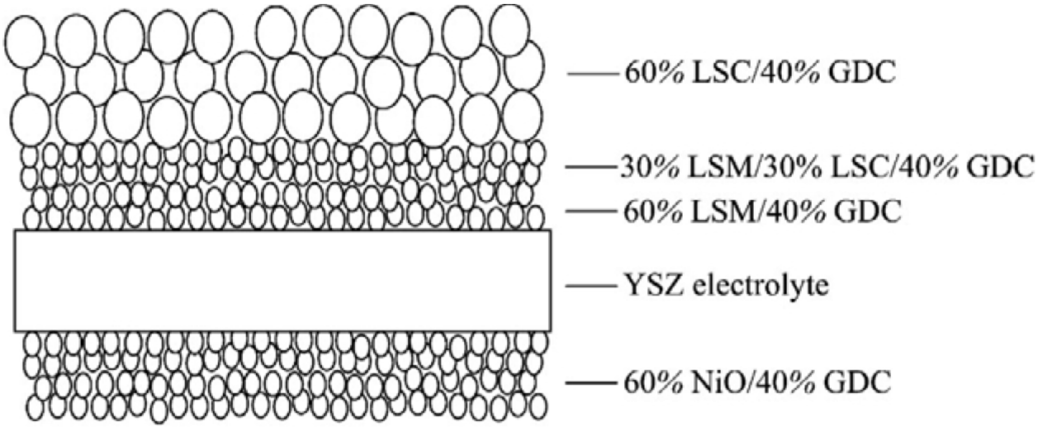

Figure 1.11 Schematic diagram of the functionally graded SOFC configuration [20].

Instead of FGMs, pore channels were applied to the SOFC electrode layers for improved SOFC performance. The “multistage nanoporous nickel substrate,” which has channels connecting both sides of the substrate, was fabricated for a SOFC anode, as shown in Figure 1.12 [23]. The term “multistage nanoporous nickel substrate” means that the pore size changes along the thickness direction of the substrate. The transition of pore size from 20 to 200nm takes place within 500nm from the 20nm surface. These channels enhance the delivery of fuel gas and the removal of H_2O vapor.

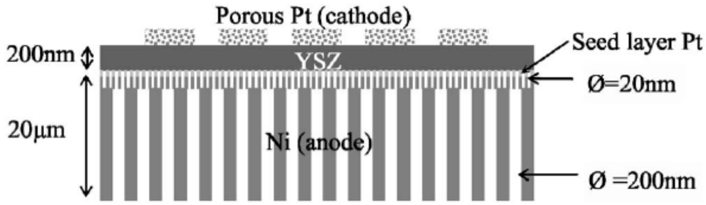

Figure 1.12 Schematics of thin-film SOFC fabricated on the multistage nanohole array nickel substrate [23].

1.5.2. SOFC Modeling of Microarchitectures in SOFC Electrodes

Mathematical modeling in fuel cell research has been successfully used for more than a decade now. Since experimental studies on SOFC are expensive, time-consuming and labor-intensive, quantitative mechanistic models are essential for SOFC technology development. A validated mechanistic model offers detailed insights into the complex physical phenomena governing SOFC performance. Therefore, it can be used as a numerical tool for cell design and optimization.

A mathematical model was developed for modeling the performance of SOFC with functionally graded electrodes (FGE) at the micro-scale level [24, 25]. Comparison between conventional non-graded (uniform random composites) electrodes and two types of FGEs, namely particle size graded and porosity graded SOFC anodes shown in Figure 1.13, were conducted to evaluate the potential of FGE for SOFC. Improved performance of both types of FGEs was observed due to reduced mass transport resistance and increased volumetric reactive surface area close to the electrode-electrolyte interface. It was found that the particle size graded SOFC anode showed the best performance.

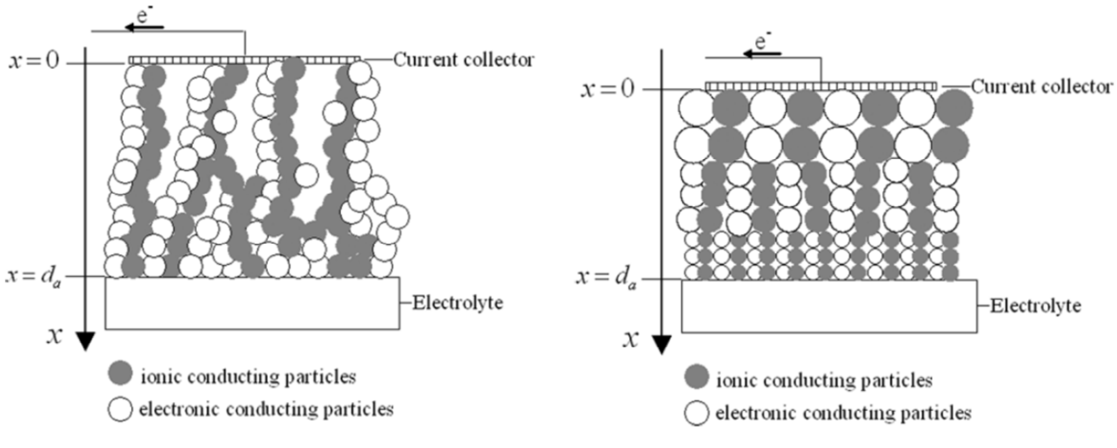

(a) **(b)**

Figure 1.13 Schematics of functionally graded electrodes: (a) porosity grading, and (b) particle size grading [24, 25].

Modeling of SOFC incorporating pore channels in the electrodes was conducted. Two types of planar SOFCs, which have channels in both the anode and the cathode, were computationally analyzed, as shown in Figure 1.14 [26]. A fully three-dimensional numerical analysis of the fluid dynamics and electrochemical kinetics was conducted for planar SOFCs. It was found that the fuel and air flow is progressively heated up along with the flow direction, and the hotspot locates at the end of the anode near the electrolyte, when the air and fuel stream is the co-flow. The output voltage measured in experiments and calculated using models agreed well.

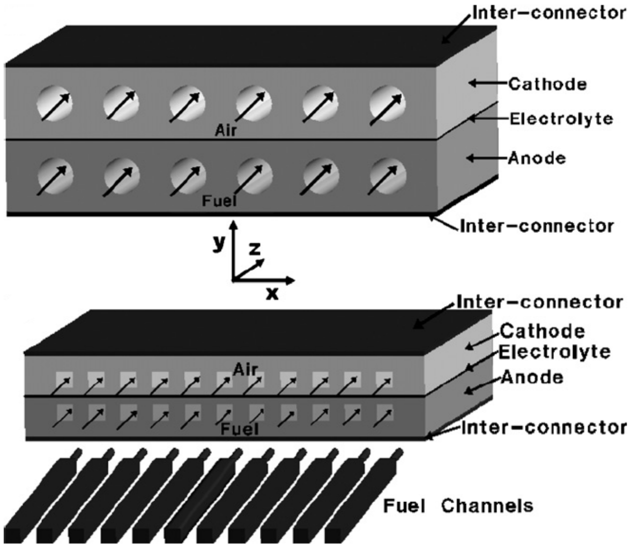

Figure 1.14 Schematics of two types of planar SOFCs [26].

1.6. Dissertation Outline

The remainder of this dissertation is divided into four chapters.

Chapter 2 presents the motivation to improve SOFC performance by controlling the distribution of the electrode layer materials. The limitation of conventional techniques to fabricate SOFCs with precise control over the orientation, placement, architecture, and distribution of conducting and porous pathways is discussed. A concept incorporating conducting wires and designed porous channels in the electrodes is proposed for improving the transport of electrons, reactant and product gases, which can result in improved overall performance of a SOFC.

Chapter 3 describes the development of a fundamental computational model-based approach to enhance the performance of SOFCs with a microarchitectured design. The performance improvement of mircoarchitectured SOFCs by applying this computational model to a typical SOFC is investigated and predicted. Moreover, the analysis of thermal stresses in the microarchitectured SOFC is investigated to examine the possibility of failure due to the presence of designed pore channels.

Chapter 4 focuses a proof-of-concept microarchitectured SOFC based on anode-supported SOFC button cells. Fabrication of microarchitectured SOFCs through laser ablation technique is demonstrated. The performance of a fabricated SOFC unit cell is characterized and compared against the performance predicted by the computational model.

Chapter 5 revisits the research objectives of this dissertation and summarizes the contributions of this dissertation. Recommendations for future work are also addressed.

CHAPTER 2

MOTIVATION AND STATEMENT OF RESEARCH

This chapter presents the limitations of conventional techniques to fabricate SOFCs with precise control over the orientation, placement, architecture, and distribution of conducting and porous pathways. The scientific basis and the motivation to improve SOFC performance by controlling the distribution of the electrode layer materials are presented. A concept incorporating conducting wires and designed porous channels in the electrodes is proposed for further investigation with the objective of achieving improved SOFC performance via improved transport of electrons, reactant and product gases.

2.1. Drawbacks of State-of-the-Art SOFC Manufacturing Techniques

Conventional techniques to fabricate SOFCs includes chemical vapor deposition (CVD), physical vapor deposition (PVD), electrochemical vapor deposition (EVD), electrophoresis deposition (EPD), atmospheric plasma spraying (APS), vacuum plasma spraying (VPS), sputtering, flame coating, laser ablation, sol-gel coat, and ceramic forming techniques such as tape casting, tape calendaring, screen printing, and dry press formation. These manufacturing techniques are not adequate for precise control over the orientation, placement, architecture, and distribution of conducting and porous pathways. Figure 2.1 shows a schematic of a typical SOFC made by conventional techniques and the random distribution of conducting particles and interconnected porosity that results as a function of the manufacturing technique.

Efforts to reduce ohmic polarization and concentration polarization are needed to achieve higher performance in the SOFCs, since the activation loss or charge transfer is usually small at the high operating temperature of SOFC's. This can be accomplished by controlling the distribution of the anode and cathode layer materials so as to optimize both electronic conductivity and gaseous mass transport.

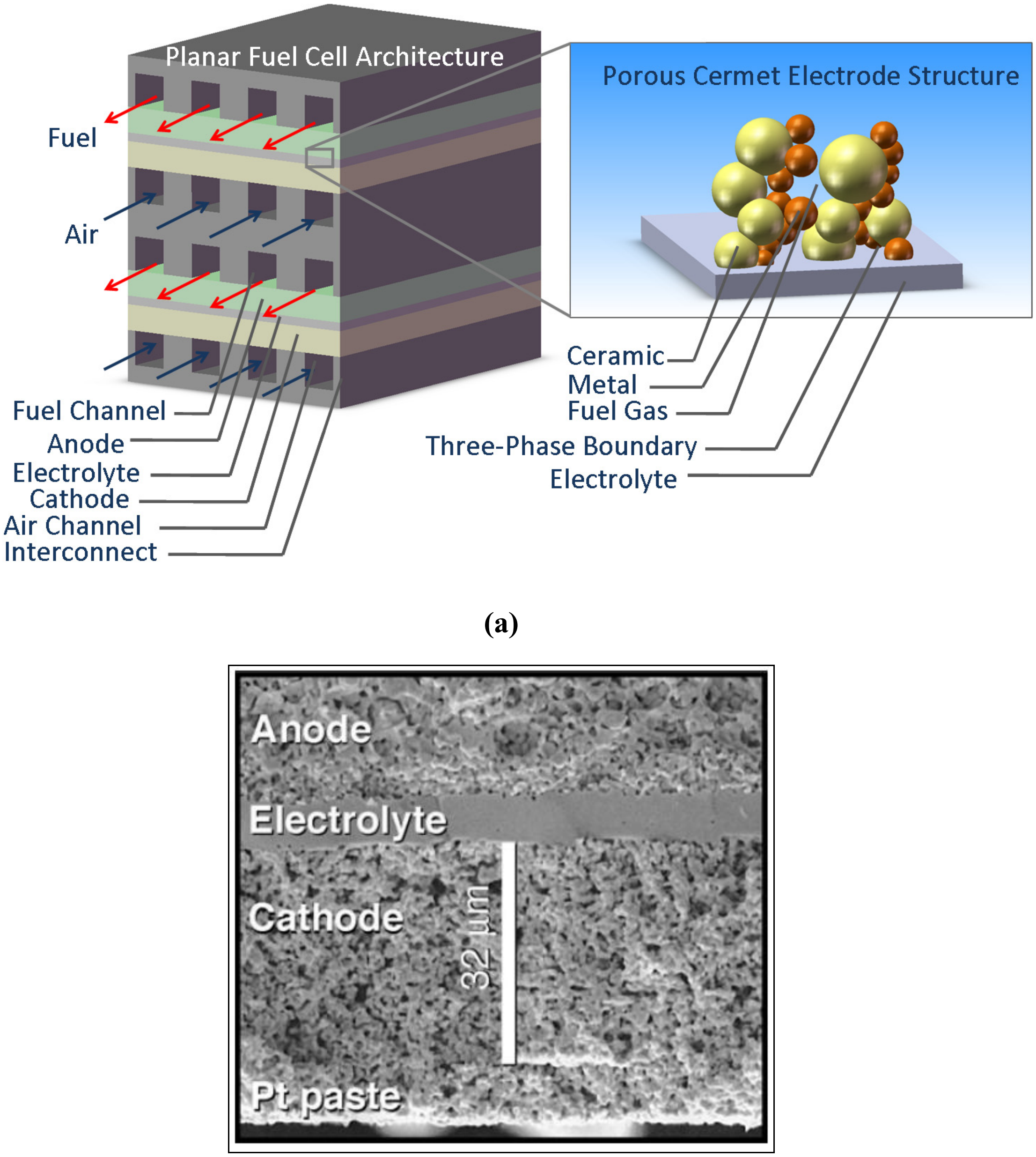

(a)

(b)

Figure 2.1 (a) Conventional planar SOFC architecture with random distribution of conducting particles and interconnected porosity that results from the conventional manufacturing techniques, and (b) Scanning electron micrograph of a SOFC made by conventional techniques [27].

The electronic conductivity of the anode, which is a cermet of metal and YSZ, can be expressed by the equation of the generalized effective media theory (GEM) [28]:

$$\sigma_{cermet} = \sigma_{metal}^{O}\left(1-\frac{V_p + V_{YSZ}}{V_{iso,c}}\right)^n \tag{2.1}$$

where σ_{metal}^{O} is the conductivity of pure metal at 25°C, V_p and V_{YSZ} are the volume fractions of pores and YSZ, respectively, $V_{iso,c}$ is the critical volume fraction of isolating phases, where the first percolation pathways are formed by metal, and n is an empirical exponent. To reduce ohmic polarization in the electrodes, for instance, straight metal wires from the electrode-electrolyte interface to the current collector can be formed inside the electrode. For the straight metal wire, the electronic conductivity is directly σ_{metal}^{O}, which will increase the overall electronic conductivity of the electrode, i.e., it will decrease $R_{electronic}$ value in equation (1.4).

The mass diffusion coefficient for species *i* in a gaseous mixture is computed as

$$D_{i,m} = \frac{1-X_i}{\sum\limits_{j,j\neq i}(X_j / D_{ij})} \tag{2.2}$$

where X_i is the molar fraction of species *i*, and D_{ij} is the binary mass diffusion coefficient of a mixture of species *i* and *j*.

The binary diffusion coefficient D_{ij} of a mixture species *i* and *j* is computed using the Fuller et al. expression [29]:

$$D_{ij} = \frac{0.0143T^{1.75}}{PM_{ij}^{1/2}(\upsilon_i^{1/3}+\upsilon_j^{1/3})^2} \tag{2.3}$$

where $M_{ij} = 2(1/M_i + 1/M_j)^{-1}$, M is molecular weight in kg/kmol, υ is the special Fuller et al. diffusion volume in m^3/kmol, T is the absolute temperature in K, and P is the pressure in Pa.

For straight and round pores [30], Knudsen diffusion is given by

$$D_K = 97.0 r_p \sqrt{\frac{T}{M_i}} \tag{2.4}$$

where D_K is Knudsen diffusion coefficient in m^2/s, r_p is the average radius of the pore in m, T is the absolute temperature in K, and M_i is molecular weight of species i in kg/kmol.

Due to the tortuous pathways and constrictions in the pores, the diffusivity is corrected by a tortuosity factor, τ, and porosity of porous medium, ε. The tortuosity factor accounts for both the effects of altered diffusion path length and the changing cross-sectional area in constrictions. A lower value of tortuosity implies a shorter mean diffusion path length and hence higher diffusivity.

Thus, the overall effective diffusion coefficient is given by [30]

$$D_{i,eff} = \frac{\varepsilon}{\tau}\left(\frac{1}{D_{i,m}} + \frac{1}{D_K}\right)^{-1} \tag{2.5}$$

Therefore, if straight porous channels are constructed inside the electrodes, the tortuosity factor will be decreased and the overall effective diffusion coefficient will be increased. This results in improved mass transport, decrease in the η_{conc} value in Equation (1.2), and therefore reduction in concentration polarization losses.

It is clear that simultaneously increasing electronic conductivity and diffusivity (through porosity control) in the electrodes leads to improved SOFC performance. However, from a SOFC design and manufacturing perspective, these objectives are conflicting. Conventional SOFC manufacturing techniques create tortuous porosity pathways and random distribution of electronically conducting networks in the electrodes. They do not provide adequate control over the orientation, placement, architecture, and distribution of conducting and porous pathways so as to fully optimize

SOFC performance. Fabrication of SOFCs with optimized material microarchitectures thus requires new computational design and novel manufacturing techniques.

2.2. Simultaneous Optimization of Mass Transport and Conductivity

In a majority of conventional techniques that are used to produce the films of SOFC materials, SOFC components are mixed with molten resin before processing, which causes tortuous porosity pathways and random distribution of electronically conducting networks in the electrodes. The fabrication of a SOFC with intentionally designed conducting wires and porous channels is nearly impossible using these techniques. Therefore, new and novel fabrication techniques that enable controlled distribution of SOFC materials are needed. Alternatively, additional fabrication processes should follow conventional techniques.

Researchers around the world have focused their efforts on the development of new SOFC materials and on new fabrication techniques to enhance the performance of SOFCs. Studies to incorporate the microarchitectures in the electrode layer materials for the performance improvement of SOFCs have also been investigated, as discussed in section 1.5. However, SOFCs with FGMs still have the random distributions of electrode materials and porosity. This can cause inconsistent performance of SOFCs. On the other hand, by incorporating conducting wires and designed porous channels in the electrodes, the distribution of electrode materials and porosity can be intentionally designed. Therefore, mass transport and electron transport in the electrode can be decoupled and controlled individually. This can result in more consistent SOFC performance while providing opportunities to perform more systematic design optimization. A few studies investigated incorporating pore channels in the electrodes [23, 26]. However, electrodes including predefined porous channel dimensions for both studies were fabricated or simulated. Systematic approaches to the computational design and performance optimization of microarchitectured SOFCs were not developed.

A schematic cross-section of a SOFC concept that better addresses the multifunctional requirements elaborated in chapter 1 is shown in Figures 2.2 (a) and (b). This concept incorporates conducting wires and designed porous channels in the electrodes, for improved transport of electrons, reactant and product gases, which can result in improved overall performance of a SOFC. This dissertation focuses on the computational design optimization and experimental validation of one aspect, the anode side porous channels, of this concept.

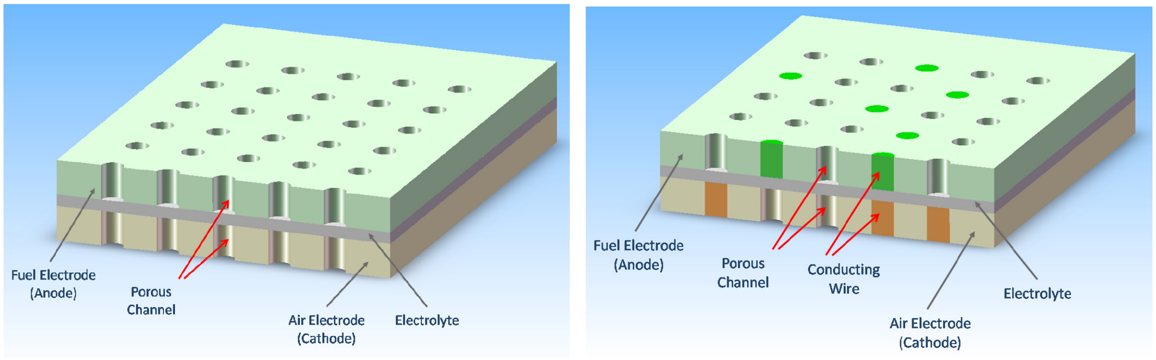

(a) **(b)**

Figure 2.2 Schematic cross-section of a SOFC with (a) designed porous channels, and (b) designed conducting wires and designed porous channels.

2.3. Statement of Research

The main objectives of this dissertation are to:

1. Investigate the computational design and performance optimization of microarchitectured SOFCs that simultaneously optimize mass transport and electron transfer so that SOFC performance could be greatly improved over currently attainable performance in state-of-the-art SOFCs. A coupled multiphysics simulation of mass transport, electrochemical charge transfer reaction, and current balance will be developed and tested as a function of SOFC microarchitecture.
2. Demonstrate the fabrication of microarchitectured SOFCs, based on anode-supported SOFC button cells through laser ablation technique. A femtosecond laser will be utilized to micromachine pore channels in the button cell. Micromachining process parameters will be optimized to achieve the desired pore size, geometry, and depth. Micromachined pores will be characterized using interferometry-based non-contact profilometry and scanning electron microscopy.
3. Characterize the performance of micromachined SOFC unit cells and compare it against the performance of a "baseline" unmicromachined cell, as well as against the performance predicted by the computational model, as a proof-of-concept. Performance characterization of SOFC button cells will include power output performance and electrochemical impedance spectroscopy. The fundamental computational model developed earlier will be applied to the

specific SOFC to compare experimentally measured performance data against the model's predictions.

4. Present recommendations for future work on further optimization of SOFC performance and for scale-up fabrication of microarchitectured SOFCs.

CHAPTER 3

COMPUTATIONAL DESIGN OF OPTIMAL MICROARCHITECTURES

The objective of this chapter is to develop a fundamental computational model-based approach to enhance the performance of SOFCs with microarchitecture design and to investigate and predict the performance improvement of mircoarchitectured SOFCs by applying this computational model to a typical SOFC.

3.1. Design Optimization for a Typical SOFC Unit Cell

3.1.1. Baseline Unit Cell Geometry and Modeling Assumptions

Button cells are widely used in SOFC experimental studies due to their simple experimental set up and operation. Therefore, the anode-supported SOFC button cell will be used for model validation, computational design, and performance optimization of microarchitectured SOFCs that simultaneously optimize mass transport and electron transfer.

For the sake of simplicity of calculation, one repeating cell unit is analyzed in this simulation. The size of one baseline unit is 1mm (l) × 1mm (w) × 1.06mm (h) with 1mm thick Ni-YSZ anode, 10μm thick YSZ electrolyte, and 50μm thick LSM-YSZ cathode as shown in Figure 3.1.

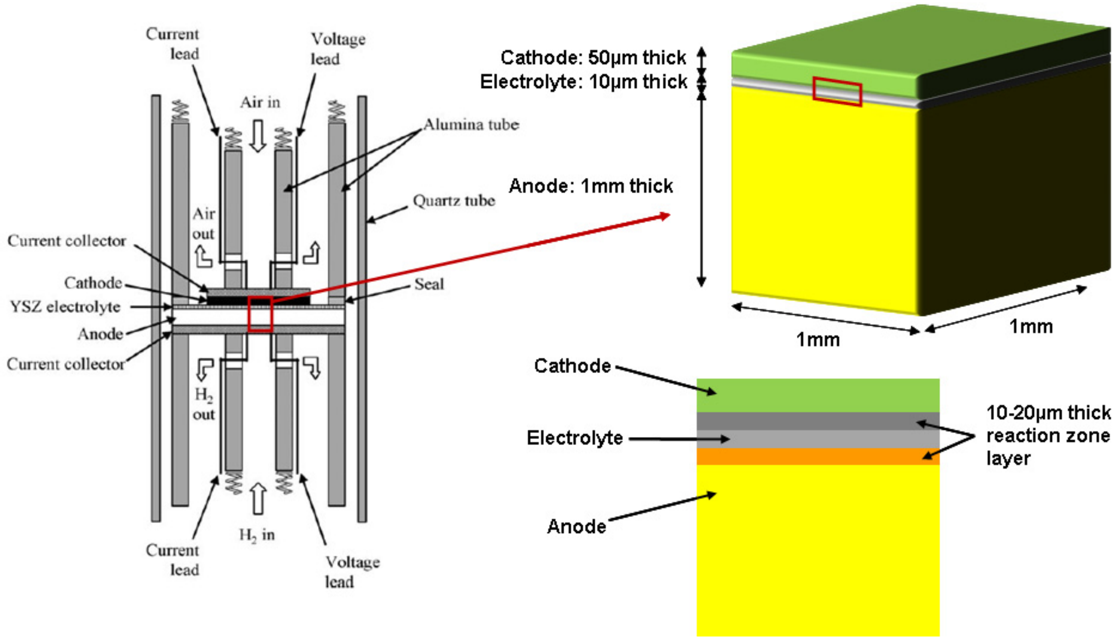

Figure 3.1 Schematic of a SOFC button cell and baseline unit cell geometry.

The assumptions made in the analysis are as follows:

- The SOFC operates at steady state.
- The reactant gas mixture is approximated as an ideal gas.
- The model is assumed to be isothermal and the cell runs at 800°C.
- Convection flux is neglected and only diffusion is considered in the porous electrode.
- Pressure gradients in the porous electrode are also neglected.
- The mathematical simulation is performed at 0.7V, which is the typical operating voltage of SOFCs.
- A reaction zone layer where electrochemical reactions occur is assumed in both electrodes.

3.1.2. Modeling Methodology

The modeling methodology is illustrated in Figure 3.2. The ionic and electronic charge balance, the mass balance, and the electrochemical charge transfer reactions are considered for modeling, as shown in Figure 3.2. In this study, the open-circuit state is chosen as the reference state. The simulations produce average current density and polarization curves as the outputs. With the coupled governing equations, the operating conditions and the microarchitecture design as the inputs, the model is validated and performance optimization is executed.

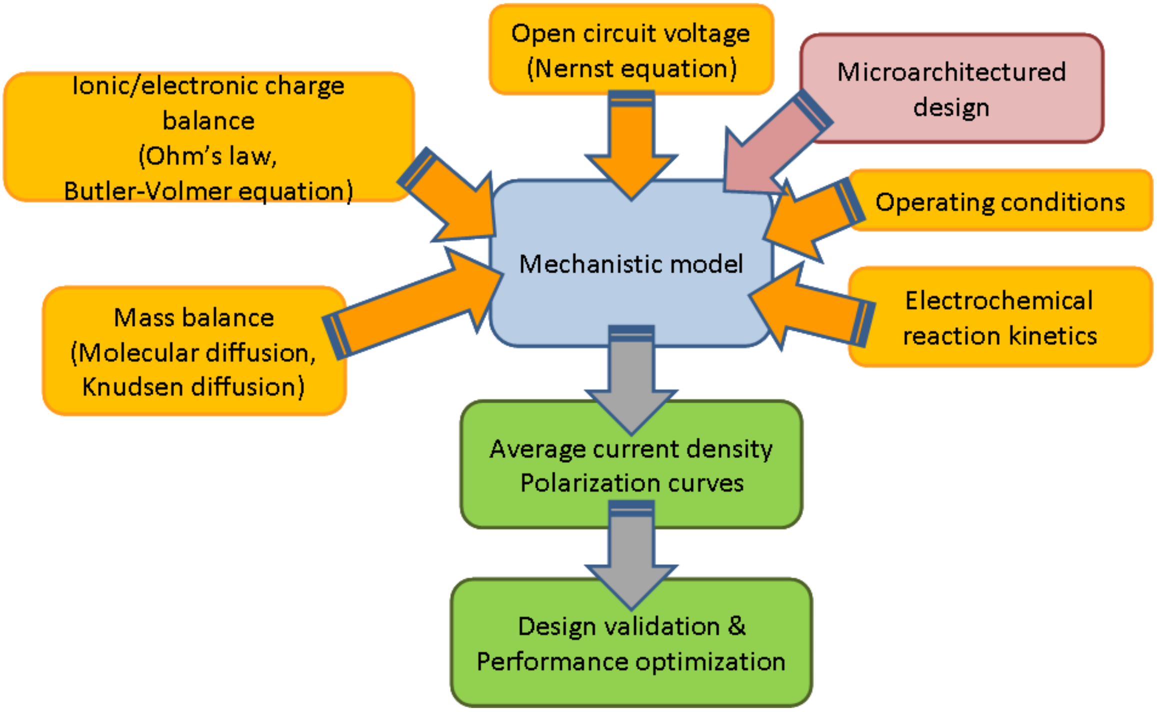

Figure 3.2 Modeling methodology.

The electronic and ionic potential in the current balance is explained more clearly as follows. The continuity of current in a conducting material can be stated as follows:

$$\nabla \cdot i = 0 \tag{3.1}$$

where i stands for the current density vector. Two types of charges are present in fuel cell systems—electrons and ions. Since both types of charges are generated from originally neutral species (hydrogen and/or oxygen), overall charge neutrality must be conserved, as follows:

$$\nabla \cdot i_{el} + \nabla \cdot i_{ion} = 0 \tag{3.2}$$

where i_{ion} stands for the ionic current density through an ion-conducting phase such as a catalyst layer or an electrolyte membrane, and i_{el} stands for an electronic current density in an electron-conducting phase such as a catalyst layer or an electrode. Equation 3.2 can be rearranged and related to local current density, j, as follows:

$$-\nabla \cdot i_{ion} = \nabla \cdot i_{el} = S_{TPB} j \tag{3.3}$$

By incorporating Ohm's law into this equation, we get

$$\nabla \cdot (\sigma_{ion} \nabla \Phi_{ion}) = -\nabla \cdot (\sigma_{el} \nabla \Phi_{el}) = S_{TPB} j \tag{3.4}$$

where Φ_{ion} and Φ_{el} are the electric potentials in the ionic and electronic conductors, respectively, σ_{ion} and σ_{el} are the ionic and electronic conductivities, respectively, and S_{TPB} is the electrochemically active area per unit volume of the electrode.

The electric potential distribution of an SOFC [31] is shown schematically in Figure 3.3. The measured cell voltage is given as the difference between the electric potentials of the current collectors at the anode and the cathode. The cell voltage is then described by:

$$E(i) = \Phi_{el,ca}(i) - \Phi_{el,an}(i) \tag{3.5}$$

where Φ_{el} is the electric potential in an electronic conducting phase.

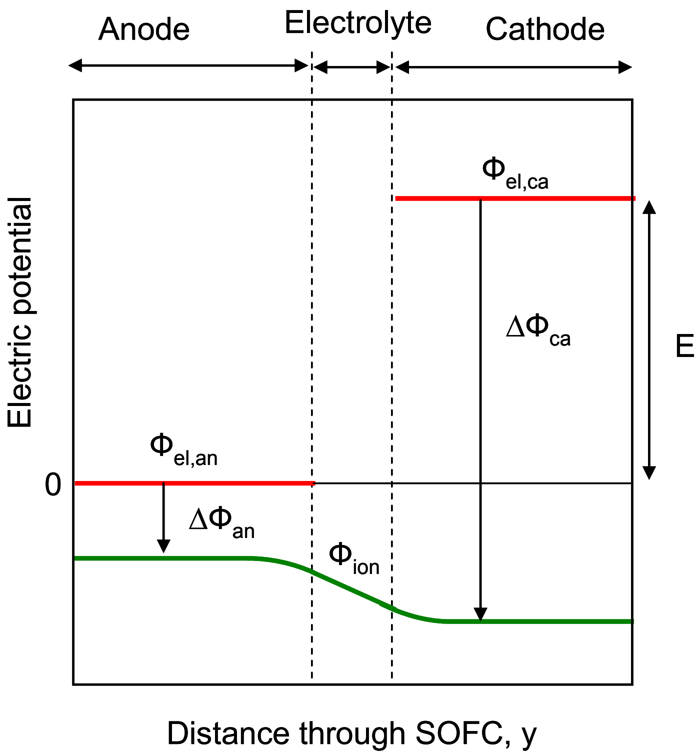

Figure 3.3 Electric potential distribution in a polarized SOFC with porous composite electrodes.

The electrodes are at different potentials due to the two electric potential steps, $\Delta\Phi_{an}$ and $\Delta\Phi_{ca}$, that form at the electrical double layers at the anode/electrolyte and cathode/electrolyte interfaces, respectively.

$$\Delta\Phi_{an}(y) = \Phi_{el,an} - \Phi_{ion,an}(y) \qquad (3.6)$$

$$\Delta\Phi_{ca}(y) = \Phi_{el,ca} - \Phi_{ion,ca}(y)$$

where Φ_{ion} is the electric potential in an ionic conducting phase. Since composite electrodes consist of electronic and ionic conducting phases, the potential steps depend on the spatial position y along the electrode thickness. Additionally, there is a potential gradient inside solid electrolyte due to ohmic resistance, resulting in a potential drop over the solid electrolyte. All potentials depend on the cell current density.

If flat electrodes and no gradients within electrodes are assumed, the cell voltage can be represented by combining Equation (3.5) and (3.6) and subtracting the potential drop over the solid electrolyte:

$$E(i) = \Delta\Phi_{ca}(i) - \Delta\Phi_{an}(i) - iR_{elyt} \tag{3.7}$$

where R_{elyt} is the ohmic resistance of the electrolyte.

The transfer of charges between the electronic and ionic conductor is illustrated in Figure 3.4 and described by the polarization equation that can be written in the general Butler-Volmer form, as follows:

$$j = j_0\left(\frac{C_{react}}{C_{react}^{bulk}}\exp\left[\alpha\frac{n_eF\eta}{RT}\right] - \frac{C_{prod}}{C_{prod}^{bulk}}\exp\left[-(1-\alpha)\frac{n_eF\eta}{RT}\right]\right) \tag{3.8}$$

where j_0 is the exchange current density; α the charge transfer coefficient; n_e the electrons transferred per reaction; F the Faraday constant; R the gas constant; T the temperature; c_{react}, c_{react}^{bulk}, c_{prod}, c_{prod}^{bulk} are the reactant and product concentrations at the reaction active sites and the electrode-gas channel interface; and η is the local overpotential.

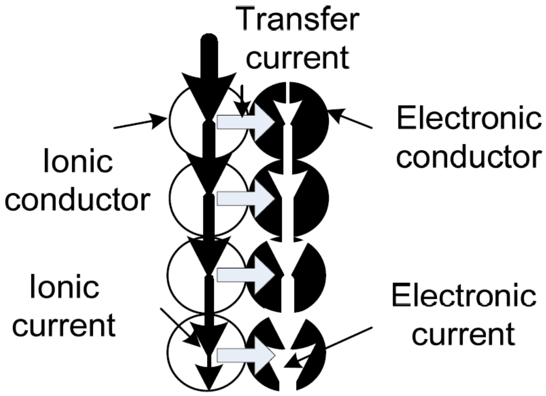

Figure 3.4 Charge transfer between electronic and ionic conductor.

The operating cell voltage, *E(i),* is usually much lower than the Nernst potential due to irreversibilities as mentioned in section 1.4. Thus, *E(i)* can be written as:

$$E(i) = E_{Nernst} - \eta_{an}(i) - |\eta_{ca}(i)| - iR_{elyt} \tag{3.9}$$

where E_{Nernst} is the Nernst potential, η_{an} and η_{ca} are the potential losses in the anode and cathode, respectively, and R_{elyt} is the ohmic resistance of the electrolyte.

By comparing Equation (3.7) and (3.9), the local overpotential is defined as:

$$\eta = \psi(\Phi_{el} - \Phi_{ion} - \Phi_{ref}) \tag{3.10}$$

where Φ_{ion} and Φ_{el} are the electric potentials in the ionic and electronic conductors, Φ_{ref} is the relative potential difference between the electronic and ionic conductors at the reference state, ψ=1 in the anode, and ψ=-1 in the cathode. In this study, the open-circuit state is chosen as the reference state. By setting $\Phi_{ref,an}$ to zero, the cathode reference potential $\Phi_{ref,ca}$ becomes the open circuit voltage. Therefore, $\Phi_{ref,ca}$ can be obtained from the Nernst equation.

Diffusion inside the porous media is important for fuel cell reactions. Diffusion in a porous medium is usually described by molecular diffusion and Knudsen diffusion. Knudsen diffusion occurs when the diameter of the pores in the porous medium is small compared with the mean free path of the gas molecules, i.e. Knudsen number Kn>>1. Molecular diffusion occurs when the pore diameter is large compared with the mean free path of the gas molecules, i.e. Kn<<1. For SOFCs, both Knudsen and molecular diffusion processes have to be considered since, in general, Kn≈1 [26]. Therefore, the effective gas diffusion coefficient for component i in the porous media can be expressed as a combination of the Knudsen diffusion and molecular diffusion (Equation (2.5)). The mass balance for the species at steady state in the macroscopic structure is governed by the equation below, neglecting the convection term:

$$\nabla \cdot (-D_{i,eff} \cdot \nabla c_i) = R_i \tag{3.11}$$

where c_i is the concentration and R_i is the source term of mass balance and can be formulated as the reaction rate of the electrochemical and chemical reactions.

In the reaction active sites of the cathode, the relationship between the mass balance source term and the current source term can be stated according to the Faraday's law as:

$$R_{O_2} = -\frac{j_{trans,ca} S_{TPB}}{4F} \tag{3.12}$$

where $j_{trans,ca}$ is local charge transfer current density at the cathode, S_{TPB} is the three-phase boundary active area per unit volume, and F is the Faraday constant.

In the reaction active sites of the anode, the reactions include the electrochemical reactions of hydrogen and carbon monoxide and the shifting reactions. Similar to the cathode, the relationship between the mass balance source term and the current source term can be built:

$$R_{H_2} = -\frac{j_{trans,an} S_{TPB}}{2F} \tag{3.13}$$

$$R_{H_2O} = \frac{j_{trans,an} S_{TPB}}{2F} \tag{3.14}$$

In the remaining electrode regions, the mass balance source term is equal to zero, that is, $R_i = 0$. In the designed porous channels, only molecular diffusion processes are considered, since $Kn \ll 1$. Therefore, the effective gas diffusion coefficient in the designed porous channels can be expressed as Equation (2.3). Furthermore, $R_i = 0$ because there is no source or sink in the designed porous channels.

In the reaction active sites of the cathode, the ionic charge balance can be described as:

$$\nabla \cdot (-\sigma_{ion,ca} \cdot \nabla \Phi_{ion,ca}) = -j_{trans,ca} S_{TPB} \tag{3.15}$$

Similar to the ionic charge balance, the electronic charge balance in the reaction active sites of the cathode can be described as:

$$\nabla \cdot (-\sigma_{el,ca} \cdot \nabla \Phi_{el,ca}) = j_{trans,ca} S_{TPB} \tag{3.16}$$

Similar to the cathode, the ionic charge balance and the electronic charge balance in the reaction active sites of the anode can be described as:

$$\nabla \cdot (-\sigma_{ion,an} \cdot \nabla \Phi_{ion,an}) = j_{trans,an} S_{TPB} \tag{3.17}$$

$$\nabla \cdot (-\sigma_{el,an} \cdot \nabla \Phi_{el,an}) = -j_{trans,an} S_{TPB} \tag{3.18}$$

In the remaining electrode regions, the current balance source term is equal to zero. Within the electrolyte layer, there is only ion conduction and there are no current sources or sinks. Consequently, only ohmic polarization exists in the electrolyte and the charge balance governing equation can be described as:

$$\nabla \cdot (-\sigma_{ion,electrolyte} \cdot \nabla \Phi_{ion,electrolyte}) = 0 \tag{3.19}$$

3.1.3. Simulation Results

3.1.3.1. Baseline Unit Cell

Electrochemical charge transfer reactions in a SOFC are likely to occur in an electrochemically active region, the TPB area, close to the electrolyte. The thickness of the electrochemically active region can be varied with different fabrication methods. A spray painted LSM-YSZ cathode showed decreasing interfacial resistance with increasing cathode thickness but reached a saturation value at approximately 10µm [32]. Tape-cast LSM-YSZ cathodes showed no performance change between 20 and 50µm [33]. The electrochemically active region typically extends 10 to 20µm from the electrolyte boundary into the electrode [33-36]. In order to remove ambiguity, the thickness of the electrochemically active region is chosen to be 10μm or 20μm in this study. The average current density at locations along the SOFC cell thickness is computed by averaging the current density distribution across the entire planar area at each location. The electronic and ionic current density distributions at the typical operating voltage of SOFCs, 0.7V, in the anode, cathode, and electrolyte along the cell thickness direction, with the assumption of a 10μm thick reaction zone layer are shown in Figures 3.5 (a) and (b). The electronic and ionic current density distributions at the typical operating voltage of SOFCs, 0.7V, in the anode, cathode, and electrolyte along the cell thickness direction, with the assumption of a 20μm thick reaction zone layer are shown in Figures 3.6 (a) and (b). Most ions are eliminated or generated near the electrode-electrolyte interface where most electrons are generated or eliminated, respectively. The results display typically expected variation of electronic and ionic current density since the electrochemical charge transfer reactions occur in the TPB region close to the electrolyte. The concentration distributions of H_2 and H_2O in the anode along the cell thickness direction, with the assumption of 20μm thick reaction zone layer are shown in Figure 3.7 (a) and (b), respectively. It can be observed that the concentration of H_2 decreases in the anode from fuel channel/anode interface to anode/electrolyte interface, while the concentration of H_2O increases. This is due to the electrochemical oxidation of H_2 at the reaction active sites resulting in the production of H_2O. Consumption of H_2 at the anode/electrolyte interface results in the depletion of H_2 within the anode. The concentration of H_2 falls from its bulk value at the fuel channel to a much lower value at the reaction active sites, while the concentration of H_2O rises since it is the product.

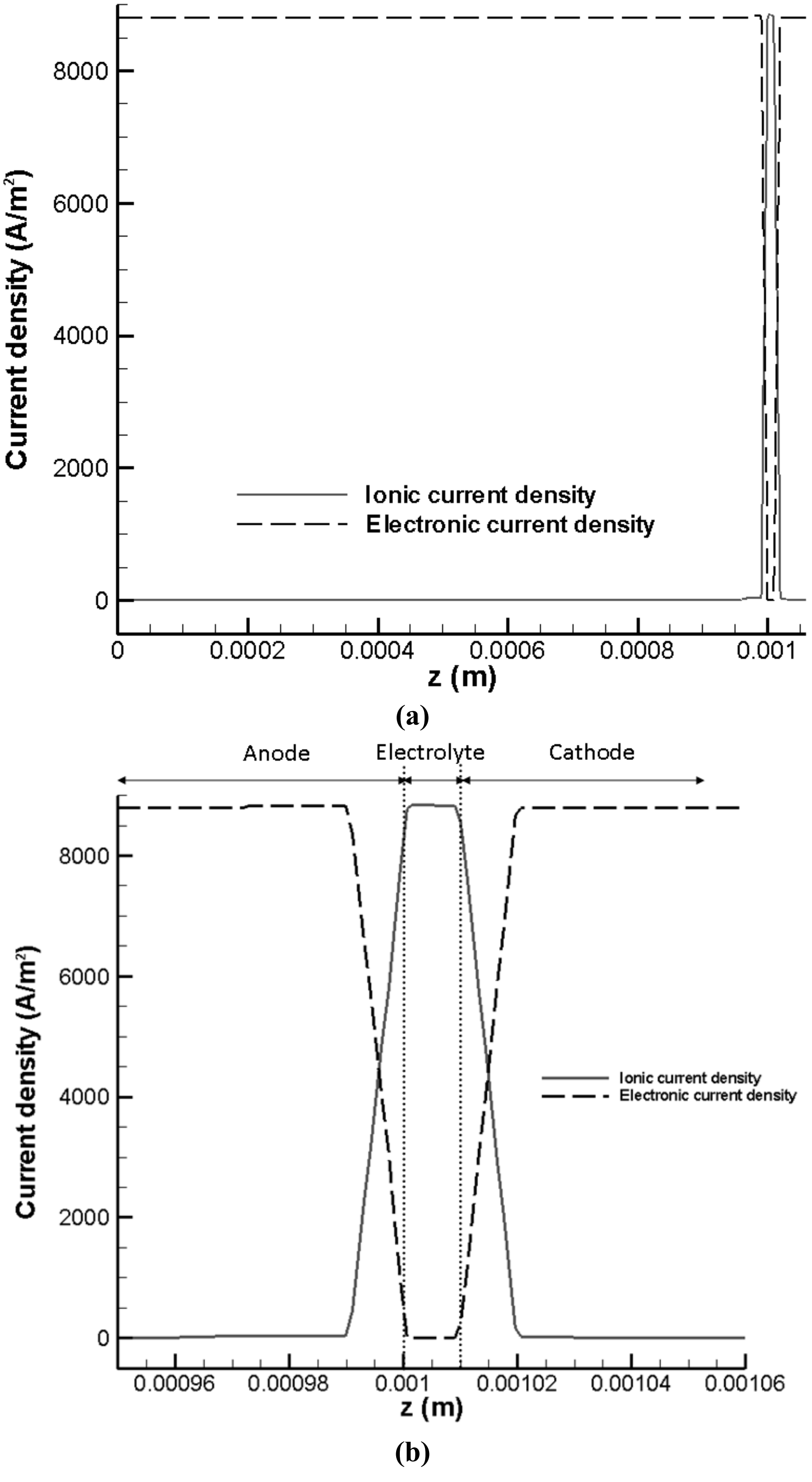

Figure 3.5 (a) Current density distribution and (b) Magnified view of current density distribution with the assumption of 10µm thick reaction zone layer.

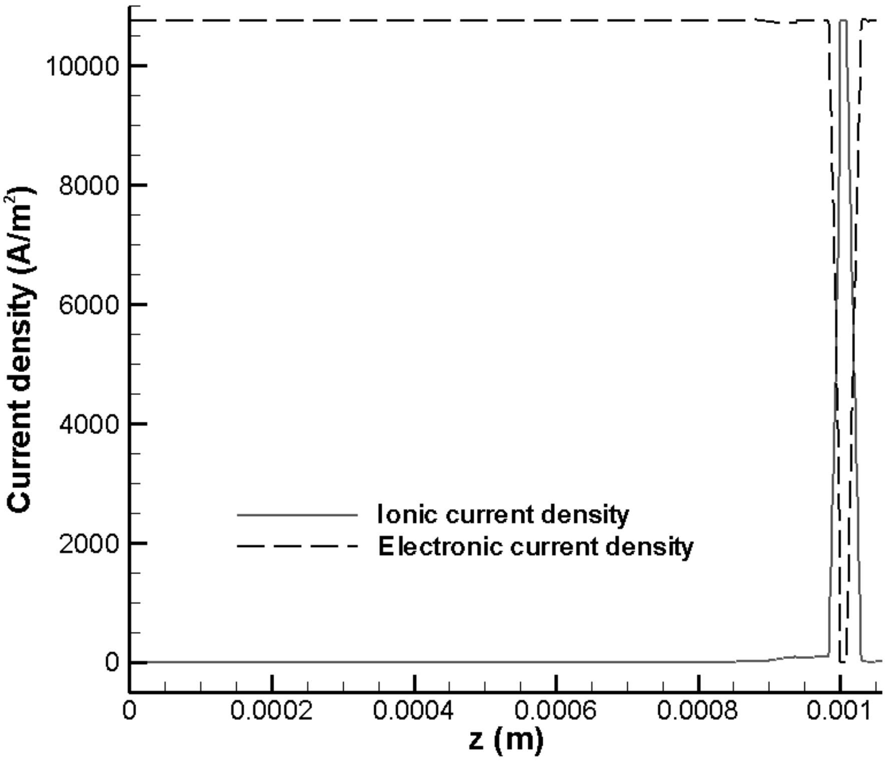

(a)

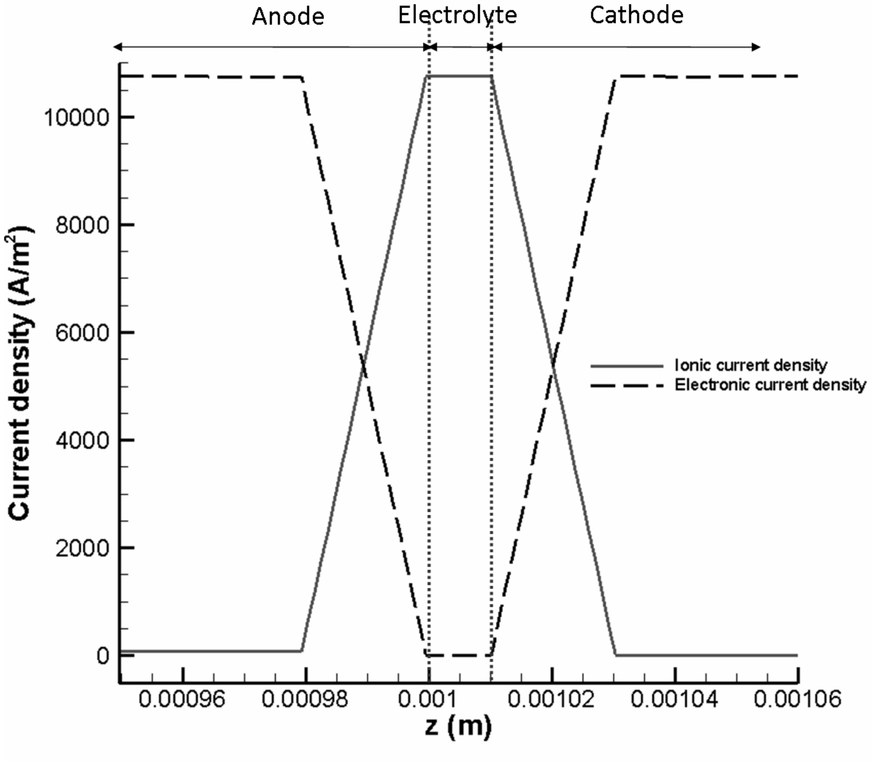

(b)

Figure 3.6 (a) Current density distribution and (b) Magnified view of current density distribution with the assumption of 20µm thick reaction zone layer.

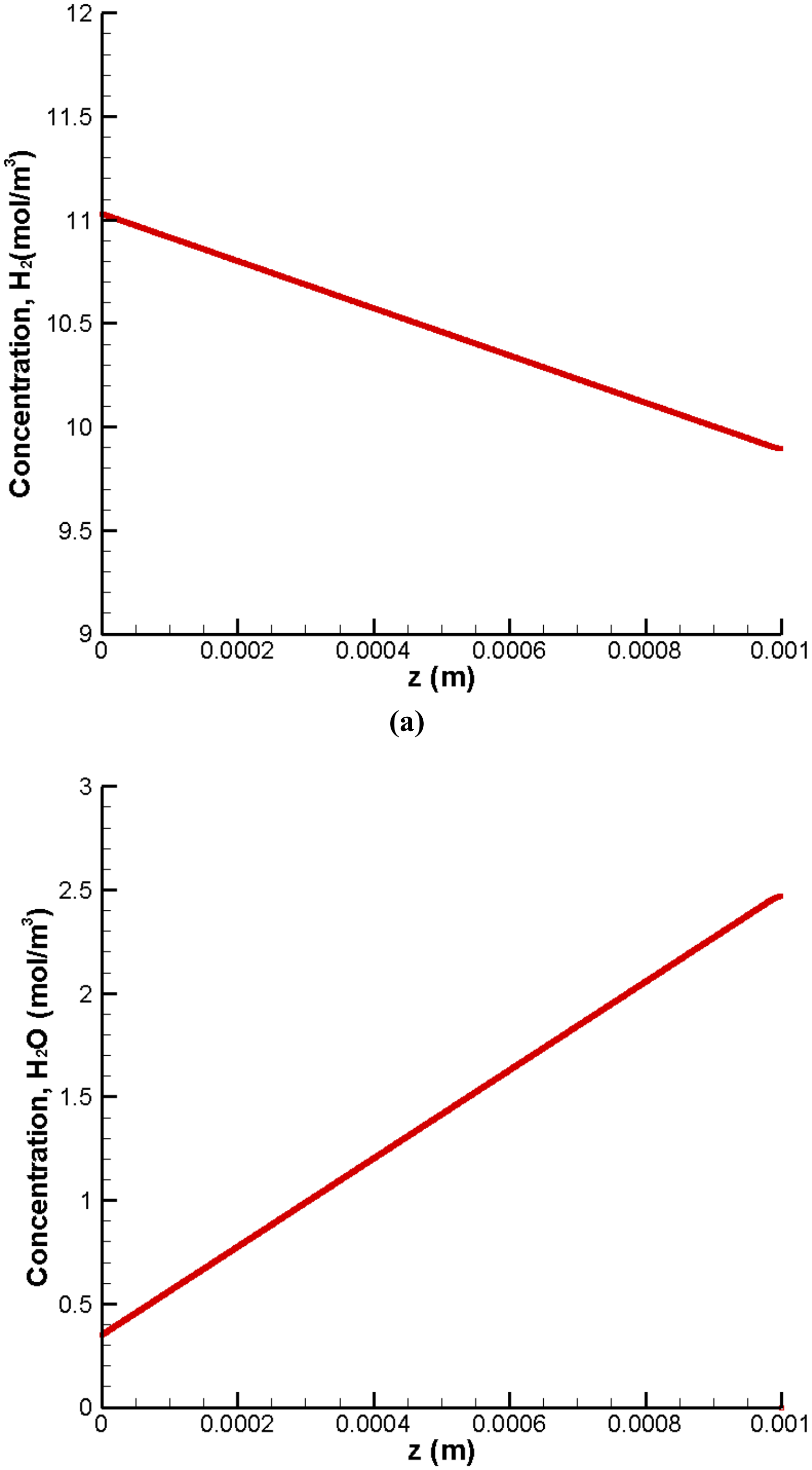

(a)

(b)

Figure 3.7 (a) H_2 and (b) H_2O concentration (mol/m^3) in the anode along the cell thickness direction, with the assumption of 20μm thick reaction zone layer.

3.1.3.2. Model Validation

The model was validated against two sets of experimental results published in the literature. The polarization curves obtained by this model's simulations were compared with experimental data in the literature.

First Experimental Validation

Experimental parameters input to model [37, 38] (from experimental measurement by W.A. Rogers et al.) are as follows:

- Electrolyte thickness: 10 μm
- Anode electrode layer thickness: 1 mm
- Anode reaction zone layer thickness: 20 μm
- Cathode electrode layer thickness: 50 μm
- Cathode reaction zone layer thickness: 20 μm
- Electrode porosity: 37.5 %
- Fuel composition: H_2 95 % H_2O 5 %
- Oxidant: air

The other input parameters to model are described in Table 3.1.

Table 3.1 The other input parameters to model [30, 39-42].

Cathode exchange current density, $j_{0,ca}$ (A m^{-2})	2000
Anode exchange current density, $j_{0,an}$ (A m^{-2})	5300
Transfer coefficient, α	0.5
Temperature, T (K)	1073.15
Average pore radius, r_p (μm)	0.5
Ionic conductor conductivity, σ_{ion} (S m^{-1})	$3.34\times10^4\exp(-10{,}300/T)$
Cathode electronic conductor conductivity, $\sigma_{elec,ca}$ (S m^{-1})	$42\times10^6\exp(-1{,}200/T)$
Anode electronic conductor conductivity, $\sigma_{elec,an}$ (S m^{-1})	$95\times10^6\exp(-1{,}150/T)$

Since the tortuosity value for SOFC electrodes is a difficult parameter to measure through experiment, the tortuosity value is treated as an adjustable parameter to assure the agreement of the modeling results and experimental data. The typical tortuosity value reported for SOFC electrodes is in the range of 2-6 [43, 44]. The value of tortuosity is varied to obtain the best agreement between the present model predictions and the experimental results. A tortuosity value of 2.75, used in the present model, is in the typical range for SOFC electrodes and provides the best agreement with the experimental results, as shown in Figure 3.8.

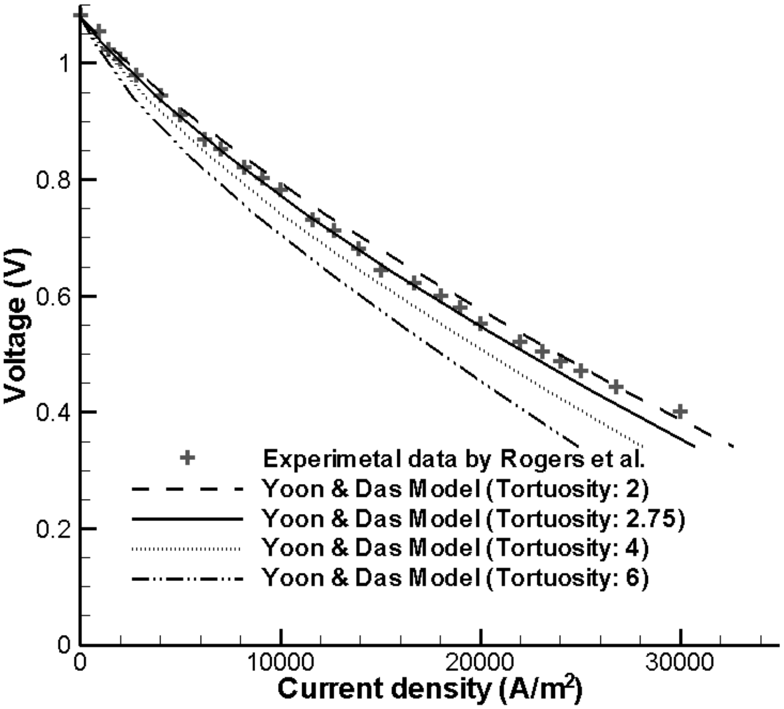

Figure 3.8 j-V curve for model and experimental data by Rogers et al..

<u>Second Experimental Validation</u>

Experimental parameters input to model [36, 45] (From experimental measurement by Feng Zhao et al.) are as follows:

- Electrolyte thickness: 8 μm

- Anode electrode layer thickness: 1 mm
- Anode reaction zone layer thickness: 20 μm
- Cathode electrode layer thickness: 50 μm
- Cathode reaction zone layer thickness: 20 μm
- Anode porosity: 48 %
- Fuel composition: H_2 97 % H_2O 3 %
- Oxidant: air

The other input parameters to model are the same as in Table 3.1.

The value of tortuosity is varied as in the previous model validation. A tortuosity value of 3, used in the present model, is in the typical range for SOFC electrodes and provides the best agreement with the experimental results, as shown in Figure 3.9.

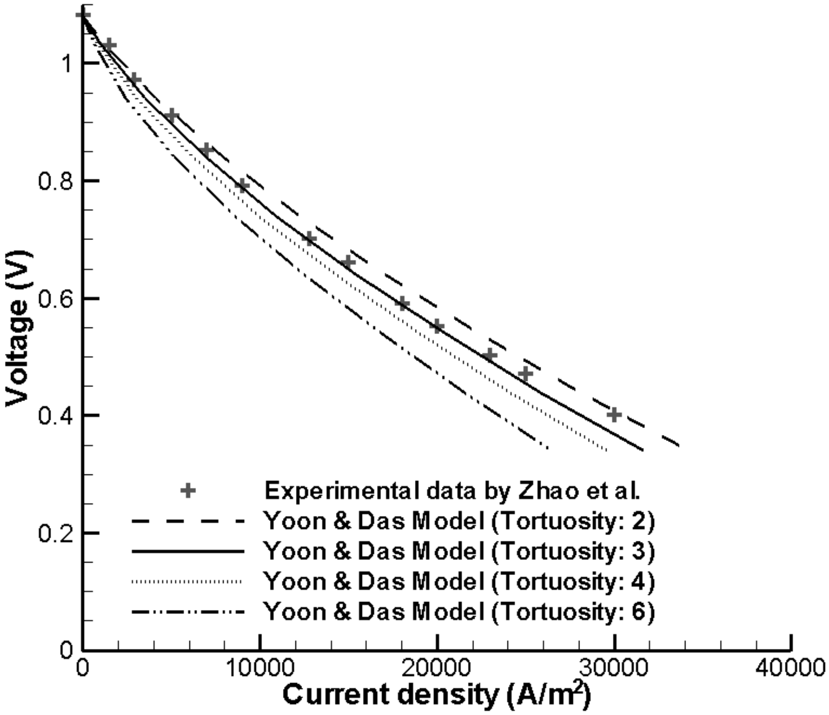

Figure 3.9 j-V curve for model and experimental data by Zhao et al..

3.1.3.3. Microarchitectured SOFC Structure

A cylindrical pore channel is applied in the center of the anode layer as shown in Figure 3.10. A gap between the anode-electrolyte interface and the cylindrical pore bottom is included in order to provide a space for the electrochemically active region. The diameter of the cylindrical pore channel is varied from 100 to 900μm in order to investigate the effect of the size of the cylindrical pore channel.

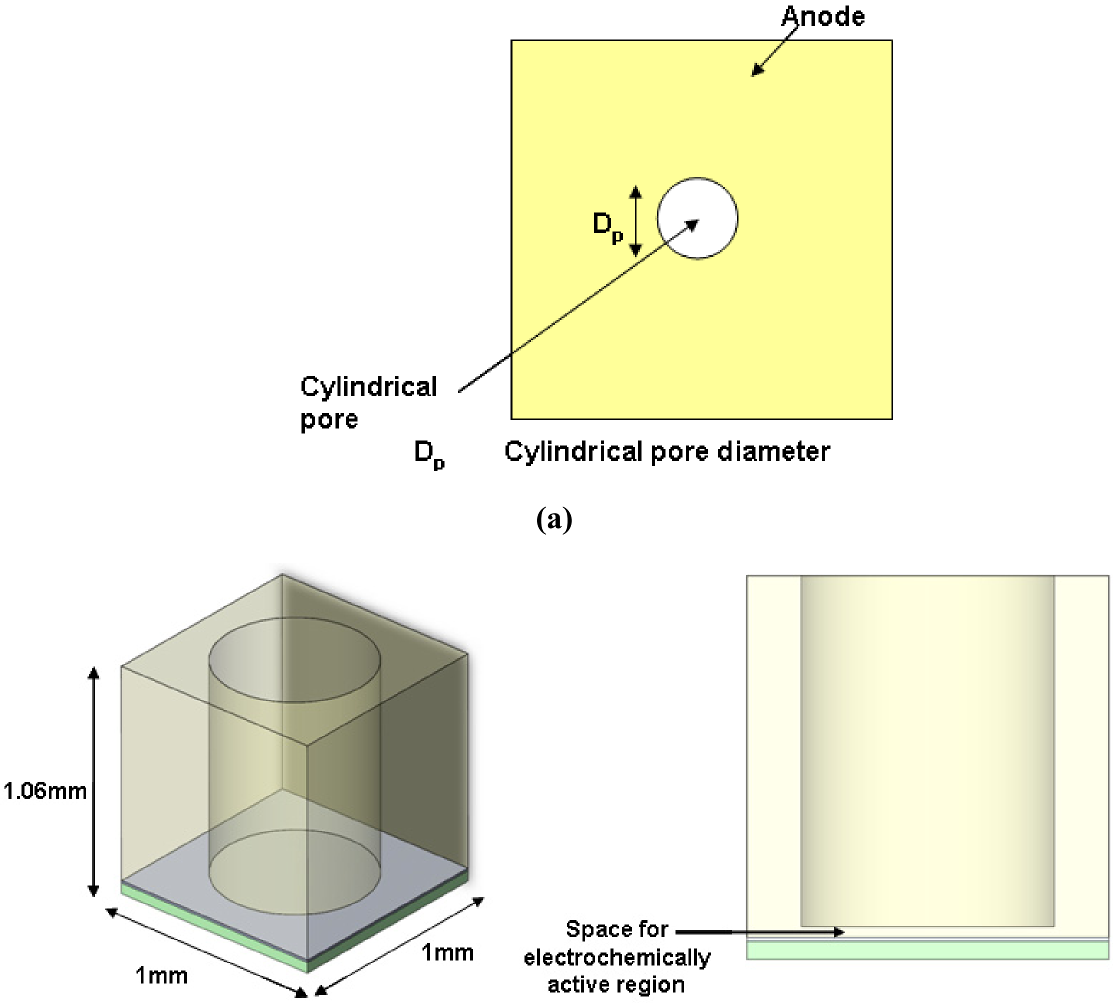

(a)

(b) (c)

Figure 3.10 SOFC with a cylindrical pore channel on the anode side (a) Top view, (b) Isometric view, and (c) Side view.

Through electronic current density distributions in the anode, cathode, and electrolyte along the cell thickness direction as shown in Figures 3.5 and 3.6, it can be found that the electronic current density is saturated near the electrode-electrolyte interface. This saturation current density, multiplied by the operating voltage, will be the power density of the SOFC cell. The saturation current density at the typical operating voltage of SOFCs, 0.7V, is plotted against the diameter of the microarchitectured pores in Figures 3.11 and 3.12 with the assumption of 10μm thick reaction zone layer and 20μm thick reaction zone layer, respectively.

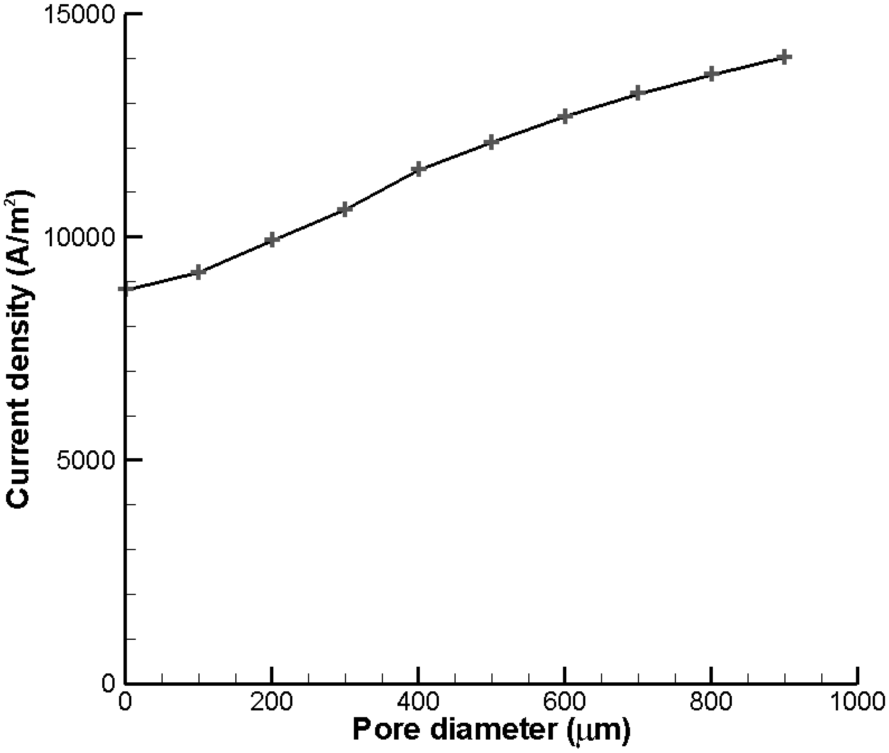

Figure 3.11 Current density vs. cylindrical pore diameter with the assumption of 10μm thick reaction zone layer.

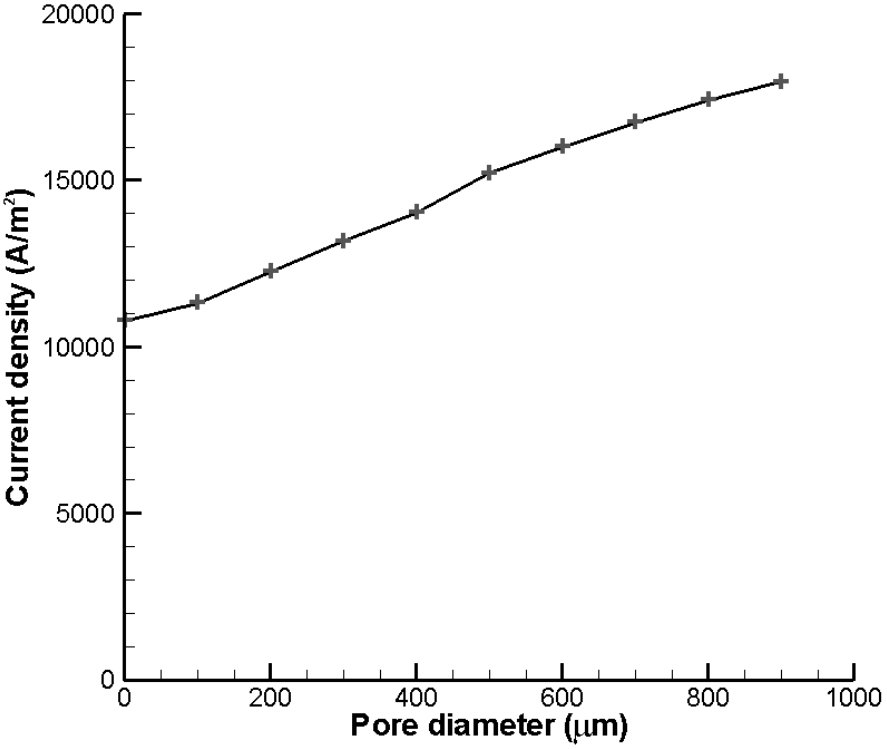

Figure 3.12 Current density vs. cylindrical pore diameter with the assumption of 20μm thick reaction zone layer.

The plots show continuous and smooth variation of the current density as a function of pore diameter consistent with the model's predictions. The saturation current density is proportional to the diameter of the microarchitectured pore. With a 10μm thick reaction zone layer and a 900μm diameter pore channel, an improvement in the current density of 59% over the baseline structure is achieved. With a 20μm thick reaction zone layer and a 900μm diameter pore channel, an improvement in the current density of 66% over the baseline structure is achieved.

Next, an array of cylindrical pore channels is applied, keeping the pore area fraction the same as for the 900μm diameter cylindrical pore channel. Pore channel arrays of 2×2, 3×3, and 4×4 configurations are considered as described in Figure 3.13.

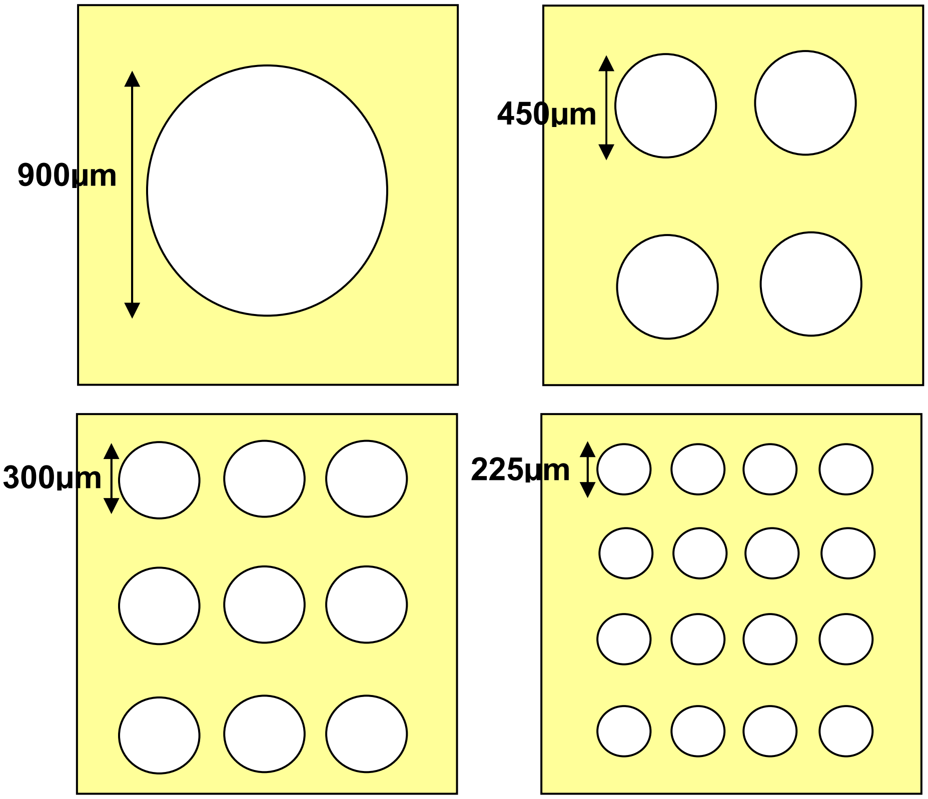

Figure 3.13 Top view of anode and cylindrical pore channels.

The saturation current density at the typical operating voltage of SOFCs, 0.7V, is plotted against the number of anode cylindrical pores in Figures 3.14 (a) and (b) with the assumption of a 10µm thick reaction zone layer and a 20µm thick reaction zone layer, respectively. The saturation current density is increased as the number of anode cylindrical pores is increased. With the 10µm thick reaction zone layer and a pore channel array of 4×4 configuration, an improvement in the current density of 62% over the baseline structure is achieved. With the 20µm thick reaction zone layer and a pore channel array of 4×4 configuration, an improvement in the current density of 70% over the baseline structure is achieved.

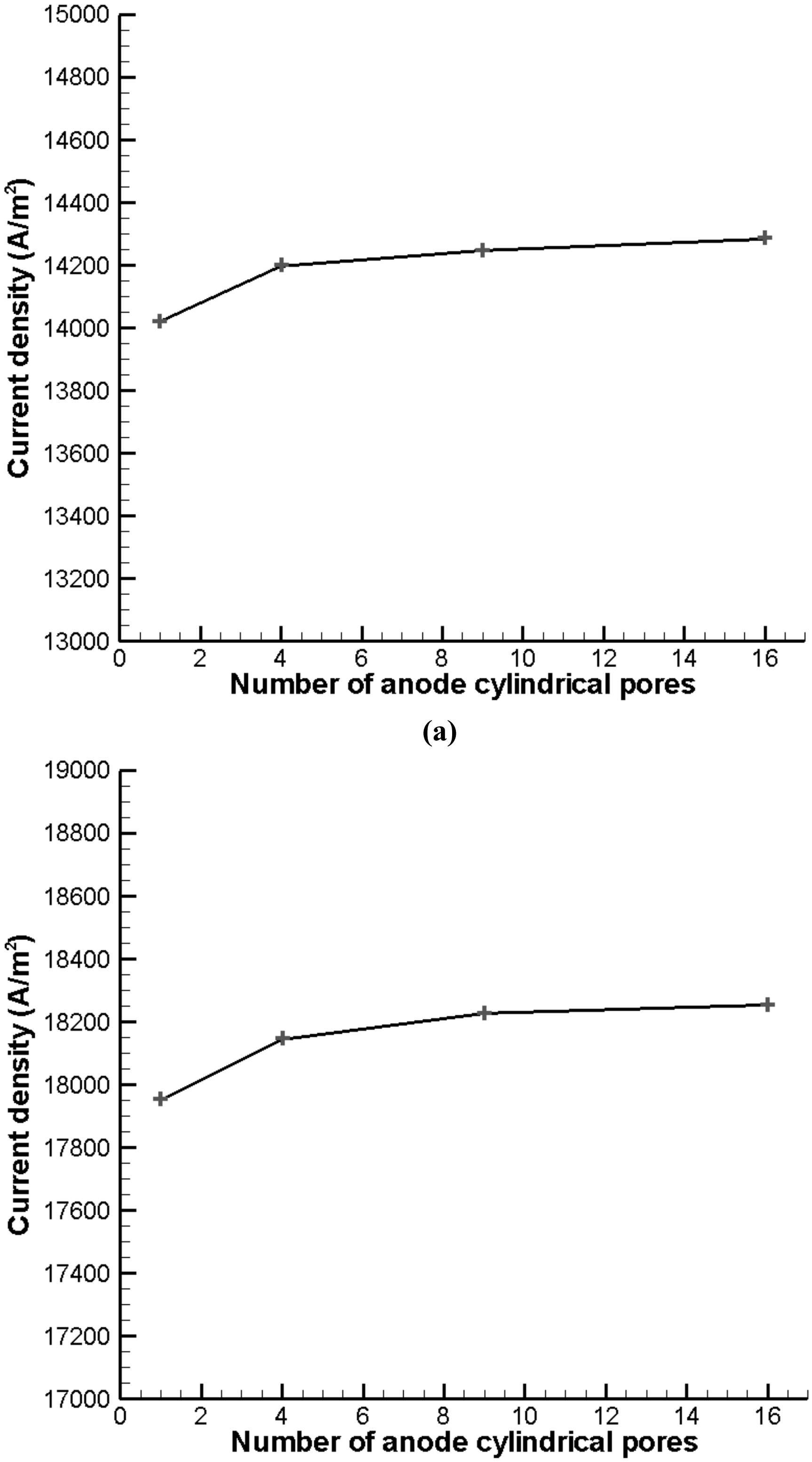

(a)

(b)

Figure 3.14 Current density vs. number of cylindrical pores (a) with the assumption of 10µm thick reaction zone layer and (b) with the assumption of 20µm thick reaction zone layer.

The improvement in current density flattens out after a pore channel array of 3×3 configuration. There is no significant difference between pore channel arrays of 3×3 configuration and 4×4 configuration. The incremental improvement in the current density of less than 0.3 % between pore channel arrays of 3×3 configuration and 4×4 configuration is achieved. This result indicates that there is no more significant effect on distributing the pore area evenly throughout the entire anode layer after a pore channel array of 3×3 configuration.

The distributions of species concentration in the anode are shown in Figure 3.15 and 3.16. In Figure 3.15 (a), the H_2 concentration of the baseline structure reduces rapidly along the z direction. In Figure 3.15 (b), the H_2 concentration of the SOFC with a pore channel array of 4×4 configuration is more uniform throughout the entire anode layer than the baseline structure. This can be observed when comparing the minimum concentrations of baseline structure and the SOFC with a pore channel array.

When the H_2 concentration in the reaction zone layer is integrated, there are 1.98E-10 mol and 2.17E-10 mol of H_2 in the reaction zone layer for the baseline structure and the SOFC with a pore channel array, respectively.

In Figure 3.16 (a), the H_2O concentration of the baseline structure rises along the z direction in contrast to the H_2 concentration. Similar to H_2 concentration, the H_2O concentration of the SOFC with a pore channel array of 4×4 configuration is more uniform throughout the entire anode layer than the baseline structure in Figure 3.16 (b). This can be observed by comparing the maximum concentrations of the baseline structure and the SOFC with a pore channel array.

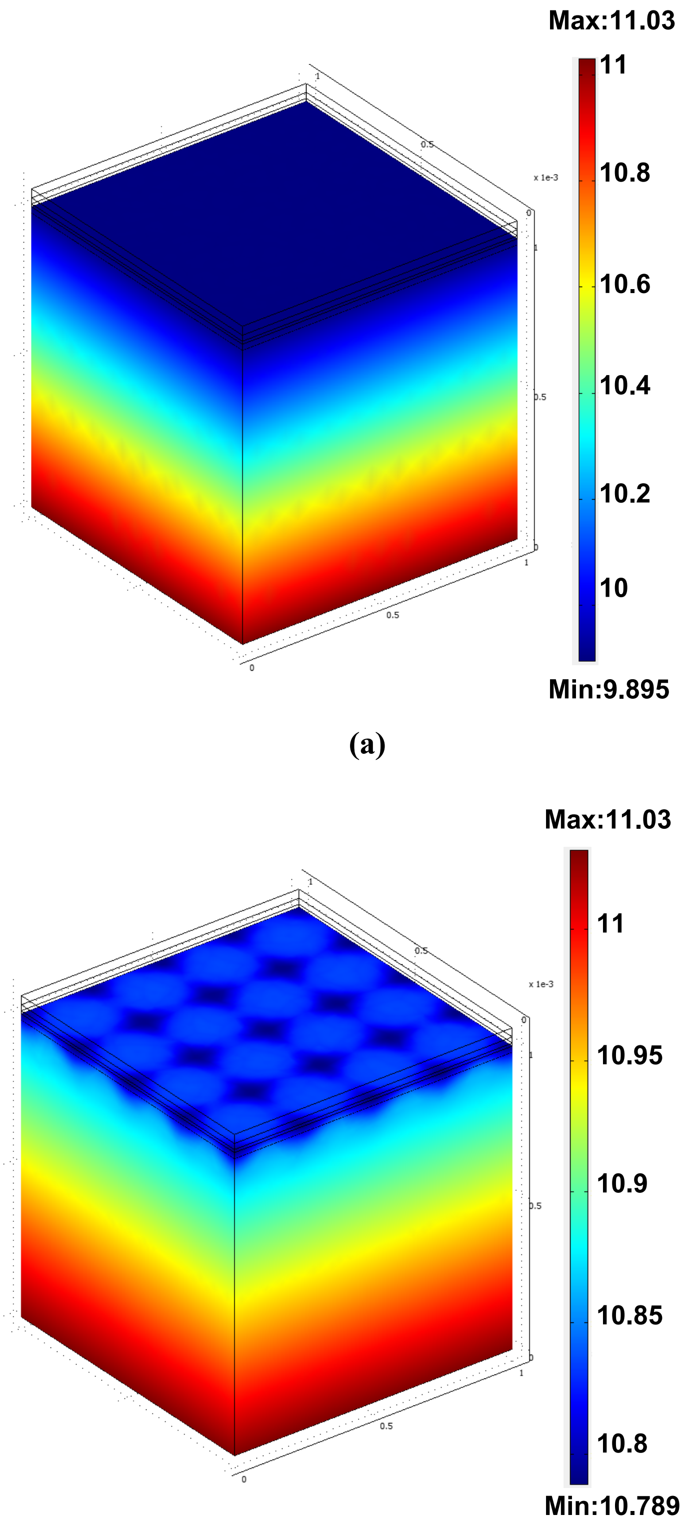

(a)

(b)

Figure 3.15 H_2 concentration (mol/m^3) of (a) baseline structure and (b) SOFC with a pore channel array of 4×4 configuration (20µm thick reaction zone layer).

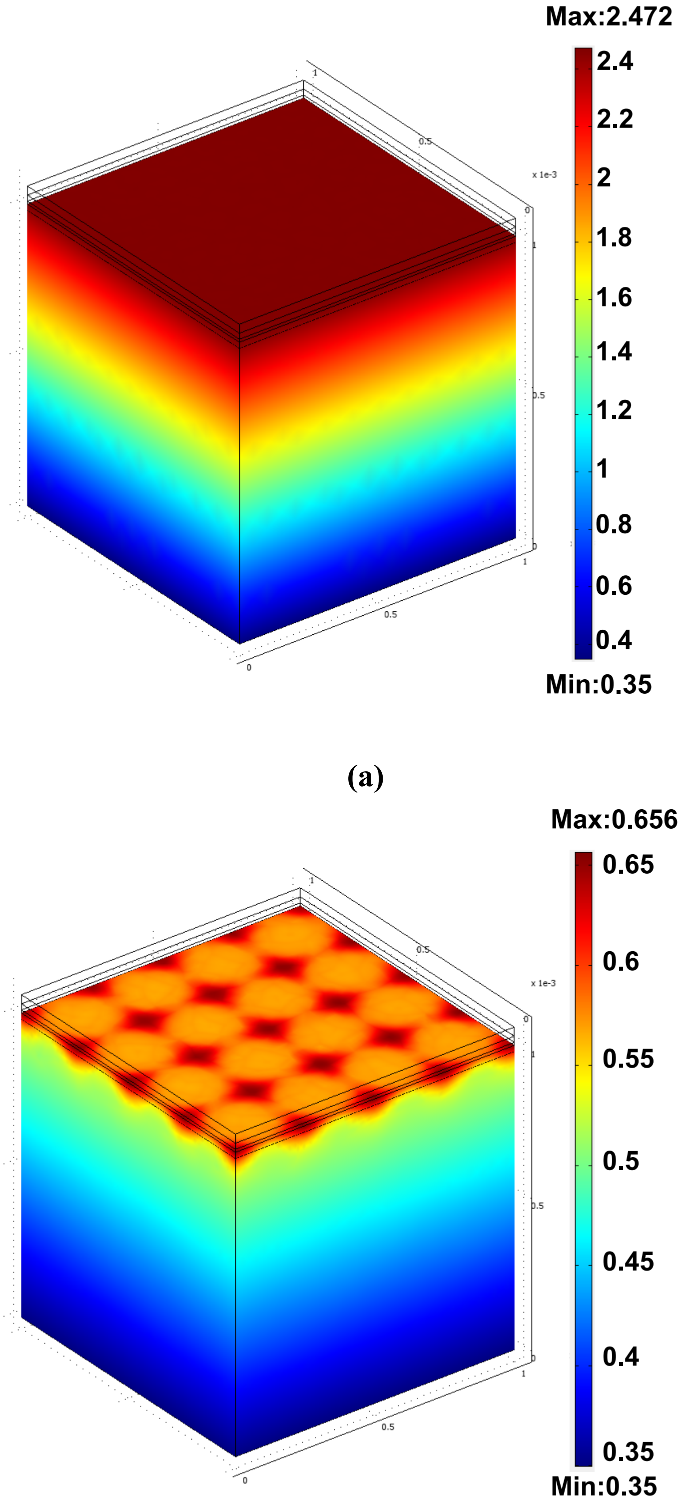

(a)

(b)

Figure 3.16 H_2O concentration (mol/m^3) of (a) baseline structure and (b) SOFC with a pore channel array of 4×4 configuration (20μm thick reaction zone layer).

When the H_2O concentration in the reaction zone layer is integrated, there are 4.92E-11 mol and 1.14E-11 mol of H_2O in the reaction zone layer for the baseline structure and the SOFC with a pore channel array, respectively.

Therefore, it is observed that with pore channels, reactants can easily reach the reaction active region, and products can also be removed faster through pore channels from the reaction active region.

3.2. Analysis of Thermal Stresses

This section presents the analysis of thermal stresses in the microarchitectured SOFC. The objective is to examine the possibility of failure due to the presence of designed pore channels.

3.2.1. Modeling Assumptions and Model Geometry

The assumptions made in this analysis are as follows:

- The model is assumed to be isothermal and at steady state.
- The thermal expansion coefficients are constant over the considered range of temperature, e.g. values from the literature applicable over a range of 273-1300K.
- The value of Young's modulus and Poisson's ratio at room temperature are used. Their precise dependency on temperature is not modeled.
- The value of the zero stress temperature is of the highest importance for the determination of the magnitude of the stresses. A uniform zero-stress temperature of 1400K is used in the present study.

The value of the zero stress temperature is of the highest importance for the determination of the magnitude of the stresses. Numerical computation is carried out for ΔT = -1102°C. In reference to the physical problem, this means the stress-free state is assumed at the manufacturing temperature at which the layers are joined (1400K) and the thermal stresses are examined at the room temperature (298K).

Due to symmetry, one quarter of the cell is modeled as shown in Figure 3.17. The anode-supported button cell is modeled with a 1mm thick Ni-YSZ anode, a 10μm thick YSZ electrolyte, and a 50μm thick LSM-YSZ cathode. The diameter of the anode-supported button cell is 10mm and the cathode area is 0.3cm^2. The gap between the anode-electrolyte interface and the cylindrical pore bottom is 20 μm. The diameter of the cylindrical pore channel is 225μm.

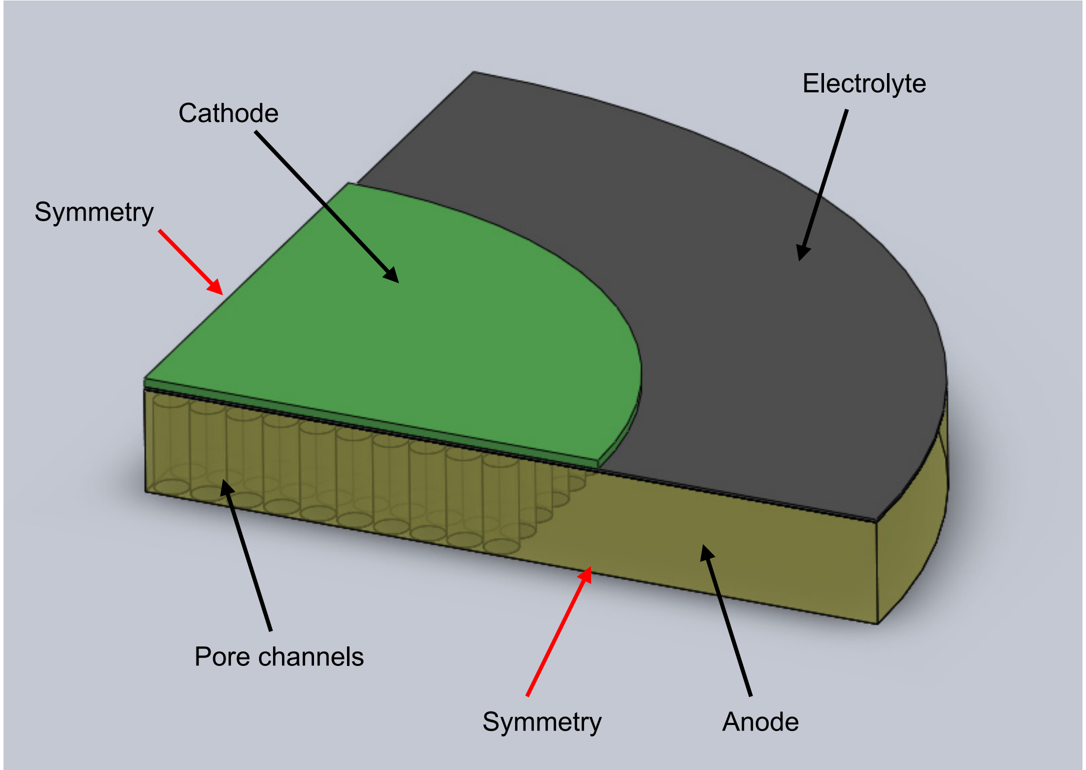

Figure 3.17 Model geometry.

Simulations have been conducted using ABAQUS commercial software using published input parameters [46-50].

Table 3.2 Material properties of SOFC components [46-50].

Component	Young's modulus, *E* (GPa)	Poisson's ratio, υ	Coefficient of thermal expansion, α ($\times 10^{-6}K^{-1}$)	Modulus of rupture (MPa)
Cathode (LSM)	35	0.25	11.7	46
Electrolyte (YSZ)				
1073K	183	0.313	10.8	377
298K	212	0.32		
Anode (NiO-YSZ)	57	0.28	12.2	56

3.2.2. Simulation Results

Fracture in the ceramic will occur when the maximum principal stress exceeds the modulus of rupture or the ultimate tensile strength of the ceramic [51]. The distribution of the maximum principal stresses is shown in Figure 3.18. The largest maximum principal stress, located at the interface between electrolyte and anode, is 47.62MPa. This stress value is below the modulus of rupture of the NiO-YSZ anode, which is 56MPa. This indicates there is no fracture with porous channels being present.

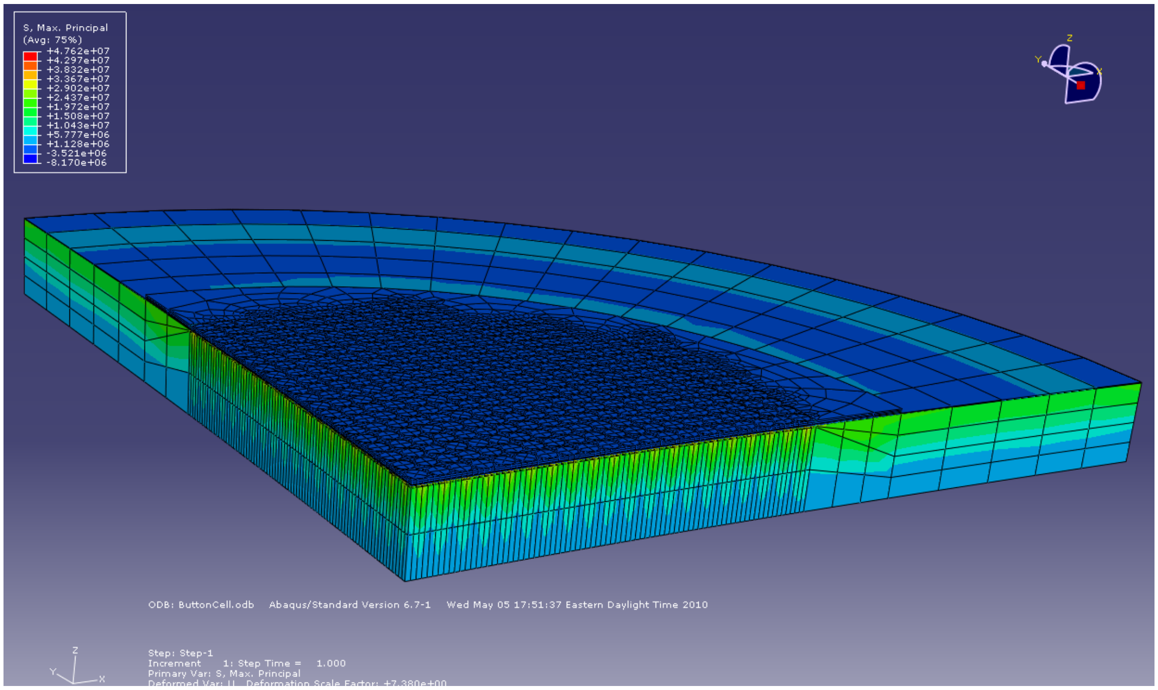

Figure 3.18 Distribution of the maximum principal stress.

3.3. Conclusions

A fundamental computational model-based approach to enhance the performance of SOFCs with microarchitectured design was developed. The SOFC model developed during this work was validated against two different sets of published experimental data. The performance of microarchitectured SOFCs was optimized in order to achieve higher power density than currently attainable in state-of-the-art SOFCs. An improvement of 60~70% in the current density was predicted by using porous channels in the anode layer over the baseline structure.

Furthermore, the analysis of thermal stresses in the microarchitectured SOFC was investigated to examine the possibility of failure due to the presence of designed pore channels. The result indicated there is no fracture with porous channels being present.

CHAPTER 4

FABRICATION AND CHARACTERIZATION

The objective of this chapter is to prove that the performance of microarchitectured SOFCs can be improved as predicted by the fundamental computational model. As a proof-of-concept, a real and specific SOFC is chosen, fabricated and characterized. Furthermore, the developed fundamental computational model is applied to this SOFC. Experimentally measured performance data is compared against the model's predictions. This chapter describes the SOFC button cell fabrication technique using sintering and laser ablation, pore size and geometry characterization using interferometry-based surface profilometry and scanning electron microscopy, SOFC button cell performance testing including power output performance and electrochemical impedance spectroscopy, and modeling of a realistic SOFC button cell.

4.1. Fabrication of Anode-supported Button Cell

As mentioned in chapter 2, in a majority of conventional techniques used to fabricate SOFCs, SOFC components are mixed with molten resin before processing. This results in tortuous porosity pathways and random distribution of electronically conducting networks in the electrodes. The fabrication of a SOFC with intentionally designed conducting wires and porous channels is nearly impossible using these techniques. Therefore, new and novel fabrication techniques that enable controlled distribution of SOFC materials are needed. Alternatively, additional fabrication processes should follow conventional techniques. In this study, anode-supported SOFC button cells are first fabricated by powder pressing and sintering. Laser ablation techniques are investigated to produce pore channels in the SOFC anode layer due to relatively easier fabrication. The fabrication of SOFC button cells consists of three main steps as follows.

4.1.1. Fabrication of NiO-YSZ Anode Supports

NiO and YSZ in a weight ratio of 65:35 with 5wt% corn starch are used as the raw materials. Starch is used as a pore former to enhance the porosity of the Ni/YSZ anode. Button anode supports are processed by pressing NiO-YSZ uniaxially under a pressure of 250MPa using a 13mm diameter die, and pre-calcined at 900°C for 2h in air.

4.1.2. Fabrication of YSZ Membrane on Anode Supports

A thin YSZ electrolyte on the button NiO-YSZ anode supports is prepared by a refined particle suspension coating technique [52]. The YSZ suspension is prepared by dispersing 3 g YSZ (TZ-8Y Tosoh, Japan) powders in 30 g ethanol with a small amount of organic ingredients, such as binder and dispersant, added. The YSZ membrane is then prepared by drop-coating the YSZ suspension on the button anode. The thickness of the YSZ membrane is exactly controlled by the volume of drop-coating. The coatings are dried in air for several minutes without any heating or cooling process and they are then co-sintered at 1400°C for 5 hours. The heating rate is 1°C / min before 550°C and 2°C / min from 550 to 1400°C.

4.1.3. Preparation of Cathode

Lanthanum strontium cobalt ferrite (LSCF) is used as the cathode. In order to avoid the reaction of LSCF and YSZ, a thin layer of $Sm_{0.2}Ce_{0.8}O_{1.95}$ (SDC) is used as the buffer layer, which is co-fired with LSCF at 1080°C for 2h. The cathode area is $0.3cm^2$.

The schematic of a fabricated anode-supported button cell with a 700µm thick NiO-YSZ anode, a 15µm thick YSZ electrolyte, a 2µm thick SDC buffer layer, and a 50µm thick LSCF cathode is shown in Figure 4.1.

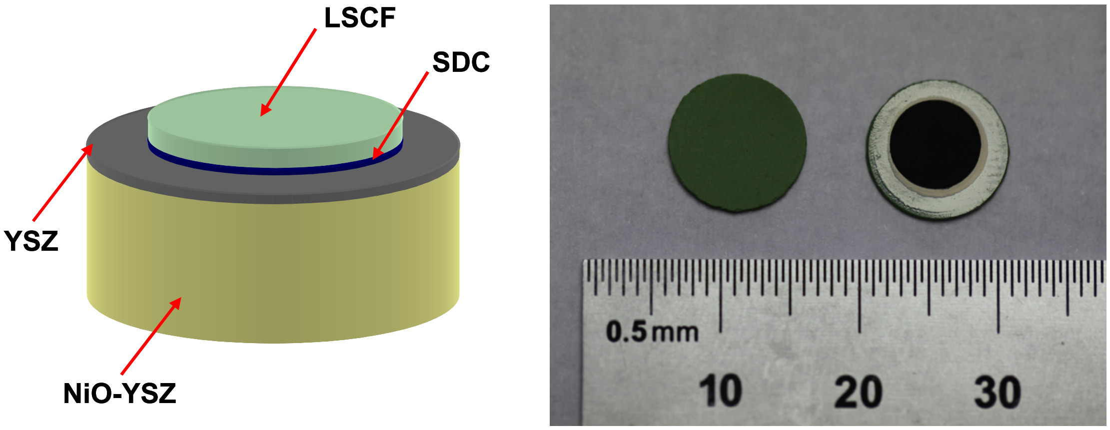

(a) (b)

Figure 4.1 (a) Schematic of anode-supported SOFC button cell and (b) actual fabricated button cell.

4.2. Fabrication of SOFC Microarchitectures Using Laser Ablation

4.2.1. Laser Ablation

Laser ablation is the removal of material from a surface as a result of absorption of laser radiation. The depth over which the laser energy is absorbed, and thus the amount of material removed by a single laser pulse, depends on the material's optical properties and the laser wavelength. The simplest application of laser ablation is to remove material from a solid surface in a controlled fashion. Laser machining and particularly laser drilling are examples; pulsed lasers can drill extremely small, deep holes through very hard materials. Solid-state lasers for materials processing are led by the Nd:YAG laser. Unlike the CO_2 laser, the Nd:YAG can be efficiently converted to its harmonic wavelengths of 532, 355, and 266nm, particularly when it is operating in a pulsed Q-switched mode. This wavelength conversion feature permits more flexibility in applications. Another laser is the Ti:sapphire laser. The great advantage of this laser is its tunability near the fundamental wavelength of 800nm. The Ti:sapphire laser can also be efficiently frequency-doubled to provide tunable near-UV output. Additionally, mode locking of this laser creates femtosecond pulses [53]. The extremely high power density is available from femtosecond lasers. A femtosecond laser is able to ablate material with minimal damage to surrounding material.

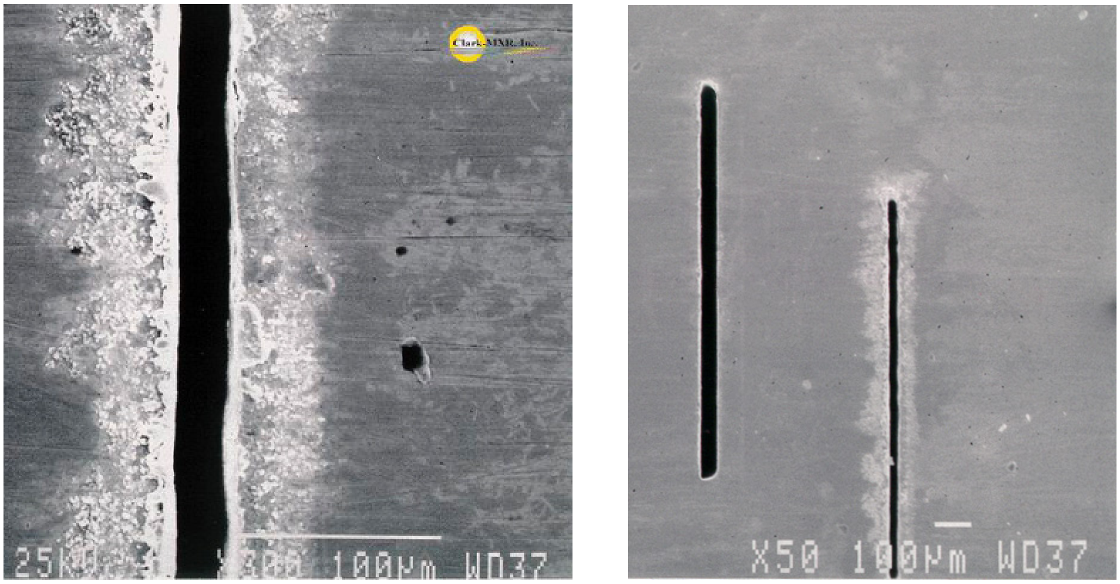

(a) (b)

Figure 4.2 Channels made in 1mm thick INVAR (nickel/iron alloy) (a) with long (nanosecond) pulses (b) with ultrafast (femtosecond) pulses [54].

Figure 4.2 (a) shows a channel made in 1mm thick INVAR (nickel/iron alloy) with long (nanosecond) pulses. It is observed that the machining process under these conditions is not very clean. A recast layer can be clearly seen near the edges of the channel. Figure 4.2 (b) describes a channel machined in 1 mm thick INVAR under the same experimental conditions as the long pulse channel in Figure 4.2 (a), but with ultrafast pulses. This channel was machined with 200 femtosecond pulses, 0.5mJ energy per pulse. It is obvious that the channel machined with femtosecond pulses is cleaner than the sample machined with nanosecond pulses. The absence of a recast layer can be also observed.

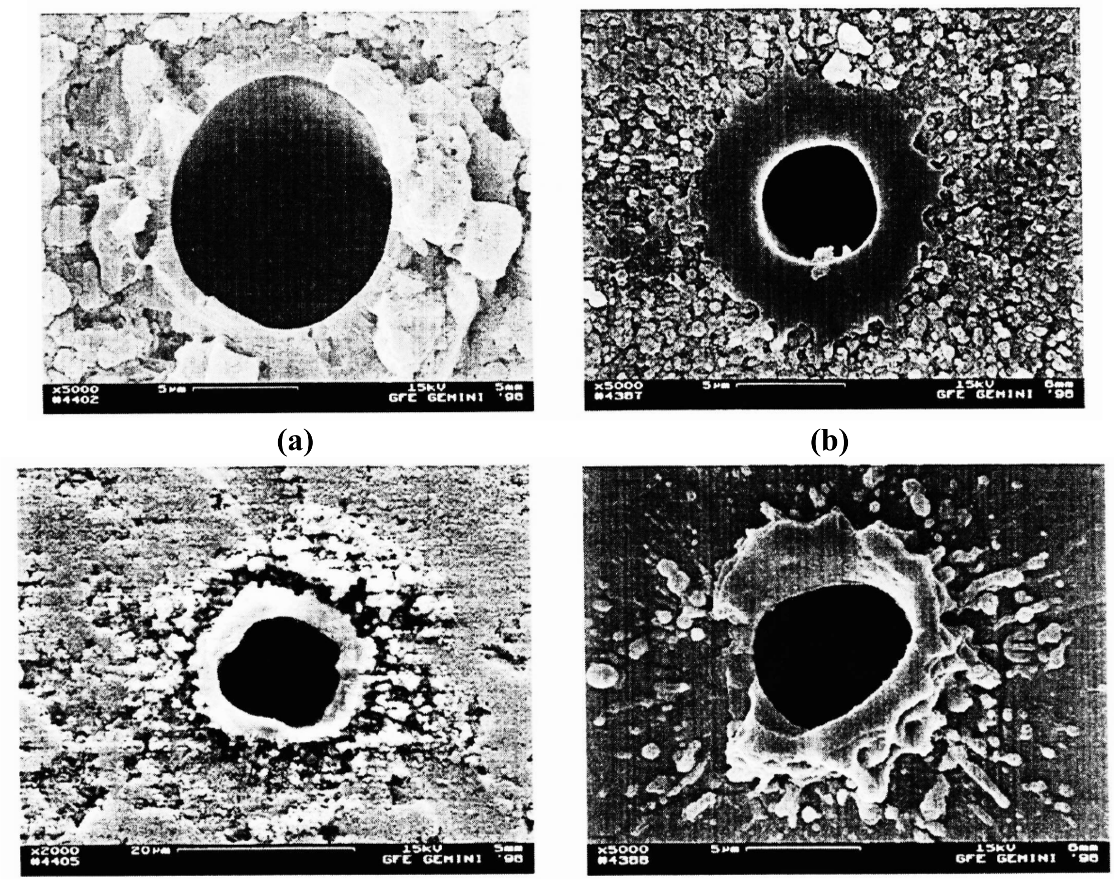

(a) **(b)**

(c) **(d)**

Figure 4.3 Holes in Al_2O_3: (a) entrance (b) exit (λ=355nm, f_p=5kHz, E_p=0.22mJ) and holes in ZrO_2: (c) entrance (d) exit (λ=355nm, f_p=5kHz, E_p=0.23mJ) [55].

Holes in Al_2O_3 and ZrO_2 with diameters ≥ 5µm and the thickness of 250µm were fabricated using a Nd:YAG laser by Hellrung et al. [55], as shown in Figure 4.3. The absorption of many ceramics is poor for the fundamental wavelength of the Nd:YAG laser. The frequency-tripled Q-Switch Nd:YAG laser was used since the absorption is higher in the UV-range.

Dear et al. [56] micromachined a zircornia ceramic using an Nd:YAG laser with millisecond pulses at 1064nm. Multipulse drilled holes and the internal surface of the drilled hole are shown in Figure 4.4.

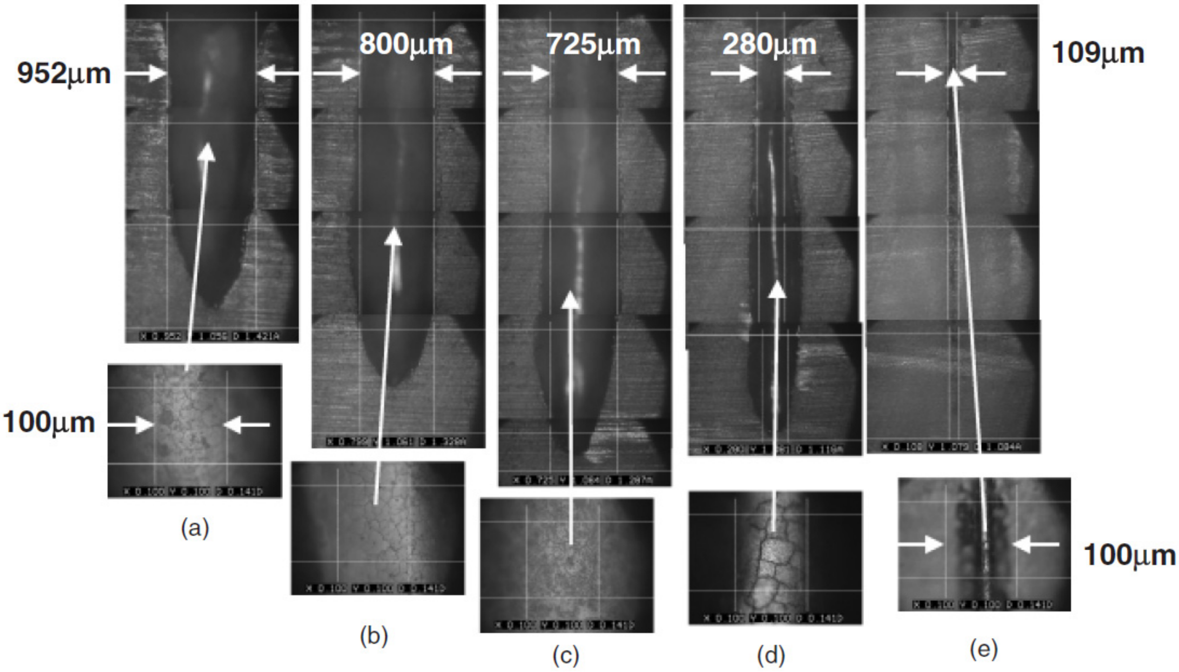

Figure 4.4 Multipulse (eight pulses) drilled holes in yttria-stabilized zirconia for (a) an 18.5J pulse energy with the sample 4mm below focus (b) 18.5J pulse energy with the sample 2mm below focus (c) 18.5J pulse energy with the sample on focus (d) an 8.5J pulse energy with the sample on focus, and (e) a 3J pulse energy with the sample on focus [56].

Shah et al. [57] demonstrated that a femtosecond laser with a wavelength of 845nm, a pulse energy of 1.5mJ and a pulse duration of 110fs can be used to produce microscopic holes (<100µm diameter) with macroscopic depth (>1mm) in silicate glasses at atmospheric pressures, as shown in Figure 4.5. A femtosecond laser which delivered 775nm wavelength, 150fs pulses at 1kHz was used to machine holes of few tens of micrometers through glass plates of about 150µm thick by Kuriyama et al. [58].

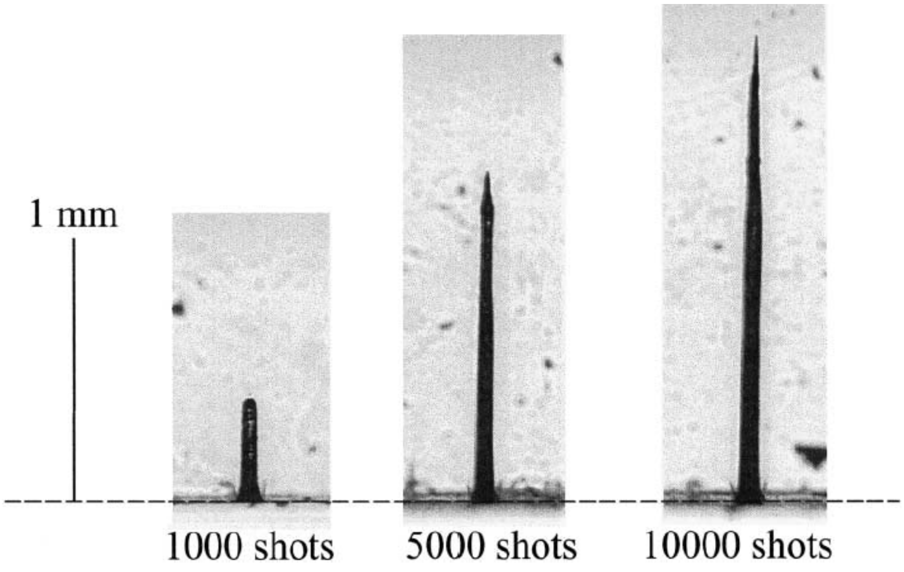

Figure 4.5 Femtosecond laser machined holes in soda-lime silicate glass [57].

A femtosecond laser located at Optical Direct-Write Materials Processing and Manufacturing Lab in the Georgia Institute of Technology was used to micromachine pore channels in the button cell. A schematic of the laser ablation setup is shown in Figure 4.6. A laser beam from a laser head is reflected by the reflection mirror and goes through a polarizer and a wave plate. The polarizer and the wave plate are used to adjust the laser power. After a beam splitter, 90% of the laser beam transmits and 10% is reflected to a power meter. The transmitted laser beam passes through a shutter which is used for controlling the exposure time. The laser beam is focused on the sample surface. In order to fabricate pore channel arrays of 20 × 20 in the sample, the sample is mounted on the 2-D stage to position the sample surface under the laser beam for each pore and to control the center-to-center distance between pore channels. The fabrication time per pore channel was 5s.

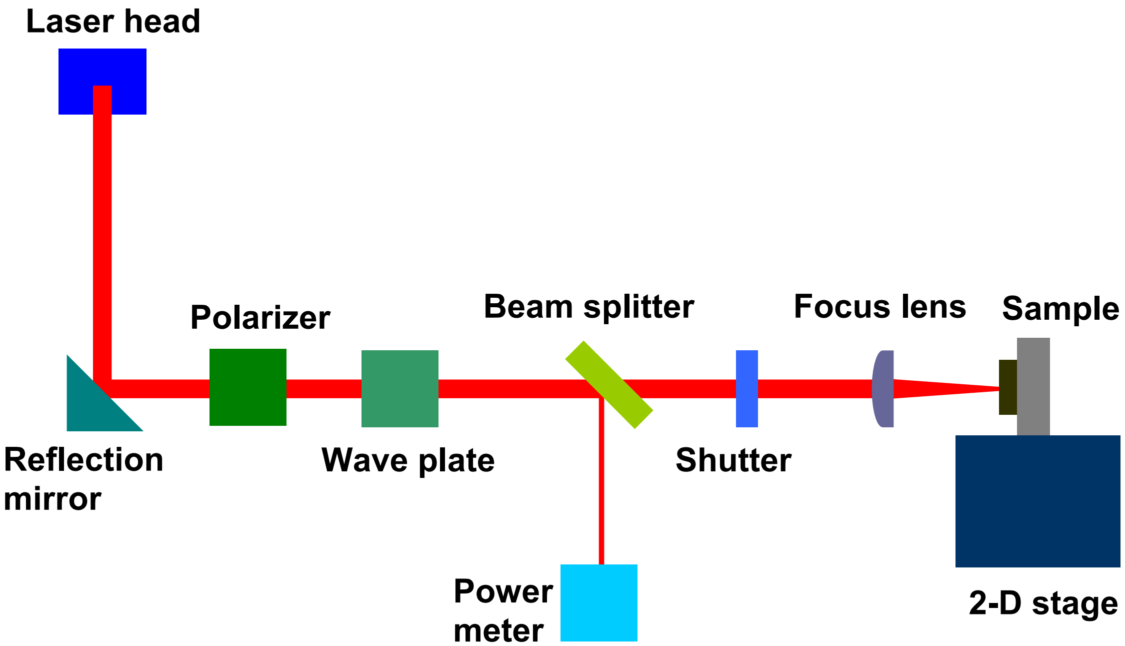

Figure 4.6 Schematic of laser ablation.

Laser processing parameters used for experiments are listed in Table 4.1.

Table 4.1 Laser processing parameters.

Wavelength (nm)	810
Pulse duration (fs)	95
Energy per pulse (mJ/pulse)	1
Repetition rate (kHz)	1
Beam diameter (mm)	10

4.2.2. Experimental Results

After a thin YSZ electrolyte has been formed on the button NiO-YSZ anode supports, pore channels are generated in button NiO-YSZ anode supports by using laser ablation. Subsequently, thin layers of SDC and LSCF are deposited on the YSZ electrolyte. Preliminary experiments were conducted in order to determine laser parameters for the desired diameter and depth of pore channels in the anode layer. A femtosecond laser described in section 4.2.1 is used. The laser power was set to 1W and exposure time was varied to achieve the desired diameter and depth of pore channels. A non-contact profilometer (Zygo, NewView 200) with sub-nanometer resolution in the vertical direction and sub-micrometer resolution in the lateral direction was used to measure the diameter and depth of the pore channels.

In Figure 4.7, it can be observed that the depth of the pore channels increases as the exposure time of the femtosecond laser is increased. The relationship between the exposure time and ablation depth is almost linear. With 6 sec exposure time, the depth of the pore channel is 550μm, which means that the gap between the electrolyte and the bottom of the pore channels is 150μm, since the thickness of the anode layer is 700μm.

Pore channel arrays of 20 × 20 are fabricated in the center of the anode layer. Figure 4.8 shows a macroscopic image of one such micromachined anode layer. Three anode-supported button cells were micromachined to have gaps of 150μm, 230μm, and 250μm between the electrolytes and the bottoms of the pore channels. The diameter of the fabricated pore channels was 225μm and the center-to-center distance of the pore channels was 250μm.

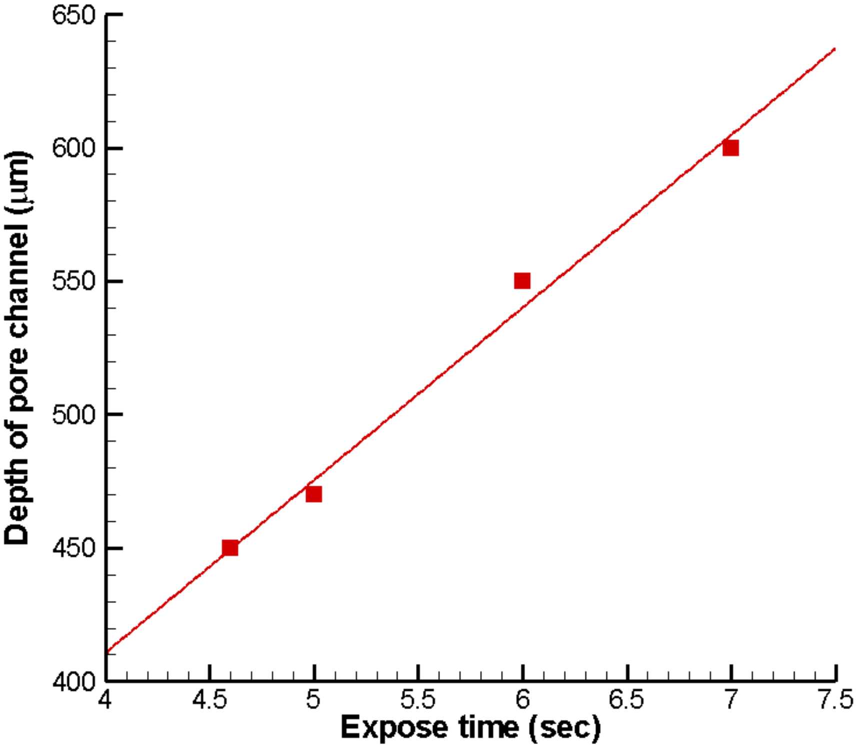

Figure 4.7 Depth of pore channel vs. exposure time.

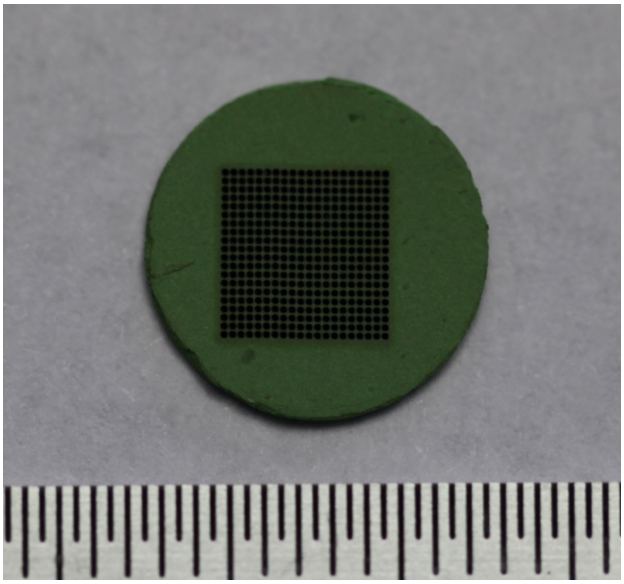

Figure 4.8 Magnified photograph of a laser micromachined anode layer showing 20×20 array of pore channels (Scale bar is in mm).

The shape of the micromachined pore channels was investigated using non-contact profilometry and scanning electron microscopy (SEM). Figure 4.9 shows the non-contact profilometer images. Figure 4.9 (a) is a top view and Figure 4.9 (b) is an oblique view plot. Figure 4.10 shows SEM images. Figure 4.10 (a) is a top view and Figure 4.10 (b) is a cross-sectional view.

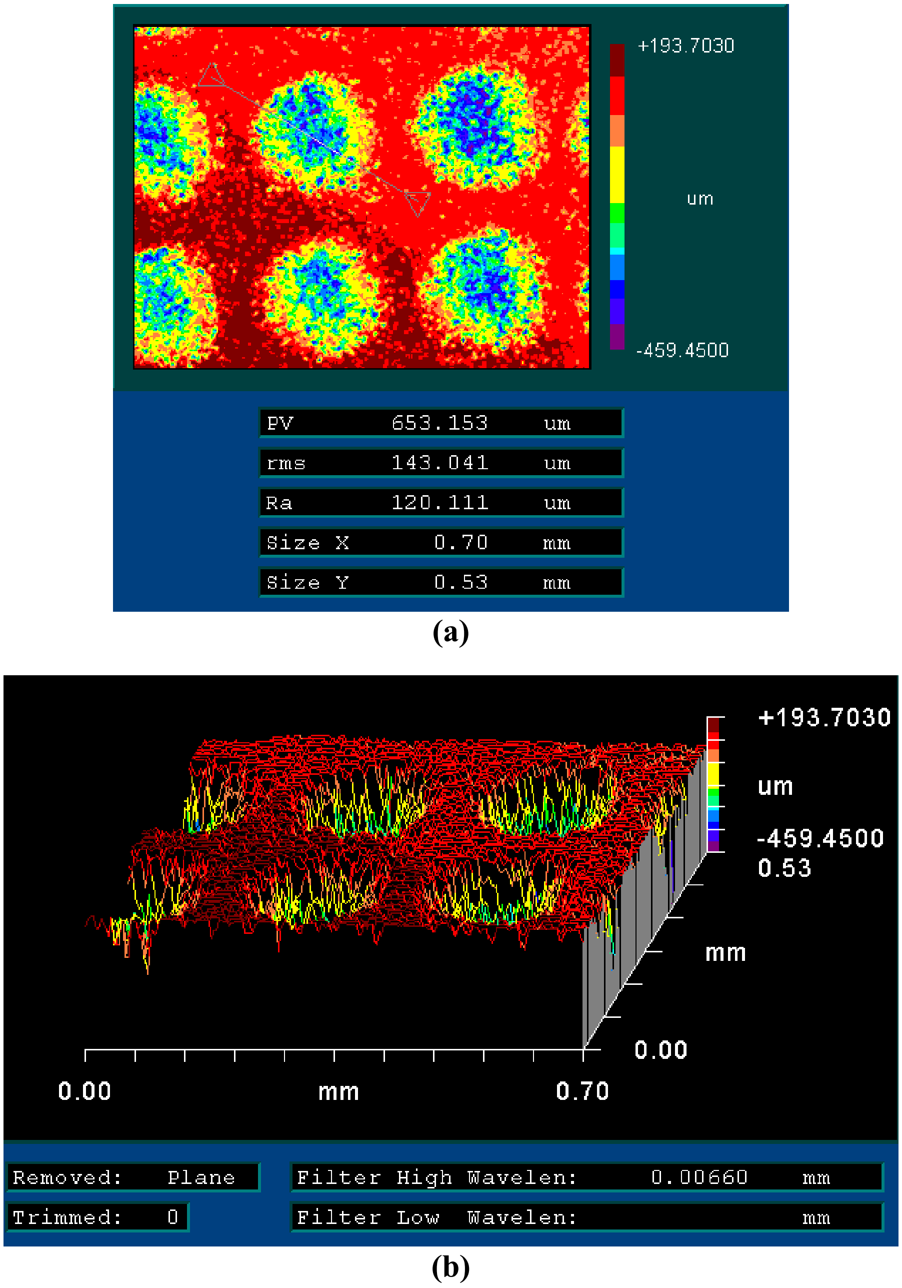

PV 653.153 um
rms 143.041 um
Ra 120.111 um
Size X 0.70 mm
Size Y 0.53 mm

Removed: Plane
Trimmed: 0
Filter High Wavelen: 0.00660 mm
Filter Low Wavelen: mm

Figure 4.9 Non-contact profilometer images of micromachined pore channels (a) top view (b) oblique view plot.

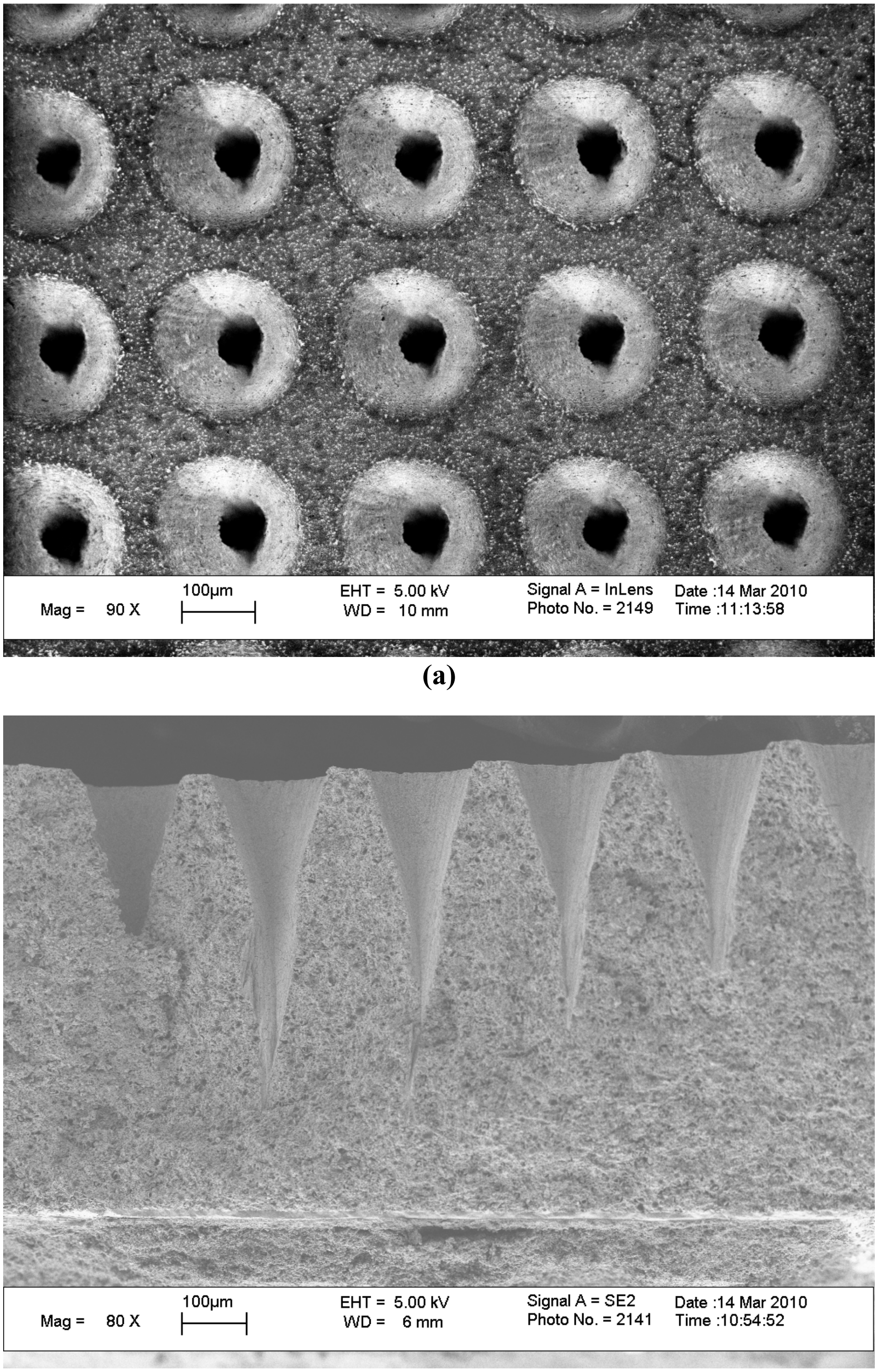

(a)

(b)

Figure 4.10 SEM images of micromachined pore channels (a) top view (b) cross-sectional view.

From these figures, it can be found that the shape of the pore channels produced by laser ablation is conical. Micromachined holes are uniform and regularly spaced. For micromachined SOFC button cells containing pore channels with the diameter of approximately 225μm and the depth of approximately 550μm, 50 pore channels were analyzed. The measured diameter is 222.5μm ± 2.8%. The measure depth is 551.3μm ± 3%. The absence of a recast layer can be also observed. The femtosecond laser micromachining technique is able to provide excellent repeatability. It is a good rapid prototyping technique.

4.3. Performance Testing

4.3.1. Test Procedure

The single cell was attached and sealed on an alumina tube by using ceramic paste and tested on a laboratory-developed-cell-testing system as shown in Figure 4.11. The cell was tested with humidified hydrogen (3% H_2O) as the fuel and ambient air as the oxidant. The cell was heated to 800°C and NiO was reduced to Ni in situ. The power output performances and AC impedance spectra were measured using a Solartron 1255 frequency response analyzer in combination with a potentiostat/galvanostat (EG&G PAR 273). The frequency range of electrochemical impedance spectroscopy (EIS) is 100kHz to 0.1Hz and the signal amplitude is 20mV. Button cells fabricated from the same batch were used for performance testing in order to avoid uncertain errors which can be generated during fabrication process and to minimize cell-to-cell difference.

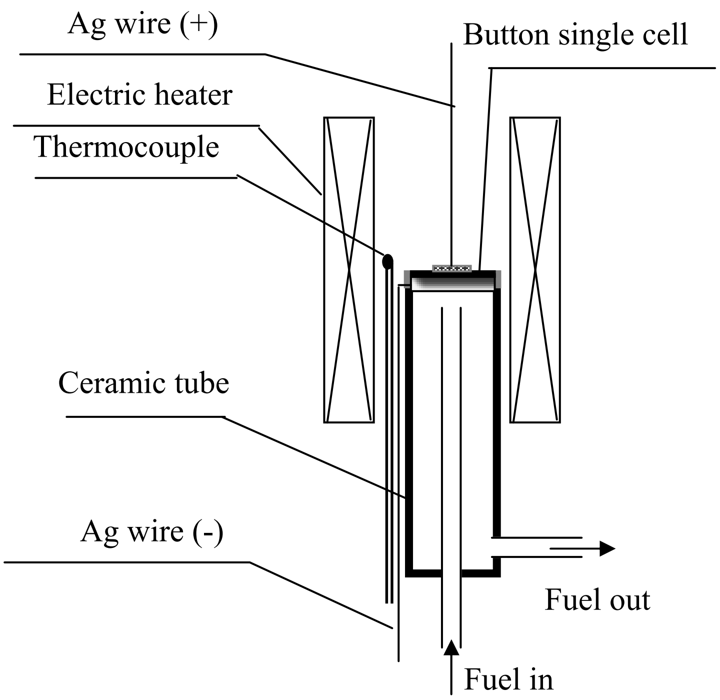

Figure 4.11 Schematic of single cell testing system.

4.3.2. Test Results

Performance characterization was executed with two kinds of electrochemical characterization techniques: The j-V characteristic measurement and EIS. One way to characterize the performance of a fuel cell consists of measuring a steady-state j-V curve, which is the most popular method. From such a curve, information about the entire fuel cell, comprising the sum of the electrochemical behavior of the electrode/electrolyte interfaces, conductivity of the electrolyte, the influences of the gas supply and the electrical contacts between individual components can be obtained [59]. Another method to characterize the performance is EIS. This more sophisticated technique can accurately differentiate between all the major sources of loss in a fuel cell [60].

4.3.2.1. j-V Characteristic

Figures 4.12-4.15 shows the measured j-V characteristics of the baseline button cell and micromachined button cells as a function of different fuel flow rates. Three micromachined anode-supported button cells, having 150μm, 230μm, and 250μm gaps between the electrolyte and the bottom of pore channels were tested. Different fuel flow rates were applied to each cell with 10, 20, 30, and 40 standard cubic centimeters per minute (sccm). For all fuel flow rate conditions at the same voltage, the micromachined cells have a higher current density than the baseline cells. The difference in current densities between the baseline and micromachined cells at the same voltage increases as the voltage drops. This result is reasonable since the concentration loss becomes dominant as the current density moves from low to high. The peak power densities of micromachined cells are larger than those of the baseline cell.

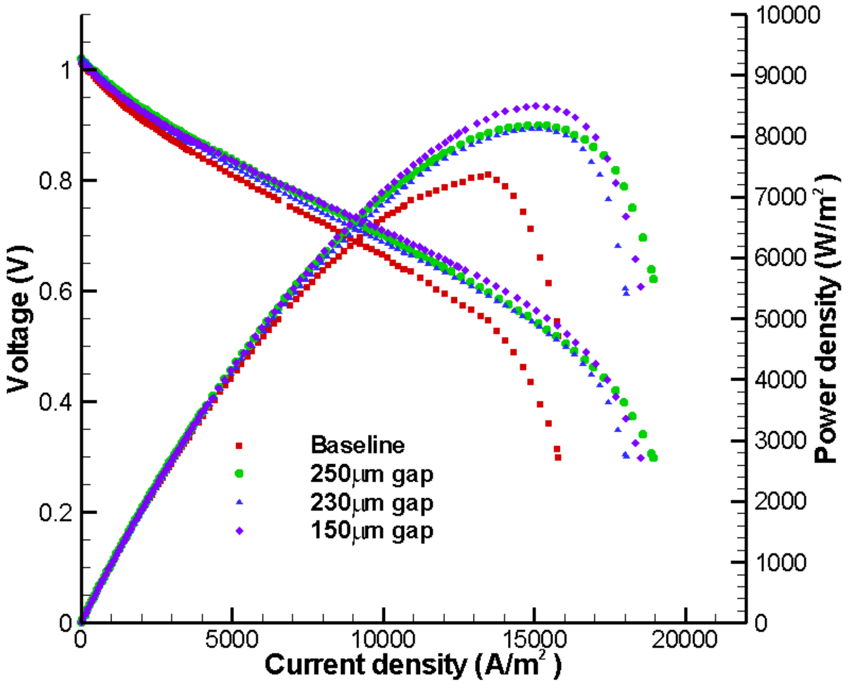

Figure 4.12 j-V characteristics of baseline and micromachined button cells with 10sccm fuel flow rate.

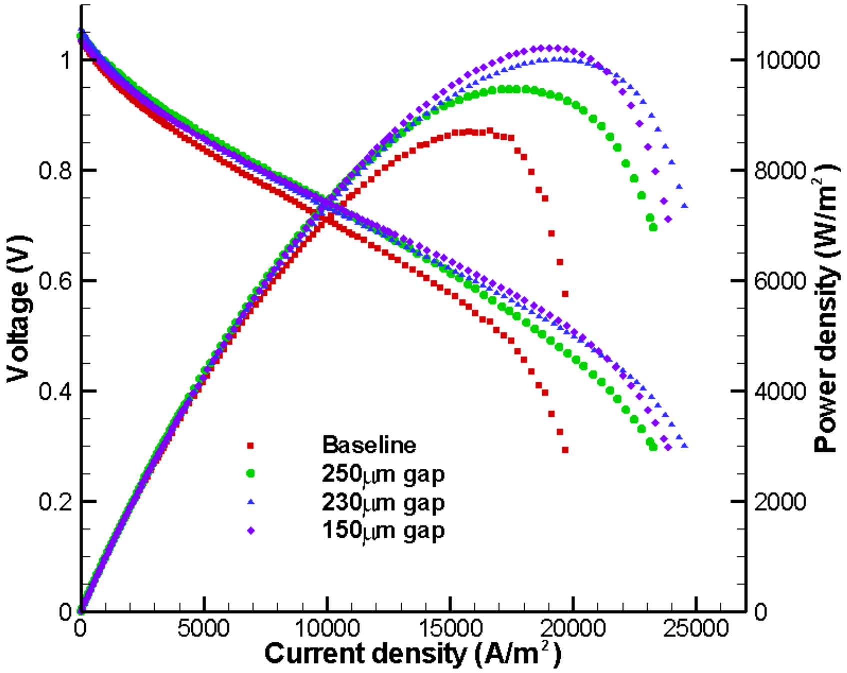

Figure 4.13 j-V characteristics of baseline and micromachined button cells with 20sccm fuel flow rate.

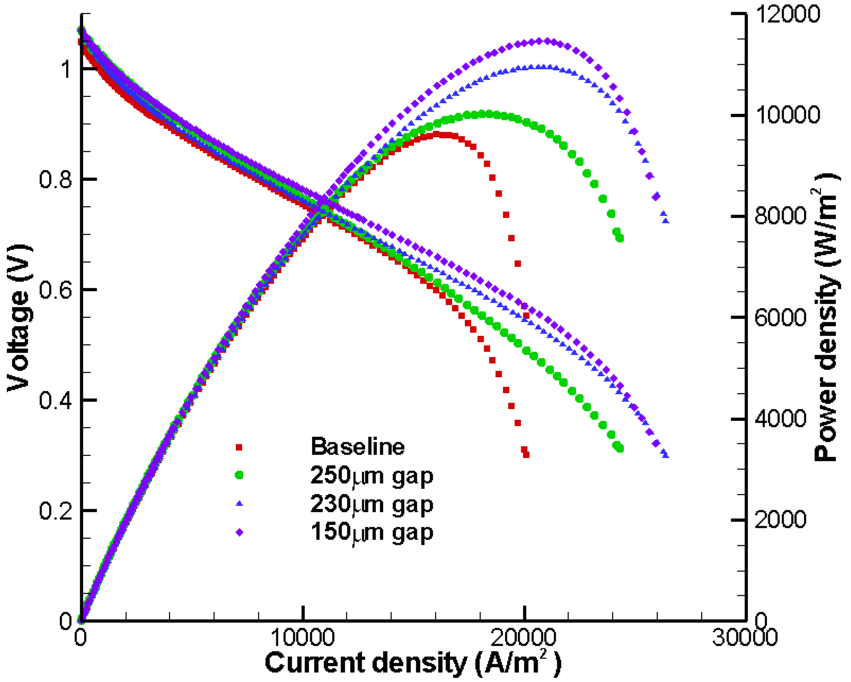

Figure 4.14 j-V characteristics of baseline and micromachined button cells with 30sccm fuel flow rate.

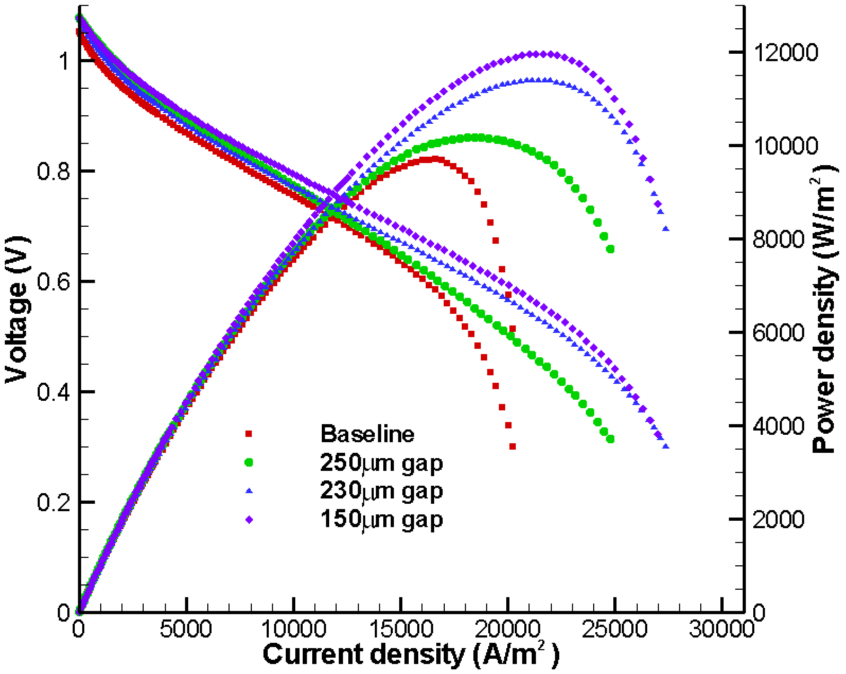

Figure 4.15 j-V characteristics of baseline and micromachined button cells with 40sccm fuel flow rate.

Figure 4.16 (a) shows the comparison of the current density at 0.7V between the baseline and the micromachined button cells at different fuel flow rates. The comparison is performed at 0.7V which is the typical operating voltage of SOFCs. As the fuel flow rate increases from 10 to 40sccm, the measured current density also increases. This indicates that an increase of flow rate decreases the overpotential related to gas diffusion at the electrode, because the increase in the diffusion of gas increases the gas exchange at the electrode [61]. It was also found that at the same fuel flow rate, micromachined cells have larger current density than the baseline cell. Furthermore, the increase in the performance of the micromachined button cell over the baseline button cell increases with a decrease of the gap between the electrolyte and the bottom of the pore channels. The smaller the gap between the electrolyte and the bottom of pore channels is, the more easily and faster the reactant can reach the reaction active region, which makes more chemical reactions occur at the reaction active region. Reaction products can also be removed faster through pore channels close to the reaction active region. These effects enhance the performance of micromachined button cells. However, the current density at 0.7V with a 250µm gap is a little higher than with 230µm gap at low flow rate (10 and 20sccm). With a 250µm gap, an averaged improvement in the current density of 9% over the baseline structure is achieved. With the 230µm gap, an average improvement in the current density of 9% over the baseline structure is achieved. With a 150µm gap, an average improvement in the current density of 17% over the baseline structure is achieved.

Figure 4.16 (b) describes the comparison of the peak power density between the baseline and the micromachined button cells at different fuel flow rates. Similar to the current density, the measured peak power density increases with an increase of flow rate. At the same fuel flow rate, micromachined cells have higher peak power density than the baseline cells. The micromachined button cell shows more improvement of the peak power density over the baseline button cell when the gap between the electrolyte and the bottom of the pore channels is decreased. With the 250µm gap, an average improvement in the peak power density of 7% over the baseline structure is achieved. With the 230µm gap, an average improvement in the peak power density of 14% over the baseline structure is achieved. With a 150µm gap, an average improvement in the peak power density of 19% over the baseline structure is achieved.

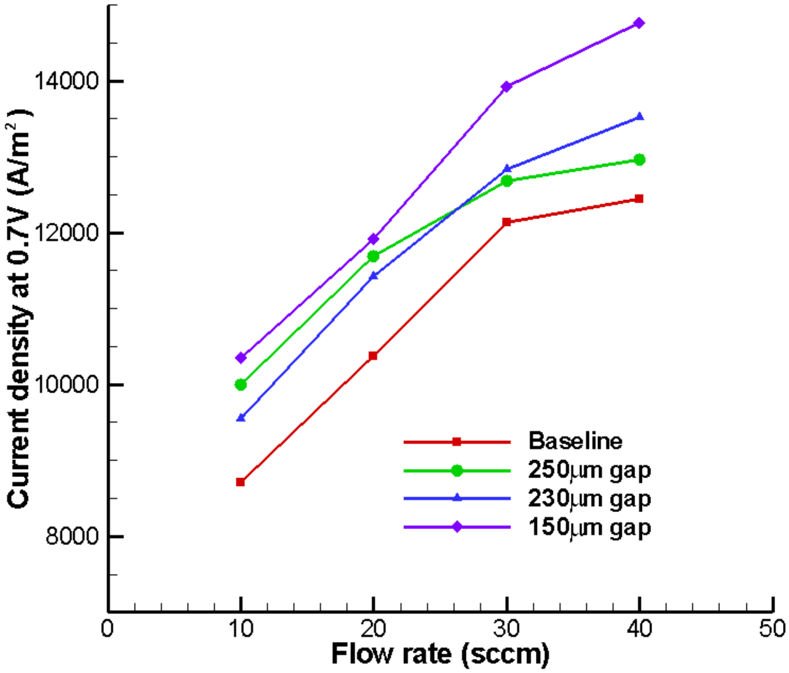

(a)

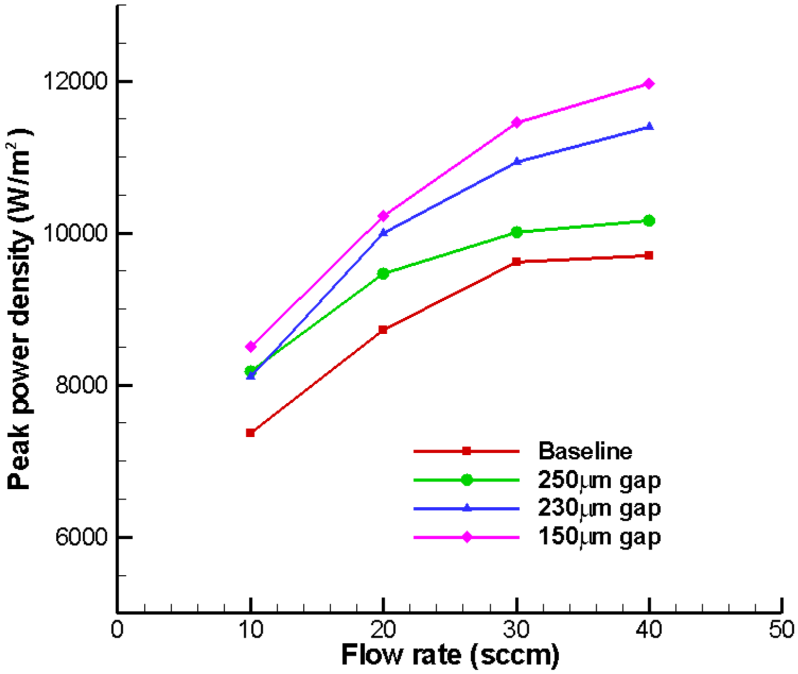

(b)

Figure 4.16 Comparison of j-V characteristic results (a) current density at 0.7V, and (b) peak power density.

4.3.2.2. Electrochemical Impedance Spectroscopy (EIS)

The impedance, Z, is a measure of the ability of a system to impede the flow of electrical current. A sinusoidal perturbation (usually a voltage perturbation) is applied to a system and the amplitude and phase shift of the resulting current response are measured. Measurements can be conducted over a wide range of frequencies, resulting in the construction of an impedance spectrum [60]. The following characteristic parameters are obtained from the impedance data:

1. The *polarization resistance*, R_p, which is responsible for the anode and cathode polarization losses. It can be determined by the distance from the high frequency real-axis impedance intercept to the low frequency real-axis impedance intercept (Figure 4.17).
2. The so-called *electrolyte resistance*, R_e, which is the ohmic resistance caused by a certain contribution of the electrolyte. It can be determined from the high frequency part of the Nyquist plot at the intersection of the impedance data with the real axis (Figure 4.17).

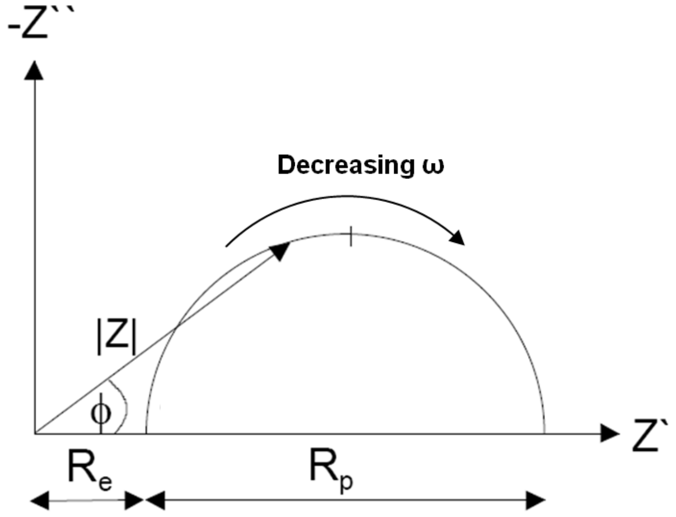

Figure 4.17 Schematic representation of Nyquist plot for a simple fuel cell [62].

Impedance measurements are conducted at open circuit voltage (OCV). Figure 4.18 shows EIS characterization results with the baseline button cell and the micromachined button cells with 150μm gap.

When the electrolyte resistance, R_e, is compared, both the baseline and the micromachined button cells have nearly the same value, approximately 0.2Ω/cm^2. Since these button cells were fabricated from the same batch of starting materials, this can be expected from the assumption of almost identical electrolytes in the baseline and the micromachined button cell.

When the polarization resistance, R_p, is compared at the same flow rate, the micromachined button cell has a smaller R_p than the baseline button cell. The percent decrease in R_P is relatively constant (22-26%) over the 10-40sccm range of fuel flow rates tested, as shown in Table 4.2.

Table 4.2 Polarization resistance, R_P (Ωcm^2) vs. Flow rate (sccm).

Flow rate (sccm)	Polarization resistance, R_p (Ωcm^2)		Decrease in R_p (%)
	Baseline cell	Micromachined cell	
10	0.62	0.46	25.8
20	0.69	0.525	23.9
30	0.73	0.56	23.3
40	0.77	0.6	22.1

Since the button cells were fabricated from the same batch, it can be assumed that the electrolytes and cathodes of the baseline and micromachined button cells are the same, and the only difference arises from microachitecture in the anode layer.

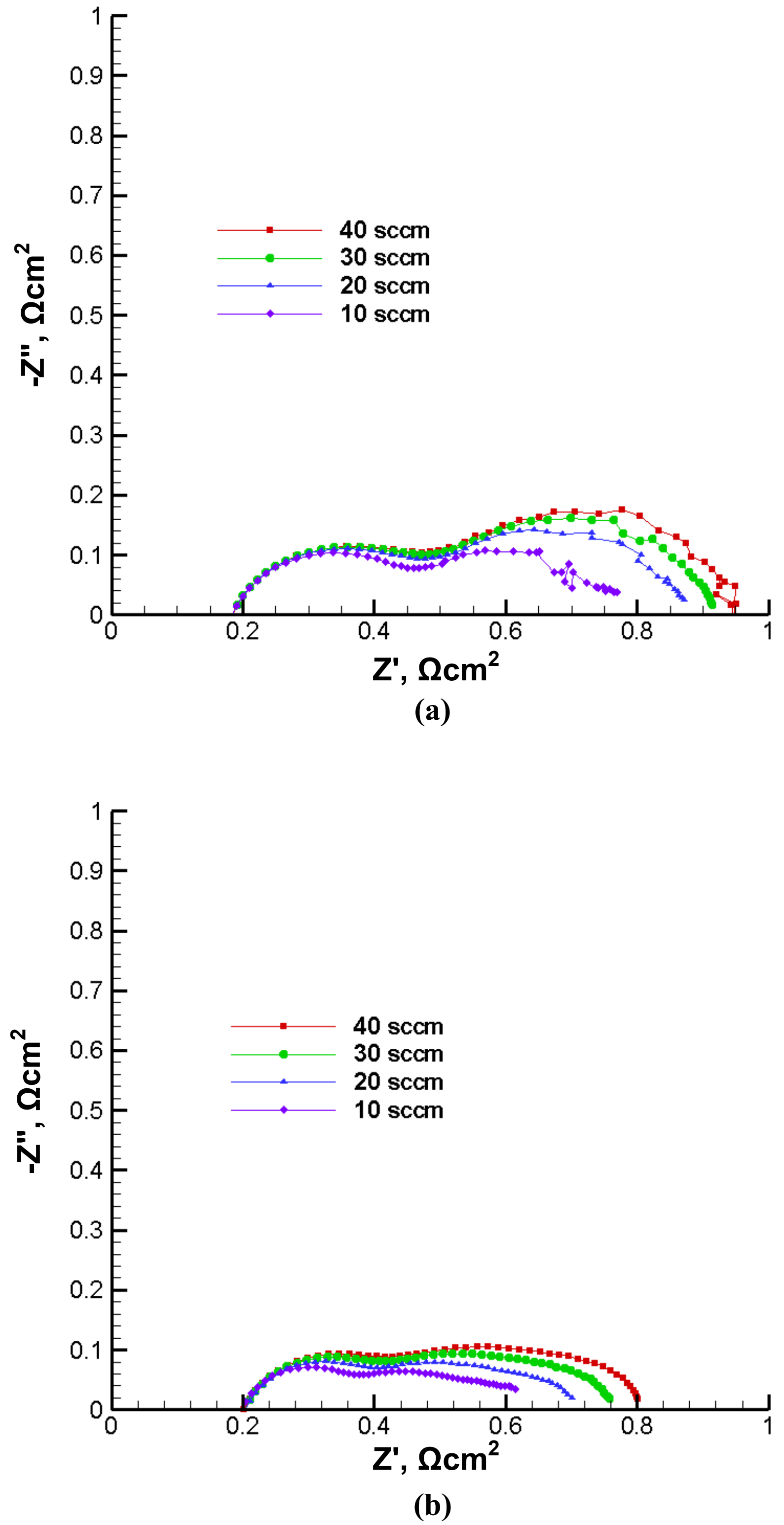

Figure 4.18 EIS characterization results (a) baseline, and (b) micromachined button cell with 150µm gap.

For the anode-supported SOFC, the cathode activation polarization and the anode activation and concentration polarization losses are significant [30, 63], as shown in Figure 4.19. The anode concentration polarization is much higher than that of the cathode because of the thick anode used.

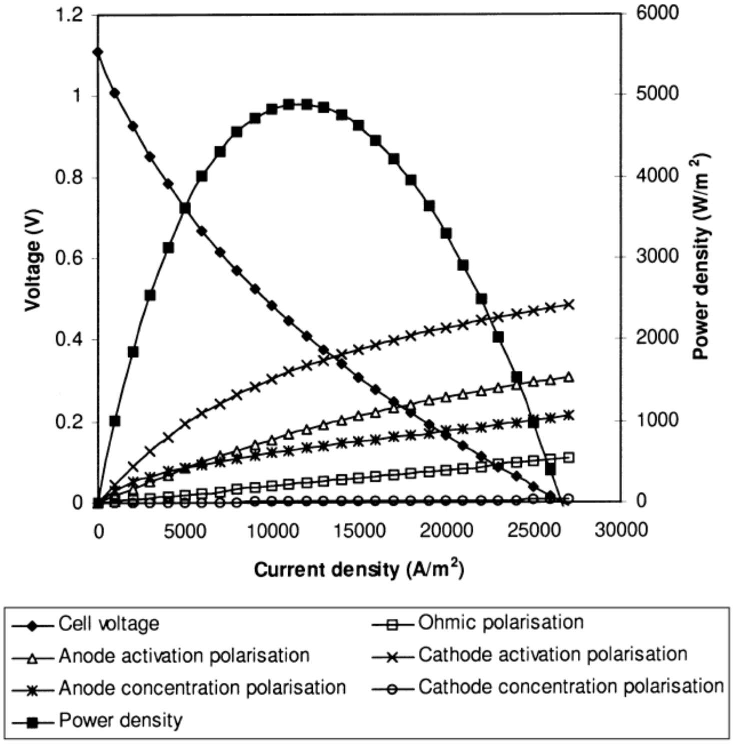

Figure 4.19 Cell voltage, polarization and power density vs. current density of typical anode-supported cells [30].

From EIS characterization results, it can be confirmed that a SOFC with micromachined pore channels enhances performance by decreasing the anode concentration polarization loss since reactants can easily reach the reaction active region and products can also be removed from the reaction active region faster through micromachined pore channels.

4.4. Modeling of Realistic Button Cell Performance

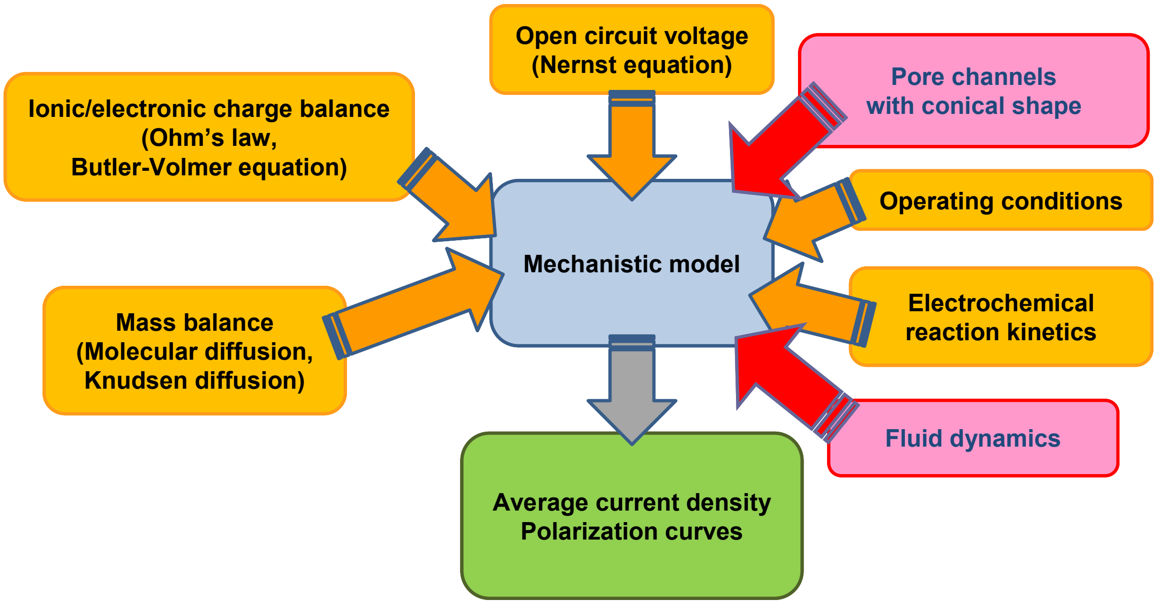

Figure 4.20 Modeling methodology.

Since pore channels with conical shapes were fabricated using laser ablation, as seen in section 4.2, performance simulations of microarchitectured SOFC button cells were modified to include conical shaped pore channels in the anode layer instead of cylindrical shaped pore channels. Furthermore, since different flow rates were applied on the side of anode layer during the performance tests, fluid dynamics, which represents momentum conservation, is considered in order to predict realistic performance of button cells. Also, the cathode material properties are changed because LSCF is used instead of LSM for the fabrication of anode-supported button cells.

4.4.1. Fluid Dynamics

In order to include fluid dynamics in the simulation, momentum as described by the Navier-Stokes equation is considered:

$$\nabla \cdot (\varepsilon \rho \mathbf{U}\mathbf{U}) = -\varepsilon \nabla P + \nabla \cdot (\varepsilon \mu_{eff} \nabla \mathbf{U}) + S_v \tag{4.1}$$

where ε is the porosity of porous electrodes, ρ is the effective density of the multi-component gas mixture, **U** is the velocity vector, P is pressure, S_v is the momentum source in the porous electrodes, and μ_{eff} is the effective dynamic viscosity of the mixture gas. Momentum is then calculated by using the ideal gas mixing law based on kinetic theory (MixKin) [64]:

$$\mu_{eff} = \sum_i \frac{y_i \mu_i}{\sum_k y_i \phi_{ik}} \tag{4.2}$$

$$\phi_{ik} = \frac{[1 + (\mu_i / \mu_k)^{1/2} (\mu_k / \mu_i)^{1/4}]^2}{[8(1 + (\mu_i / \mu_k))]^{1/2}} \tag{4.3}$$

where y_i is the mole fraction of species i, M_i and M_k are molecular weight of species i and k, respectively, and μ_i and μ_k are dynamic viscosities of species i and k, respectively.

The dynamic viscosities of the gas components are defined as a function of temperature by using Sutherland's viscosity law. Sutherland's viscosity law results from the kinetic theory by Sutherland (1893), using an idealized intermolecular-force potential. Sutherland's law with three coefficients is [65, 66]:

$$\mu = \mu_0 \left(\frac{T}{T_0} \right)^{3/2} \frac{T_0 + S}{T + S} \tag{4.4}$$

where μ_0 is the reference value of viscosity, T_0 is a reference temperature, and S is an effective temperature, the Sutherland constant, which is characteristic of the gas. The parameters of Sutherland's law for gas components are listed in Table 4.3.

Table 4.3 Coefficients of Sutherland's viscosity law for different gas components [65, 66].

Gas species	μ_0 ($kgm^{-1}s^{-1}$)	T_0 (K)	S (K)
H_2	8.411E-6	273.11	96.67
H_2O	1.703E-5	416.67	861.11

The effective density ρ in the porous medium is determined by a local volume-averaging method along with the ideal gas law:

$$\rho = \frac{P}{RT}\sum y_i M_i \tag{4.5}$$

The momentum equation has been modified to be valid for both the porous layer and the flow duct by including a source term S_v:

$$S_v = -\left(\frac{\mu_{eff}\mathbf{U}}{K} + \rho B U_i \left|\mathbf{U}\right|\right) \tag{4.6}$$

where K is the porous electrode permeability, and U_i is the velocity component in the i direction, and B is inertial coefficient, described further below. Because of the simplicity and reasonable performance within a certain range of applications, the Darcy model has been used for the majority of existing studies on gas flow in porous media. For a single-phase fully developed flow through a porous medium, the Darcy model has a linear feature, i.e., the volumetrically averaged velocity in any direction in space is proportional to the pressure gradient in that direction, and inversely proportional to the viscosity. However, the Darcy model cannot predict the viscous effect and the flow development. It also breaks down when flow velocity is not small, which is the case when the inertial forces are not negligible [67, 68]. Therefore, the Forchheimer-extended Darcy model [66-70] has been applied in this study to assess the inertial force effects.

The first term on the right-hand side accounts for the linear relationship between the pressure gradient and the flow rate in the Darcy law. The second term is the Forchheimer term, which takes into account the inertial effects, i.e., the non-linear relationship between pressure drop and flow rate. The inertial coefficient B in the second term is an empirical function depending on the microstructure of the porous medium [68]:

$$B = \frac{\varepsilon}{\sqrt{K}}\left(\frac{1.8}{\sqrt{180\varepsilon^5}}\right) \tag{4.7}$$

where ε is the porosity of porous electrodes and K is the porous electrode permeability.

The above equation is limited to gas flows in the porous anode layers, while for forced convection in the fuel channels and micromachined pore channels $S_v = 0$.

Since fluid dynamics is included in the simulation, the species conservation equation should be modified by adding a convection term, the second term on the left-hand side:

$$\nabla \cdot (-D_{i,eff} \cdot \nabla c_i + \varepsilon c_i \mathbf{U}) = R_i \tag{4.8}$$

where c_i is the concentration and R_i is the source term of mass balance and can be formulated as the reaction rate of the electrochemical and chemical reactions.

4.4.2. Model Geometry and Input Parameters

Figure 4.21 shows a cross sectional view of a SOFC button cell and fuel channels.

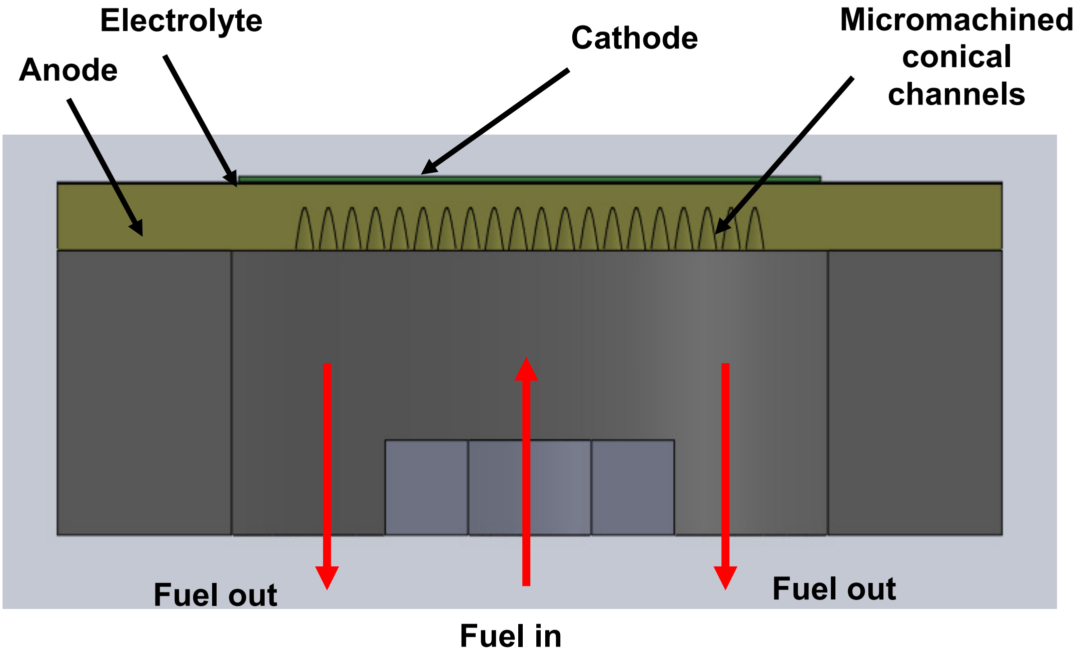

Figure 4.21 Cross sectional view of SOFC button cell and fuel channels.

To incorporate fluid dynamics in the simulation, the whole structure, instead of the unit cell, has to be considered because the fuel inlet and outlet have to be included. As seen in Figure 4.22, the pore channel array of 20 × 20 is fabricated in the center of the anode layer. Using the symmetric condition, one-eighth of the button cell is simulated, to reduce calculation time, as shown in Figure 4.22. An inner tube has 1.5785mm (0.0625in) inner diameter (ID) and 3.175mm (0.125in) outer diameter (OD) and an outer tube has 6.35mm (0.25in) ID and 9.525mm (0.375in) OD. The gap between the end of the inner tube and the bottom of anode layer is 2mm.

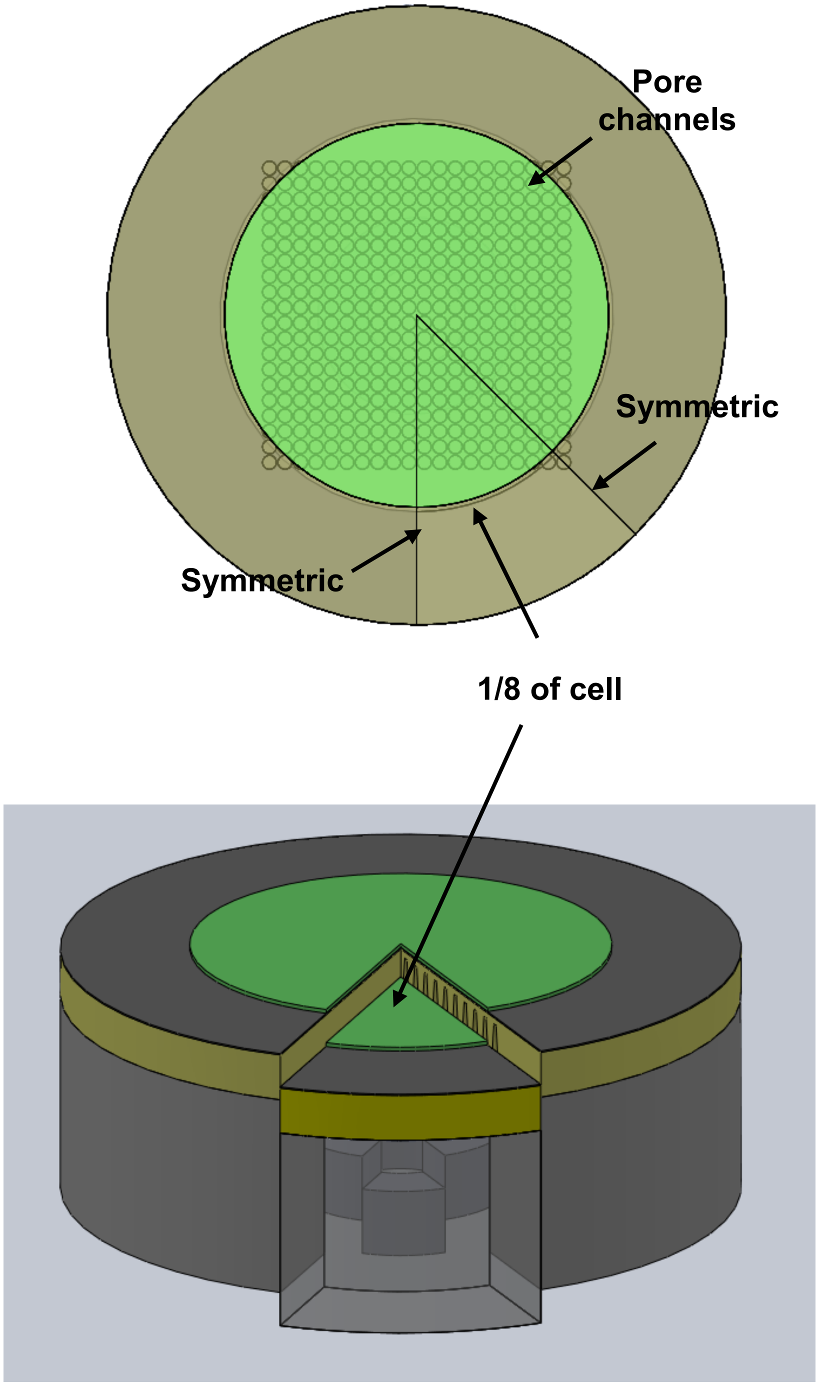

Figure 4.22 Schematic of SOFC button cell and fuel channels.

At 800ºC, YSZ has ionic conductivity of approximately 3 S/m while the ionic conductivity of SDC is approximately 10 S/m at the same temperature [71, 72]. Furthermore, the thickness of the SDC layer used as the buffer layer is 2μm, which is very thin compared with the thickness of the other layers. Therefore, a thin SDC layer is omitted in the simulation to save calculation time and to facilitate meshing. The input parameters to the model are the same as the parameters described in Table 3.1 except for the parameters shown in Table 4.4.

Table 4.4 The other input parameters to model [66, 68-70, 73-75].

Electrode porosity, ε (%)	40
Cathode exchange current density, $j_{0,ca}$ (A m^{-2})	5720
Cathode ionic conductor conductivity, σ_{ion} (S m^{-1})	0.2
Cathode electronic conductor conductivity, $\sigma_{elec,ca}$ (S m^{-1})	28000
Electrode permeability, K (m^2)	1.7E-10

The value of tortuosity is varied to obtain the best agreement between the model predictions and the experimental results. The tortuosity value of 3, used in the model predictions, is in the typical range for SOFC electrodes and provides the best agreement with the experimental results.

In Figure 4.23, the simulation results show trends similar to the experimental data described in Figure 4.16 (a). As the fuel flow rate increases from 10 to 40sccm, the measured current density also increases. It can also be observed that at the same fuel flow rate, the micromachined cells have a higher current density than the baseline cell. Furthermore, the improvement in performance of the micromachined button cell over the baseline button cell increases with a decrease in the gap between the electrolyte and the bottom of the pore channels.

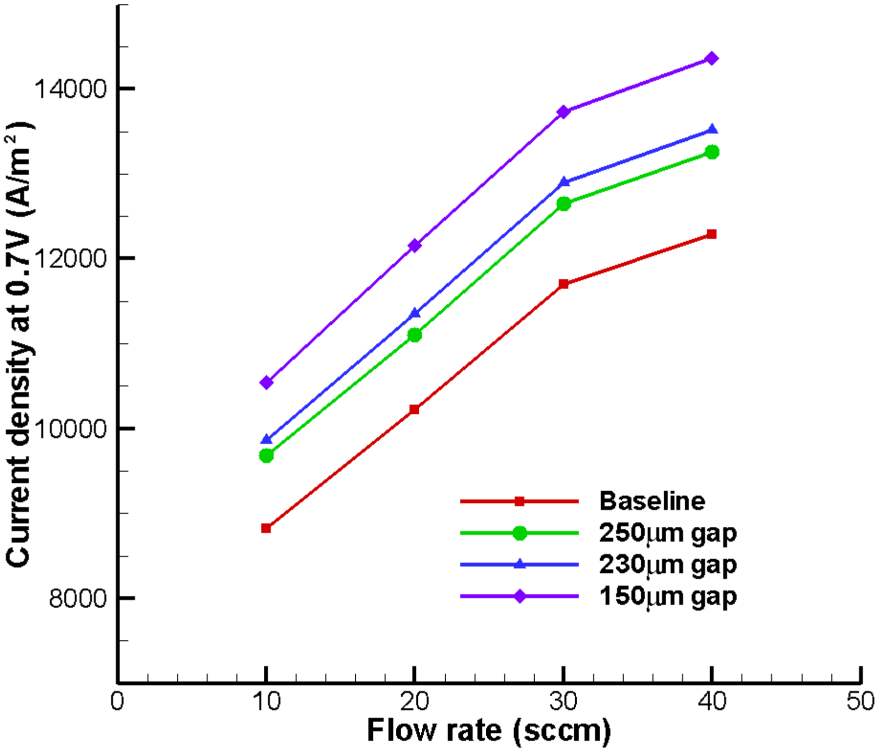

Figure 4.23 Simulation results of current density at 0.7V.

4.5. Comparison between Modeling and Experimental Results

Figures 4.24 and 4.25 compares the experimental data and the simulation results. The suffix "Ex" stands for experimental data while the suffix "Sim" stands for simulation results. It can be seen that the simulation results agree very well with the experimental data, with less than 5% difference. These results confirm the validity of the model incorporating conical pore channels, momentum transport through fluid dynamics, and material properties of the specific SOFC tested.

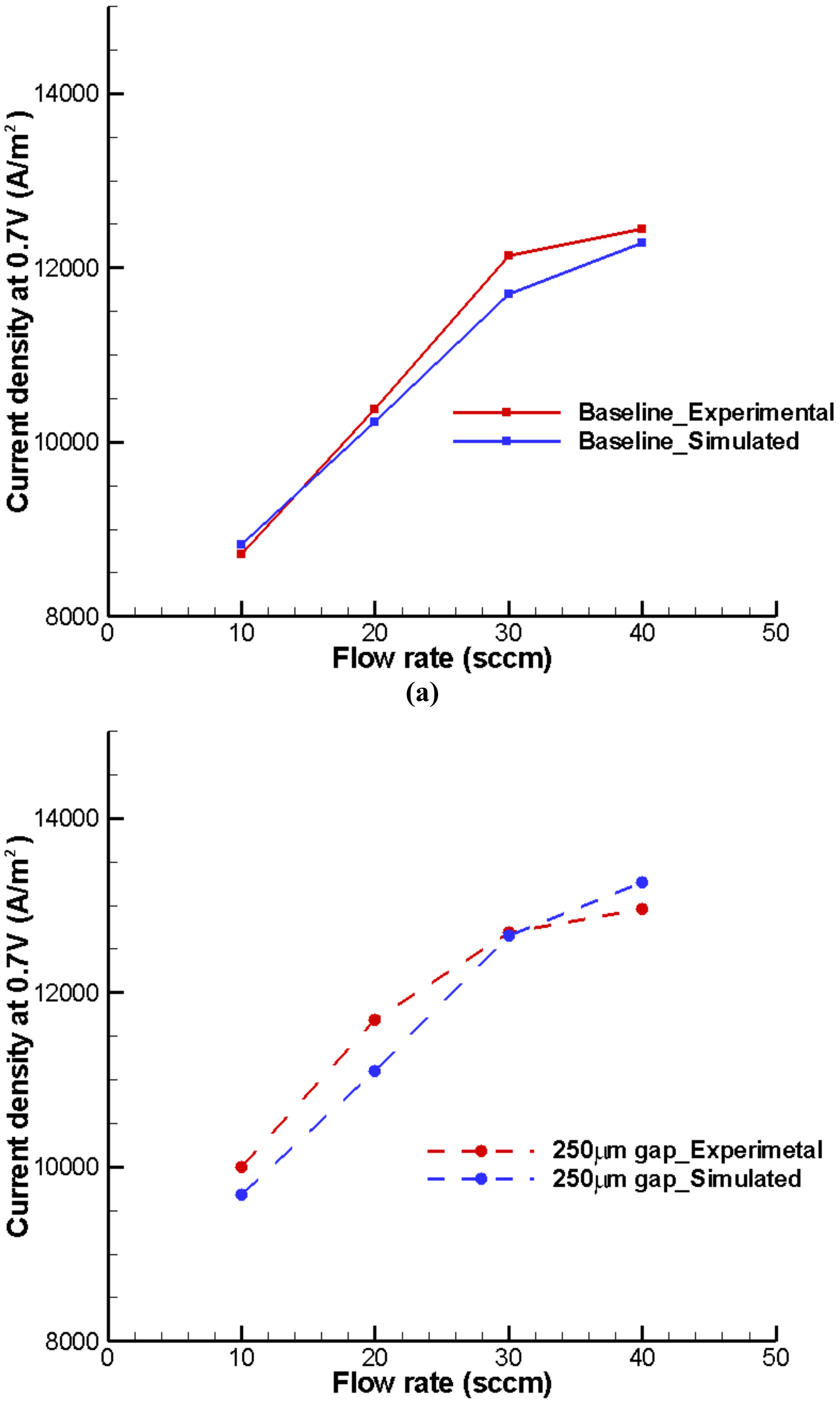

(a)

(b)

Figure 4.24 Comparison between simulation results and experimental results (a) baseline and (b) 250μm gap.

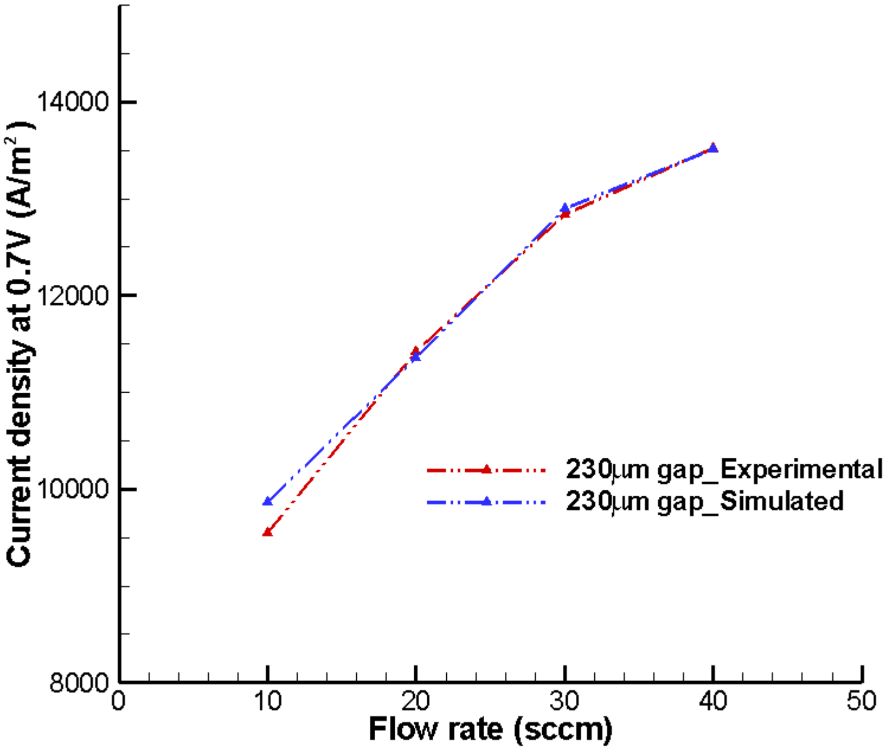

(a)

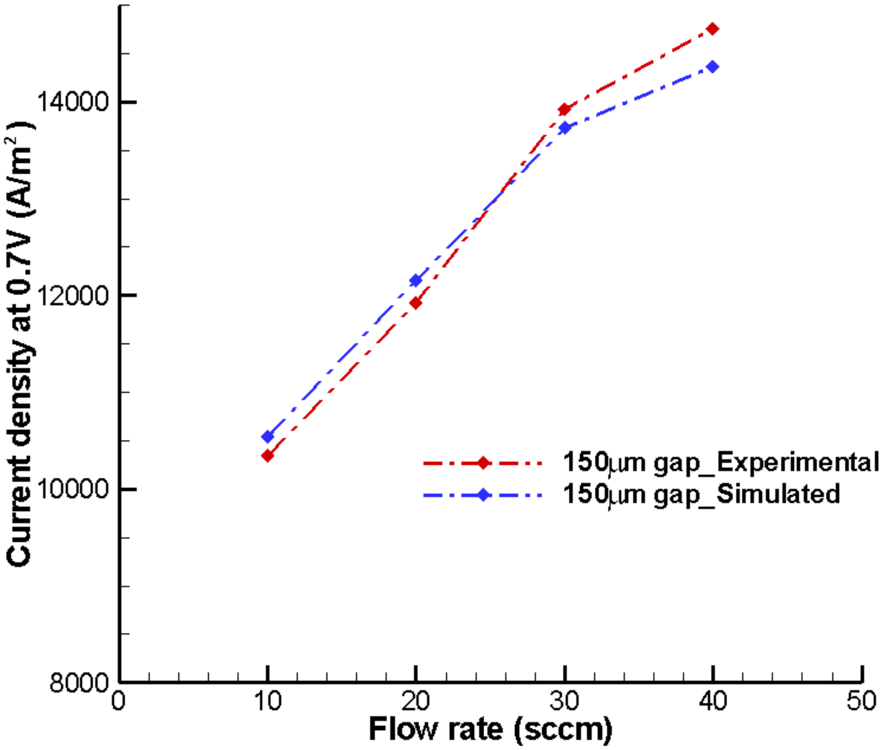

(b)

Figure 4.25 Comparison between simulation results and experimental results (a) 230μm and (b) 150μm gap.

4.6. Conclusions

In this chapter, it was proved that the performance of microarchitectured SOFCs can be improved as predicted by the fundamental computational model. A real and specific SOFC was chosen and fabricated. SOFC button cell fabrication technique using sintering and laser ablation was demonstrated. Pore size and geometry were characterized by interferometry-based surface profilometry and scanning electron microscopy. The SOFC button cell performance testing including power output performance and electrochemical impedance spectroscopy was performed. Performance simulations of microarchitectured SOFC button cells described in chapter 3 were modified to incorporate conical shaped pore channels, momentum transport through fluid dynamics, and material properties of the specific SOFC tested. The developed fundamental computational model was applied to the specific SOFC, and experimentally measured performance data was compared against the model's predictions. Simulation results agreed very well with the experimental data with less than 5% difference, further confirming the validity of the model.

CHAPTER 5

CONCLUSIONS AND FUTURE WORK

This chapter presents a summary of the research presented in this dissertation and recommendations for future work.

5.1. Summary of the Dissertation

The objective of this dissertation was to investigate and develop a new approach to enhance the performance of SOFCs. It was found that SOFC performance could be greatly improved with computationally designed microarchitectures that simultaneously optimize mass transport and electron transfer.

Chapter 2 suggested the scientific basis of the motivation to improve SOFC performance by controlling the distribution of the electrode layer materials. By controlling the distribution of the anode and cathode layer materials, both electronic conductivity and gaseous mass transport can be optimized. The concept incorporating conducting wires and designed porous channels in the electrodes was suggested for improved transport of electrons, reactant and product gases.

Chapter 3 developed the fundamental computational model-based approach to enhance the performance of SOFCs with a microarchitectured design. This involved coupled multiphysics simulation of mass transport, electrochemical charge transfer reaction, and current balance as a function of SOFC microarchitecture. The performance improvement of mircoarchitectured SOFCs by applying this computational model to a typical SOFC was investigated and predicted. An improvement of 60~70% in the current density was predicted by using porous channels in the anode layer over the baseline structure. The analysis of thermal stresses in the microarchitectured SOFC was also investigated to examine the possibility of failure due to the presence of designed pore channels.

Chapter 4 demonstrated that the performance of microarchitectured SOFCs can be improved as predicted by the fundamental computational model. As a proof of concept, a real and specific SOFC was chosen, fabricated and characterized. Performance simulations of microarchitectured SOFC button cells described in chapter 3 were modified to incorporate conical shaped pore channels, momentum transport through fluid dynamics, and material properties of specific SOFC tested. Furthermore, the developed fundamental computational model was applied to the specific SOFC and measured experimental data were well matched to simulation results.

5.2. Contributions

The contributions of this dissertation can be divided into the following categories:

1. Development of a new approach to enhance the performance of SOFCs with computationally designed microarchitectures.
2. Experimental demonstration of the improved performance of microarchitectured SOFCs with a real and specific SOFC.

5.2.1. New Approach to Enhance the Performance of SOFCs

This dissertation has offered a new and fundamental computational model-based approach to enhance the performance of SOFCs with a microarchitectured design, which has a broad range of application. This approach can be applied to other types of SOFCs, new SOFC materials, and even other kinds of fuel cells if proper material properties are known and the optimal microarchitectured SOFC structure can be determined for each type of a SOFC.

Microarchitectured SOFC designs hold the promise of potentially enhancing current generation efficiency, and therefore increasing power density over a baseline SOFC unit cell at standard operating conditions. For identical SOFC stack geometries, and considering even comparable costs of scale-up manufacturing for conventional versus microarchitectured designs, the cost of power generation in SOFCs could be reduced significantly.

In chapter 2, conducting wires and porous channels were proposed for improved transport of electrons, reactant and product gases, which can result in improved overall performance of a SOFC. However, only porous channels in the anode layer were considered for simulations. The same approach to enhancing SOFC performance with porous channels can be applied to the cathode layer.

Furthermore, a hybrid approach can be investigated. Since conducting metal wires have high thermal expansion coefficients relative to SOFC materials, the use of such wires can result in the fracture of SOFCs. Nonetheless, microarchitectured SOFC designs provide the foundation for further improvement by using a hybrid approach involving incorporation of nanoparticles or thin films of catalysts inside the designed porous channels. Such a hybrid approach has the potential for simultaneously increasing reactant gas mass transport through the electrodes and overall surface area of catalyst thereby increasing the number of sites for electrochemical reaction, and therefore the reaction rate.

Most catalysts to date have been discovered with a trial-error approach. Finding optimal catalysts by this approach is time consuming and expensive. Fortunately, a cost-effective systematic approach involving simulations followed by experimental verification has recently become possible [60]. Quantum mechanics can provide good qualitative insight into how a catalyst works. Therefore, the macroscopic model developed in this dissertation coupled with quantum mechanics will be a powerful tool to investigate this hybrid approach.

5.2.2. Experimental Demonstration of the Improved Performance of Microarchitectured SOFCs

This dissertation demonstrated that the performance of microarchitectured SOFCs can be improved as predicted by the fundamental computational model. By conventional techniques to fabricate SOFCs, anode-supported SOFC button cells were fabricated and laser ablation followed to micromachine pore channels in the button cell. However, a new fabrication method is needed for scale-up production.

5.3. Future Work

Based on the work done in this dissertation, several recommendations for future work can be made.

First, a hybrid approach involving incorporation of nanoparticles or thin films of catalysts inside the designed porous channels can be investigated. Infiltration has been widely used in surface modification of porous electrodes in SOFCs. The larger surface area and heterogeneous microstructure created by infiltration can dramatically enhance the surface catalytic behavior as well as the ionic and electronic conductivity. It is expected that surface modification with a proper catalyst has the potential to increase both performance and stability of the state-of-the-art SOFC electrodes [76-78]. During the infiltration process, more nanoparticles can be easily delivered to sites for electrochemical reaction through porous channels, as illustrated in Figure 5.1. Therefore, the reaction rate in a TPB layer will be increased and the resultant performance of the SOFC will be enhanced.

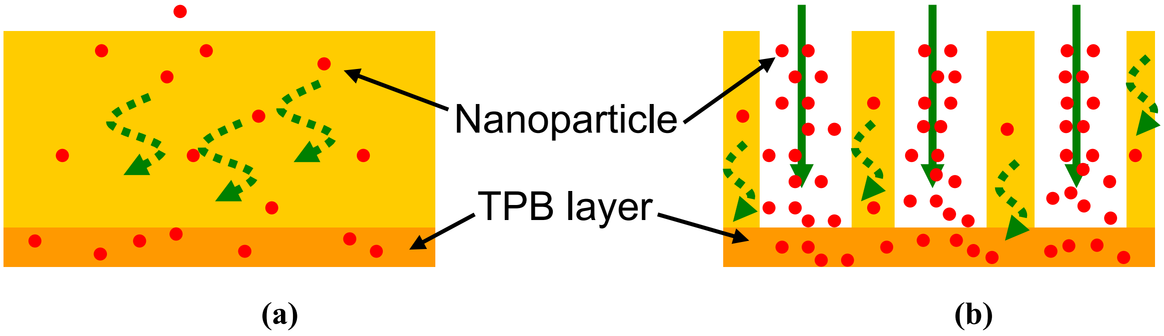

Figure 5.1 Infiltration of nanoparticles in the electrode (a) baseline, and (b) micromachined cell.

Nanoparticles or thin films of catalysts inside the designed porous channels can be selected through the quantum mechanical simulation. Once nanoparticles or thin films of catalysts inside the designed porous channels are selected, macroscale multiphysics modeling approach with properties of selected nanoparticles or thin films of catalysts can be conducted in order to determine the amount and location of nanoparticles or thin films of catalysts. For this approach, the infiltration process should be coupled with the macroscale multiphysics model developed in this dissertation and supercomputing may be needed since quantum mechanical problems consists of the equations of hundreds of atoms.

Second, the efforts to develop this technique for scale-up production are needed. Figure 5.2 shows how porous channel microarchitectures can be imparted to the electrodes by using screen printing with UV-curable electrode inks and with UV-curable or thermal phase-change, hardenable, fugitive porogen inks. Starting with a tape cast or dry-pressed, and sintered YSZ substrate, a thin (10-20μm) conformal anode layer is deposited onto the electrolyte and hardened through UV curing. Next, a thick film of fugitive ink is screen-printed in the locations of the designed porous channels and hardened by UV curing, bonding the ink to the previously cured anode layer and securing the fugitive ink pillars in place. Finally, a thick film of the anode ink is screen-printed to surround the fugitive ink pillars and to occupy all other areas of the anode layer. The anode-electrolyte assembly will be thermally processed through a careful fugitive ink burnout (or sublimation), binder burnout, and sintering process to produce the anode-supported electrolyte assembly. Subsequently, the LSM cathode layer will be screen-printed using steps similar to those described above on the other side of the YSZ electrolyte and fired to produce the SOFC assembly.

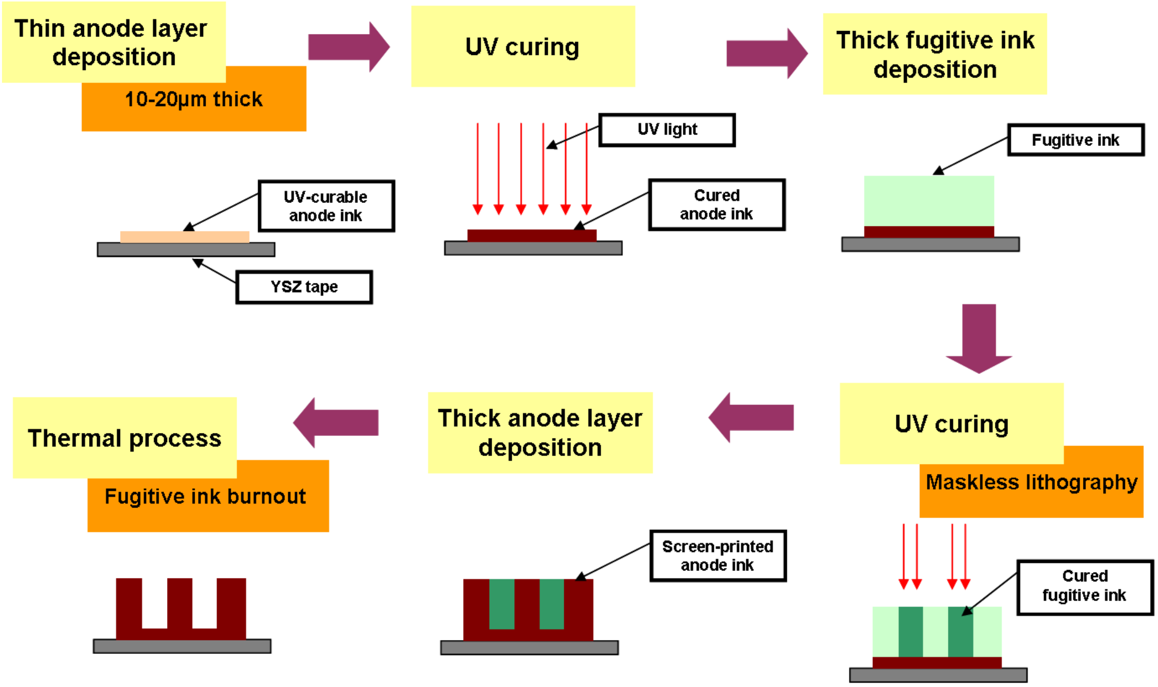

Figure 5.2 Procedure of screen printing with UV-curable inks.

This method for manufacturing microarchitectured SOFCs uses standard screen-printing technology, but with UV-curable electrode inks and fugitive porogen inks. Screen-printing is commercially available off-the-shelf (COTS) technology already in use for making planar SOFCs. This method takes advantage of UV-curable inks that can be converted to porous ceramic electrodes through binder burnout and sintering, and through the use of fugitive porogen inks that can be thermally decomposed or sublimed to leave behind well-formed microarchitectured porous channels inside the electrode structures. The design and printing of both types of inks is well understood. Therefore, manufacturing steps, complexity, and cost are bound to be reduced. Further, incorporating functionally graded materials (FGMs) into the microarchitectured SOFC designs, if desired, is relatively straightforward with additional screen-printing steps in this approach.

APPENDIX A

COMSOL MODEL REPORT

1. Table of Contents

2. Model Properties

Property	Value
Model name	Baseline
Author	Chan Yoon
Company	Georgia Tech
Department	Mechanical Eng.
Reference	
URL	
Saved date	Jul 21, 2009 5:13:34 PM
Creation date	Mar 26, 2008 12:19:13 PM
COMSOL version	COMSOL 3.5.0.603

File name: C:\Documents and Settings\Chan\Desktop\Baseline.mph

Application modes and modules used in this model:

Geom1 (3D)

- Conductive Media DC

- Conductive Media DC
- Conductive Media DC
- Diffusion
- Diffusion
- Diffusion

3. Constants

Name	Expression	Value	Description
DH2	4.887e-5	4.887e-5	Diffusion coefficient H2
DO2	1.155e-5	1.155e-5	Diffusion coefficient O2
DH2O	2.613e-5	2.613e-5	Diffusion coefficient H2O
alfa	0.5	0.5	Transfer coefficient
F	96485	96485	Faraday's constant
Temp	800+273.15	1073.15	Temperature
R	8.314	8.314	Gas constant
Vrefa	0	0	Anode reference potential
Vrefc	1.08	1.08	Cathode reference potential
CO2Bulk	2.38	2.38	Oxygen concentration at the electrode/gas chamber interface
CH2Bulk	11.03	11.03	Hydrogen concentration at the electrode/gas chamber interface
CH2OBulk	0.35	0.35	Water vapor concentration at the electrode/gas chamber interface
I0a	5300	5300	Anode exchange current density
I0c	2000	2000	Cathode exchange current density
Stpb	3.225e5	3.225e5	TPB area per unit volume
Kionc	3.34e4*exp(-10300/Temp)	2.266867	Cathode ionic conductor conductivity
Kione	3.34e4*exp(-10300/Temp)	2.266867	Electrolyte ionic conductor conductivity
Kiona	3.34e4*exp(-10300/Temp)	2.266867	Anode ionic conductor conductivity
Kelecc	(42e6/Temp)*exp(-1200/Temp)	12792.613699	Cathode electronic conductor conductivity
Keleca	(95e6/Temp)*exp(-1150/Temp)	30315.739469	Anode electronic conductor conductivity
Vcell	0.7	0.7	Cell voltage

4. Global Expressions

Name	Expression
Itransc	I0c*((CO2/CO2Bulk)*exp(alfa*nec*F*(-Velecc+Vion+Vrefc)/(R*Temp))-exp(-(1-alfa)*nec*F*(-Velecc+Vion+Vrefc)/(R*Temp)))
Itransa	I0a*((CH2/CH2Bulk)*exp(alfa*nea*F*(Veleca-Vion-Vrefa)/(R*Temp))-(CH2O/CH2OBulk)*exp(-(1-alfa)*nea*F*(Veleca-Vion-Vrefa)/(R*Temp)))

5. Geometry

Number of geometries: 1

5.1. Geom1

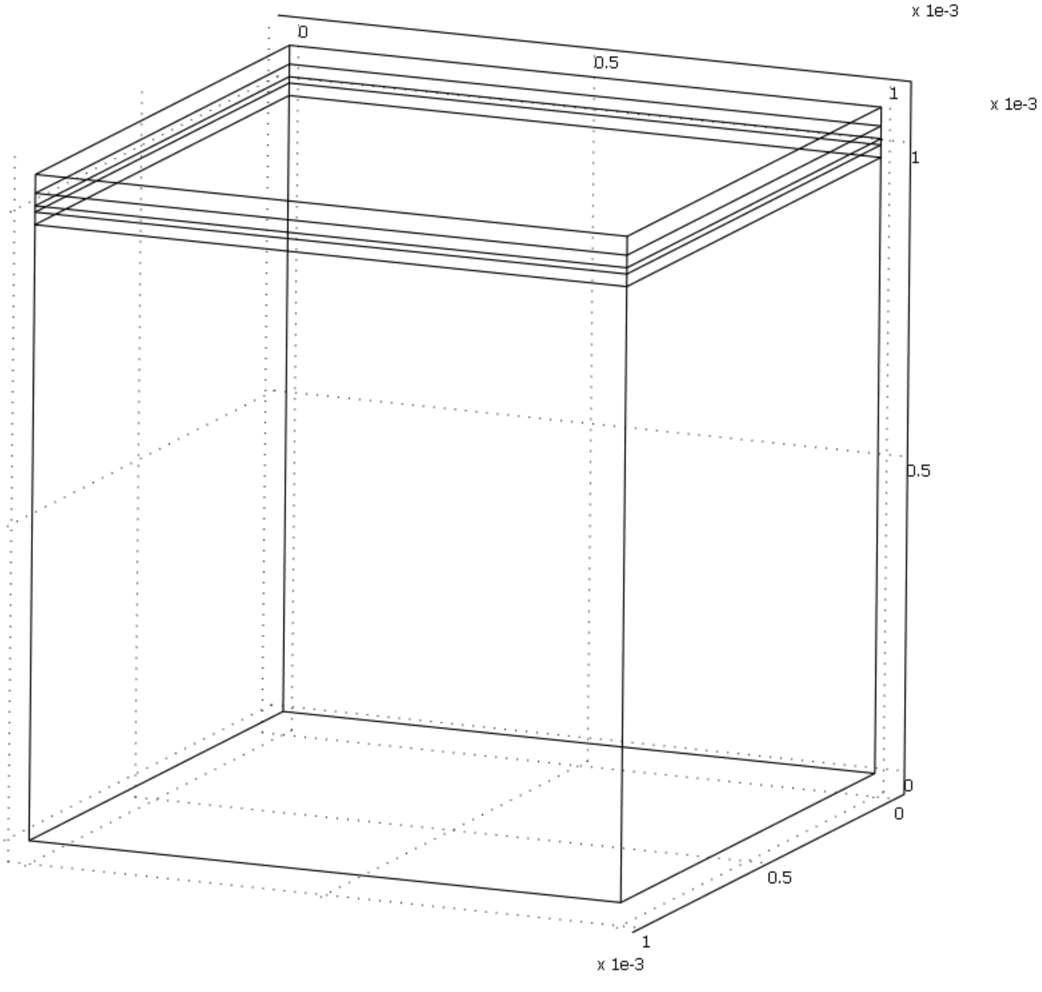

5.1.1. Point mode

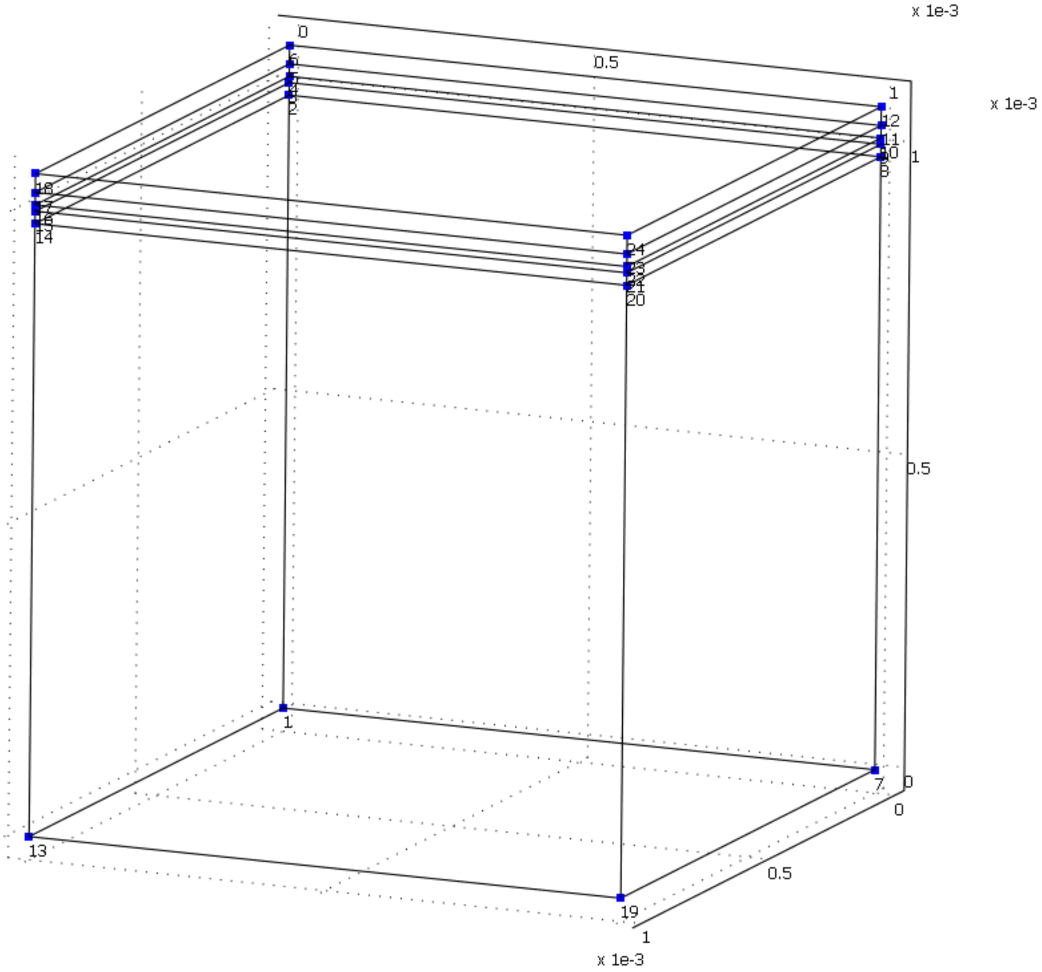

5.1.2. Edge mode

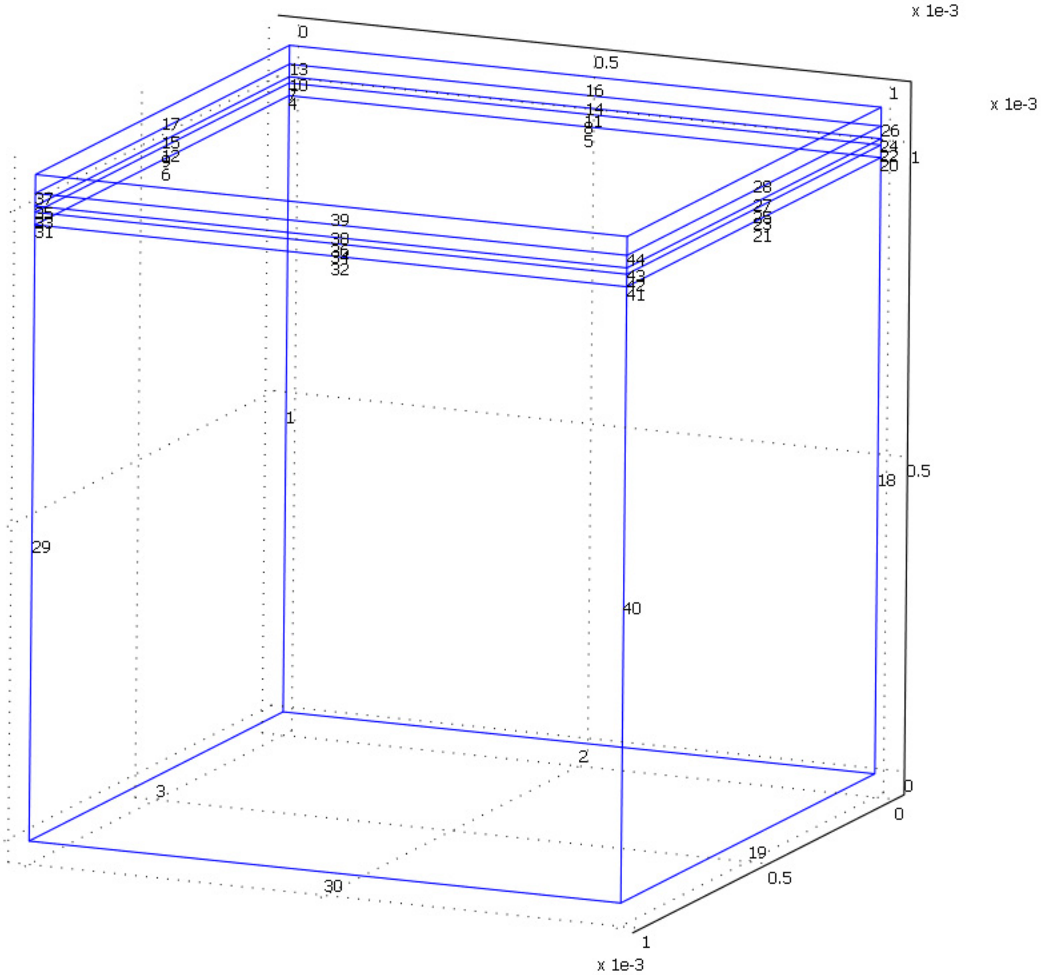

5.1.3. Boundary mode

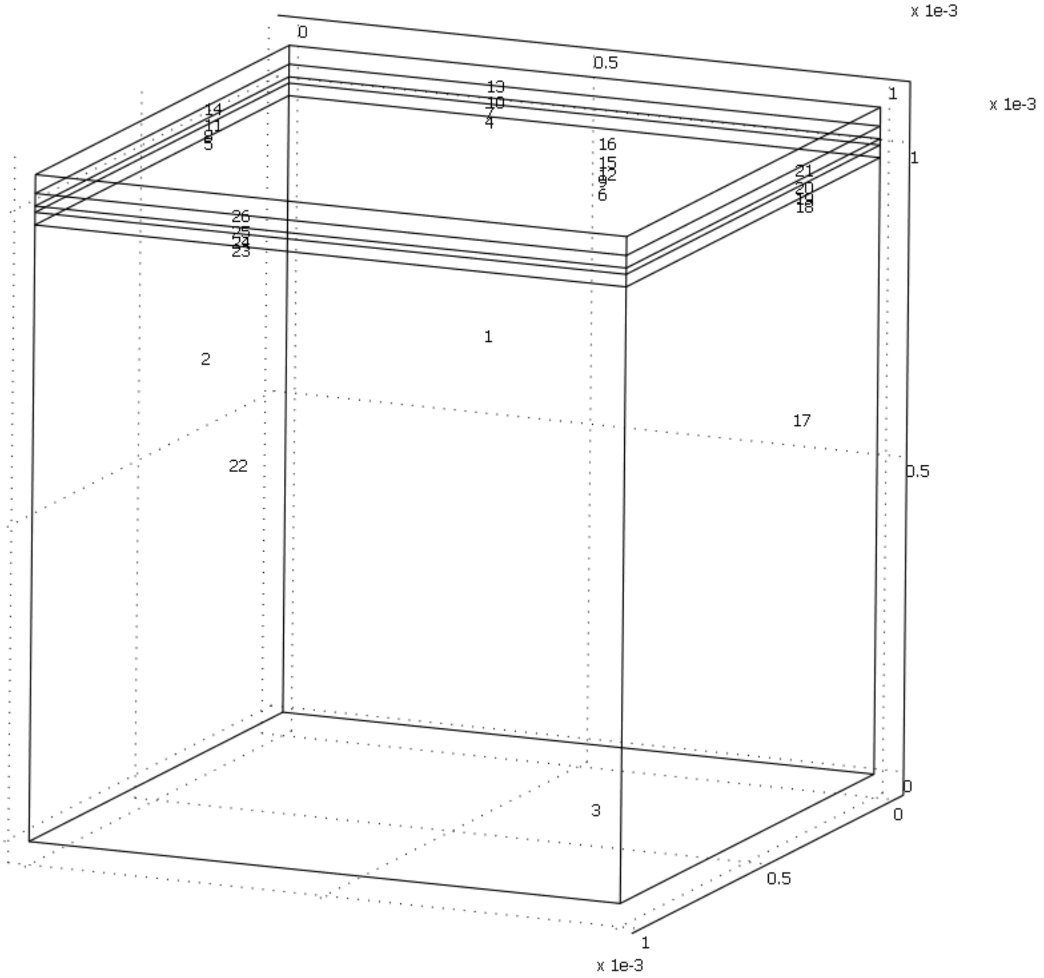

5.1.4. Subdomain mode

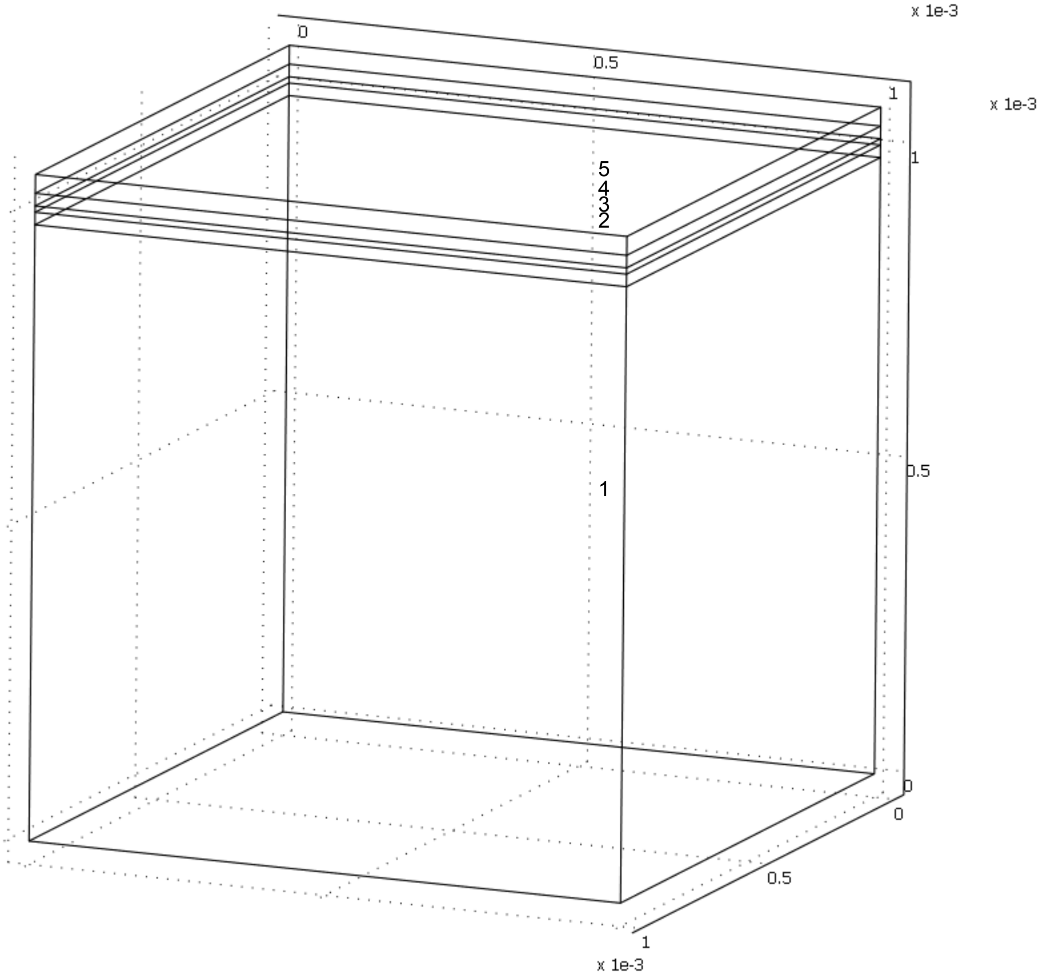

6. Geom1

Space dimensions: 3D

Independent variables: x, y, z

6.1. Mesh

6.1.1. Mesh Statistics

Number of degrees of freedom	176032

Number of mesh points	7664
Number of elements	39191
Tetrahedral	39191
Prism	0
Hexahedral	0
Number of boundary elements	15256
Triangular	15256
Quadrilateral	0
Number of edge elements	674
Number of vertex elements	24
Minimum element quality	0.1416
Element volume ratio	1.62E-5

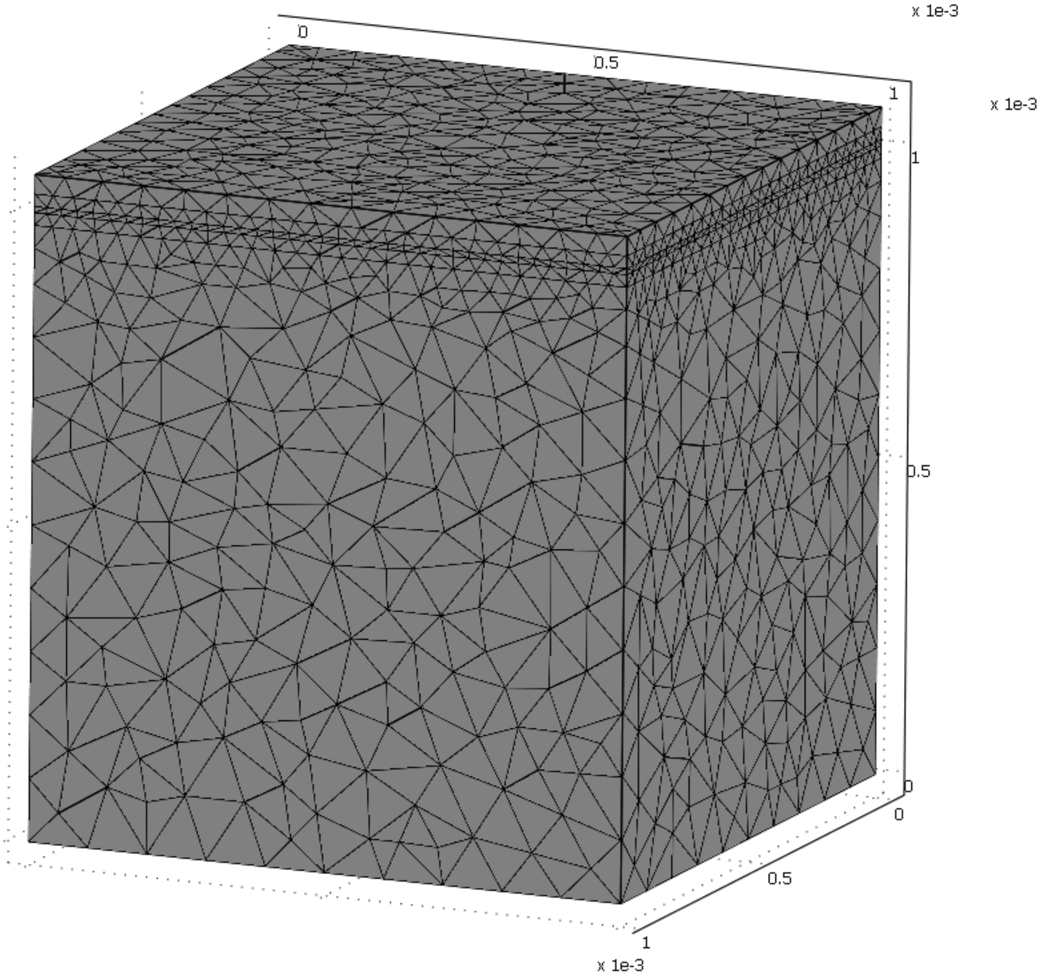

6.2. Application Mode: Conductive Media DC (ionic)

Application mode type: Conductive Media DC

Application mode name: ionic

6.2.1. Application Mode Properties

Property	Value
Default element type	Lagrange - Quadratic
Frame	Frame (ref)
Weak constraints	Off
Constraint type	Ideal

6.2.2. Variables

Dependent variables: Vion

Shape functions: shlag(2,'Vion')

Interior boundaries active

6.2.3. Boundary Settings

Boundary		1-5, 7-8, 10-11, 13-14, 16-26	6, 15	9
Type		Electric insulation	Continuity	Continuity
Normal current density (Jn)	A/m^2	0	0	**Itransa**

Boundary		12
Type		Continuity
Normal current density (Jn)	A/m^2	**Itransc**

6.2.4. Subdomain Settings

Subdomain		1	2	3
Electric conductivity (sigma)	S/m	**{Kiona,0,0;0,Kiona, 0;0,0,Kiona}**	**{Kiona,0,0;0,Kiona, 0;0,0,Kiona}**	**{Kione,0,0;0,Kione, 0;0,0,Kione}**
Temperature coefficient (alpha)	1/K	**0**	**0**	**0**
Temperature (T)	K	**0**	**0**	**0**

Reference temperature (T0)	K	**0**	**0**	**0**
Current source (Qj)	A/m^3	0	**Itransa*Stpb**	0

Subdomain		4	5
Electric conductivity (sigma)	S/m	**{Kionc,0,0;0,Kionc,0;0,0,Kionc}**	**{Kionc,0,0;0,Kionc,0;0,0,Kionc}**
Temperature coefficient (alpha)	1/K	**0**	**0**
Temperature (T)	K	**0**	**0**
Reference temperature (T0)	K	**0**	**0**
Current source (Qj)	A/m^3	**-Itransc*Stpb**	0

6.3. Application Mode: Conductive Media DC (electronic_anode)

Application mode type: Conductive Media DC

Application mode name: electronic_anode

6.3.1. Application Mode Properties

Property	Value
Default element type	Lagrange - Quadratic
Frame	Frame (ref)
Weak constraints	Off
Constraint type	Ideal

6.3.2. Variables

Dependent variables: Veleca

Shape functions: shlag(2,'Veleca')

Interior boundaries active

6.3.3. Boundary Settings

Boundary		1-2, 4-5, 17-18, 22-23	3	6, 12, 15
Type		Electric insulation	Electric potential	Continuity
Normal current density (Jn)	A/m^2	0	0	0

Boundary		7-8, 10-11, 13-14, 16, 19-21, 24-26	9
Type		Ground	Electric insulation
Normal current density (Jn)	A/m^2	0	**-Itransa**

6.3.4. Subdomain Settings

Subdomain		1	2
Electric conductivity (sigma)	S/m	**{Keleca,0,0;0,Keleca,0;0,0, Keleca}**	**{Keleca,0,0;0,Keleca,0;0,0,Keleca}**
Temperature coefficient (alpha)	1/K	**0**	**0**
Temperature (T)	K	**0**	**0**
Reference temperature (T0)	K	**0**	**0**
Current source (Qj)	A/m^3	0	**-Itransa*Stpb**

6.4. Application Mode: Conductive Media DC (electronic_cathode)

Application mode type: Conductive Media DC

Application mode name: electronic_cathode

6.4.1. Application Mode Properties

Property	Value
Default element type	Lagrange - Quadratic
Frame	Frame (ref)
Weak constraints	Off
Constraint type	Ideal

6.4.2. Variables

Dependent variables: Velecc

Shape functions: shlag(2,'Velecc')

Interior boundaries active

6.4.3. Boundary Settings

Boundary		1-5, 7-8, 17-19, 22-24	6, 9, 15	10-11, 13-14, 20-21, 25-26
Type		Ground	Continuity	Electric insulation
Normal current density (Jn)	A/m^2	0	0	0
Electric potential (V0)	V	0	0	0

Boundary		12	16
Type		Electric insulation	Electric potential
Normal current density (Jn)	A/m^2	**-Itransc**	0
Electric potential (V0)	V	0	**Vcell**

6.4.4. Subdomain Settings

Subdomain		4	5
Electric conductivity (sigma)	S/m	**{Kelecc,0,0;0,Kelecc,0;0,0, Kelecc}**	**{Kelecc,0,0;0,Kelecc,0;0,0, Kelecc}**
Temperature coefficient (alpha)	1/K	**0**	**0**
Temperature (T)	K	**0**	**0**
Reference temperature (T0)	K	**0**	**0**
Current source (Qj)	A/m^3	**Itransc*Stpb**	0

6.5. Application Mode: Diffusion (H2)

Application mode type: Diffusion

Application mode name: H2

6.5.1. Application Mode Properties

Property	Value
Default element type	Lagrange - Quadratic
Analysis type	Stationary
Frame	Frame (ref)
Weak constraints	Off
Constraint type	Ideal

6.5.2. Variables

Dependent variables: CH2

Shape functions: shlag(2,'CH2')

Interior boundaries active

6.5.3. Boundary Settings

Boundary		1-2, 4-5, 17-18, 22-23	3	6-8, 10-16, 19-21, 24-26
Type		Insulation/Symmetry	Concentration	Continuity
Inward flux (N)	$mol/(m^2 \cdot s)$	0	0	0
Concentration (c0)	mol/m^3	0	**CH2Bulk**	0

Boundary		9
Type		Insulation/Symmetry
Inward flux (N)	$mol/(m^2 \cdot s)$	**-Itransa/(2*F)**
Concentration (c0)	mol/m^3	0

6.5.4. Subdomain Settings

Subdomain		1	2
Diffusion coefficient (D)	m^2/s	**DH2**	**DH2**
Reaction rate (R)	$mol/(m^3 \cdot s)$	0	**-Itransa*Stpb/(2*F)**

6.6. Application Mode: Diffusion (H2O)

Application mode type: Diffusion

Application mode name: H2O

6.6.1. Application Mode Properties

Property	Value
Default element type	Lagrange - Quadratic
Analysis type	Stationary
Frame	Frame (ref)
Weak constraints	Off
Constraint type	Ideal

6.6.2. Variables

Dependent variables: CH2O

Shape functions: shlag(2,'CH2O')

Interior boundaries active

6.6.3. Boundary Settings

Boundary		1-2, 4-5, 17-18, 22-23	3	6-8, 10-16, 19-21, 24-26
Type		Insulation/Symmetry	Concentration	Continuity
Inward flux (N)	$mol/(m^2\cdot s)$	0	0	0
Concentration (c0)	mol/m^3	0	**CH2OBulk**	0

Boundary		9
Type		Insulation/Symmetry
Inward flux (N)	$mol/(m^2\cdot s)$	**Itransa/(2*F)**
Concentration (c0)	mol/m^3	0

6.6.4. Subdomain Settings

Subdomain		1	2
Diffusion coefficient (D)	m^2/s	**DH2O**	**DH2O**
Reaction rate (R)	$mol/(m^3\cdot s)$	0	**Itransa*Stpb/(2*F)**

6.7. Application Mode: Diffusion (O2)

Application mode type: Diffusion

Application mode name: O2

6.7.1. Application Mode Properties

Property	Value
Default element type	Lagrange - Quadratic
Analysis type	Stationary
Frame	Frame (ref)
Weak constraints	Off
Constraint type	Ideal

6.7.2. Variables

Dependent variables: CO2

Shape functions: shlag(2,'CO2')

Interior boundaries active

6.7.3. Boundary Settings

Boundary		1-9, 15, 17-19, 22-24	10-11, 13-14, 20-21, 25-26	12
Type		Continuity	Insulation/Symmetry	Insulation/Symmetry
Inward flux (N)	$mol/(m^2 \cdot s)$	0	0	**Itransc/(4*F)**
Concentration (c0)	mol/m^3	0	0	0

Boundary		16
Type		Concentration
Inward flux (N)	$mol/(m^2 \cdot s)$	0
Concentration (c0)	mol/m^3	**CO2Bulk**

6.7.4. Subdomain Settings

Subdomain		4	5
Diffusion coefficient (D)	m^2/s	**DO2**	**DO2**
Reaction rate (R)	$mol/(m^3 \cdot s)$	**-Itransc*Stpb/(4*F)**	0

7. Solver Settings

Solve using a script: off

Auto select solver	On
Solver	Stationary
Solution form	Automatic
Symmetric	auto
Adaptive mesh refinement	Off
Optimization/Sensitivity	Off
Plot while solving	Off

7.1. Direct (PARDISO)

Solver type: Linear system solver

Parameter	Value
Preordering algorithm	Nested dissection
Row preordering	On
Bunch-Kaufmann	Off
Pivoting perturbation	1.0E-8
Relative tolerance	1.0E-6
Factor in error estimate	400.0
Check tolerances	On

7.2. Stationary

Parameter	Value
Linearity	Automatic
Relative tolerance	1.0E-6
Maximum number of iterations	25
Manual tuning of damping parameters	Off
Highly nonlinear problem	Off
Initial damping factor	1.0
Minimum damping factor	1.0E-4
Restriction for step size update	10.0

7.3. Advanced

Parameter	Value
Constraint handling method	Elimination
Null-space function	Automatic
Automatic assembly block size	On
Assembly block size	5000
Use Hermitian transpose of constraint matrix and in symmetry detection	Off
Use complex functions with real input	Off

Stop if error due to undefined operation	On
Store solution on file	Off
Type of scaling	Automatic
Manual scaling	
Row equilibration	On
Manual control of reassembly	Off
Load constant	On
Constraint constant	On
Mass constant	On
Damping (mass) constant	On
Jacobian constant	On
Constraint Jacobian constant	On

8. Postprocessing

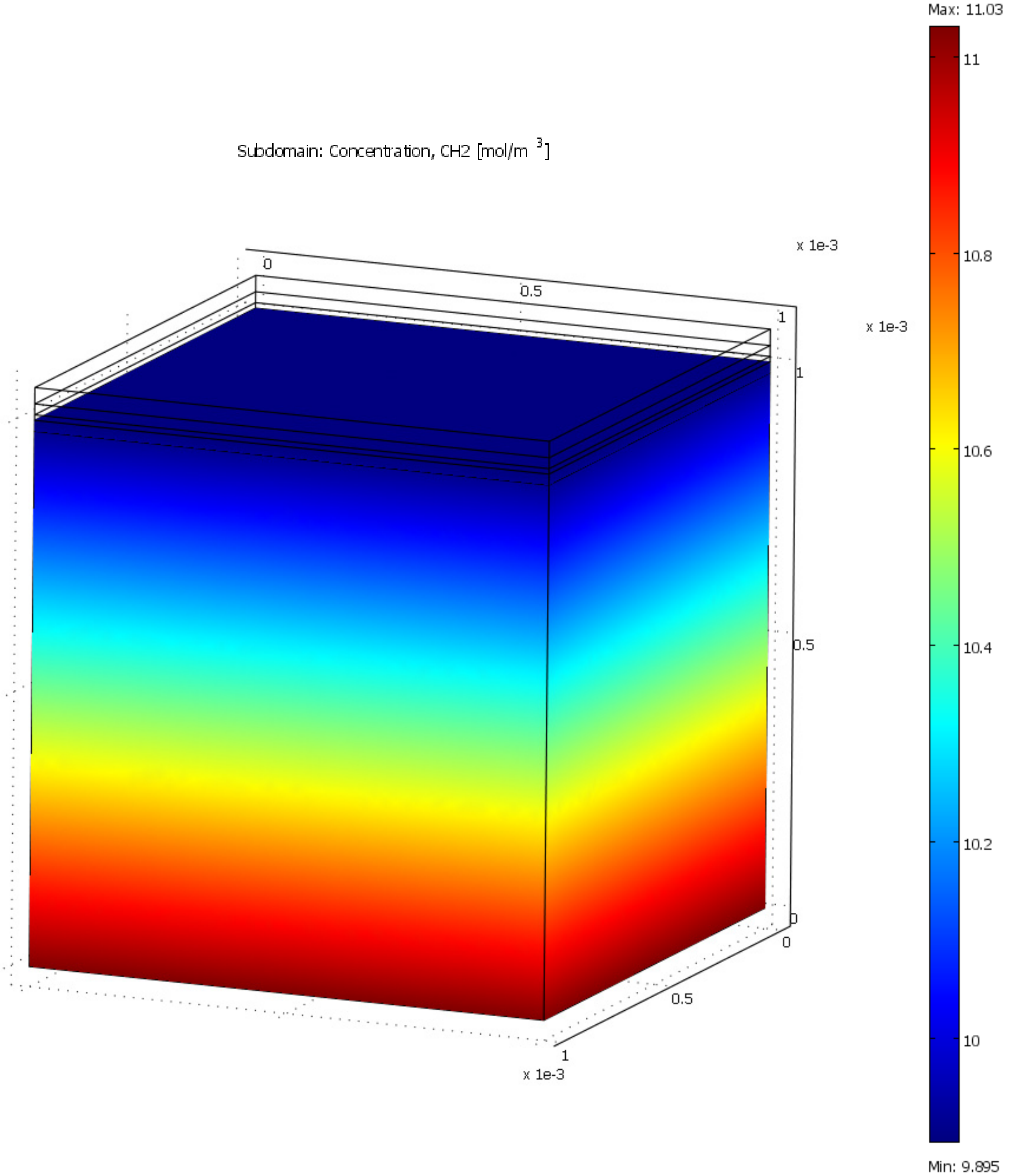

REFERENCES

[1] N. Q. Minh, "Ceramic fuel cells," *Journal of the American Ceramic Society,* vol. 76, pp. 563-588, 1993.

[2] EG&G Technical Services, Inc., "Fuel Cell Handbook (Seventh Edition)," *U.S. Department of Energy,* 2004.

[3] K. Kendall and M. Palin, "A small solid oxide fuel cell demonstrator for microelectronic applications," *Journal of Power Sources,* vol. 71, pp. 268-270, 1998.

[4] A. Heinzel, C. Hebling, M. Muller, M. Zedda, and C. Muller, "Fuel cells for low power applications," in *7th Ulmer Elektrochemische Tage, Jun 26-27 2000*, Ulm, 2002, pp. 250-255.

[5] G. J. Saunders and K. Kendall, "Reactions of hydrocarbons in small tubular SOFCs," in *7th Grove Fuel Cell Symposium, Grove VII, Sep 11-13 2001*, London, 2002, pp. 258-263.

[6] Y. Du, N. M. Sammes, G. A. Tompsett, D. Zhang, J. Swan, and M. Bowden, "Extruded tubular strontium- and magnesium-doped lanthanum gallate, gadolinium-doped ceria, and yttria-stabilized zirconia electrolytes. Mechanical and thermal properties," *Journal of the Electrochemical Society,* vol. 150, pp. 74-78, 2003.

[7] I. P. Kilbride, "Preparation and properties of small diameter tubular solid oxide fuel cells for rapid start-up," *Journal of Power Sources,* vol. 61, pp. 167-171, 1996.

[8] J. Van Herle, R. Ihringer, N. M. Sammes, G. Tompsett, K. Kendall, K. Yamada, C. Wen, T. Kawada, M. Ihara, and J. Mizusaki, "Concept and technology of SOFC for electric vehicles," *Solid State Ionics,* vol. 132, pp. 333-342, 2000.

[9] S. P. S. Badwal and K. Foger, "Solid oxide electrolyte fuel cell review," *Ceramics International,* vol. 22, pp. 257-265, 1996.

[10] A. B. Stambouli and E. Traversa, "Solid oxide fuel cells (SOFCs): A review of an environmentally clean and efficient source of energy," *Renewable and Sustainable Energy Reviews,* vol. 6, pp. 433-455, 2002.

[11] J. M. H. Gruner, "The Monolithic VPS-Fabricated SOFC," *Proceedings of the Second European Solid Oxide Fuel Cell Forum,* p. 261, 1996.

[12] A. O. Isenberg, "Energy Conversion via Solid Oxide Electrolyte Electrochemical. Cells at High Temperatures," *Solid State Ionics,* vol. 3/4, p. 431, 1981.

[13] W. Feduska and A. O. Isenberg, "HIGH-TEMPERATURE SOLID OXIDE FUEL CELL - TECHNICAL STATUS.," *Journal of Power Sources,* vol. 10, pp. 89-102, 1983.

[14] E. Wagner, "Sintering of aluminous minerals and silts of natural moulding sands in heating electron microscope. Inferences for foundry practice," Iron and Steel Institute (ISI), London, England 1943.

[15] M. Han, S. Peng, "Fabrication of Solid Oxide Fuel Cell Components," *Science Press,* p. 24, 2004.

[16] H. Nagamoto and H. Ikewaki, "Preparation of YSZ thin film on porous electrode of SOFC," *Materials Research Society Symposium - Proceedings,* vol. 547, pp. 333-338, 1999.

[17] N. Q. Minh, B. W. Chung, R. Doshi, G.R. Lear, K. Montgomery, and E. T. Ong, "Fabrication and performance of zirconia electrolysis cells for carbon dioxide reduction for mars in situ resource utilization applications," *ISRU III Technical Interchange Meeting*.

[18] N. T. Hart, N. P. Brandon, M. J. Day, and N. Lapena-Rey, "Functionally graded composite cathodes for solid oxide fuel cells," London, United kingdom, 2002, pp. 42-50.

[19] P. Holtappels and C. Bagger, "Fabrication and performance of advanced multi-layer SOFC cathodes," *Journal of the European Ceramic Society,* vol. 22, pp. 41-48, 2002.

[20] Y. Liu, C. Compson, and M. Liu, "Nanostructured and functionally graded cathodes for intermediate temperature solid oxide fuel cells," *Journal of Power Sources,* vol. 138, pp. 194-198, 2004.

[21] L. C. R. Schneider, C. L. Martin, Y. Bultel, L. Dessemond, and D. Bouvard, "Percolation effects in functionally graded SOFC electrodes," *Electrochimica Acta,* vol. 52, pp. 3190-3198, 2007.

[22] S. Zha, Y. Zhang, and M. Liu, "Functionally graded cathodes fabricated by sol-gel/slurry coating for honeycomb SOFCs," *Solid State Ionics,* vol. 176, pp. 25-31, 2005.

[23] S. Kang, P. C. Su, Y. I. Park, Y. Saito, and F. B. Prinz, "Thin-film solid oxide fuel cells on porous nickel substrates with multistage nanohole array," *Journal of the Electrochemical Society,* vol. 153, pp. A554-A559, 2006.

[24] M. Ni, M. K. H. Leung, and D. Y. C. Leung, "Micro-scale modeling of a functionally graded Ni-YSZ anode," *Chemical Engineering and Technology,* vol. 30, pp. 587-592, 2007.

[25] M. Ni, M. K. H. Leung, and D. Y. C. Leung, "Micro-scale modelling of solid oxide fuel cells with micro-structurally graded electrodes," *Journal of Power Sources,* vol. 168, pp. 369-378, 2007.

[26] Y. Wang, F. Yoshiba, T. Watanabe, and S. Weng, "Numerical analysis of electrochemical characteristics and heat/species transport for planar porous-electrode-supported SOFC," *Journal of Power Sources,* vol. 170, pp. 101-110, 2007.

[27] R. J. Kee, H. Zhu, D. G. Goodwin, and R. K. Lyon, "Solid-oxide fuel cells with hydrocarbon fuels," in *30th International Symposium on Combustion, Jul 25-30 2004*, Chicago, IL, United States, 2005, pp. 2379-2404.

[28] J. Mizusaki, S. Tsuchiya, K. Waragai, H. Tagawa, Y. Arai, and Y. Kuwayama, "Simple mathematical model for the electrical conductivity of highly porous ceramics," *Journal of the American Ceramic Society,* vol. 79, pp. 109-113, 1996.

[29] B. Todd and J. B. Young, "Thermodynamic and transport properties of gases for use in solid oxide fuel cell modelling," *Journal of Power Sources,* vol. 110, pp. 186-200, 2002.

[30] S. H. Chan, K. A. Khor, and Z. T. Xia, "Complete polarization model of a solid oxide fuel cell and its sensitivity to the change of cell component thickness," *Journal of Power Sources,* vol. 93, pp. 130-140, 2001.

[31] W. G. Bessler, S. Gewies, and M. Vogler, "A new framework for physically based modeling of solid oxide fuel cells," *Electrochimica Acta,* vol. 53, pp. 1782-1800, 2007.

[32] M. Mogensen and S. Skaarup, "Kinetic and geometric aspects of solid oxide fuel cell electrodes," *Solid State Ionics,* vol. 86-88, pp. 1151-1160, 1996.

[33] H. Fukunaga, M. Ihara, K. Sakaki, and K. Yamada, "Relationship between overpotential and the three phase boundary length," *Solid State Ionics,* vol. 86-88, pp. 1179-1185, 1996.

[34] C. W. Tanner, K.-Z. Fung, and A. V. Virkar, "Effect of porous composite electrode structure on solid oxide fuel cell performance. I. Theoretical analysis," *Journal of the Electrochemical Society,* vol. 144, pp. 21-30, 1997.

[35] A. V. Virkar, J. Chen, C. W. Tanner, and J.-W. Kim, "Role of electrode microstructure on activation and concentration polarizations in solid oxide fuel cells," *Solid State Ionics,* vol. 131, pp. 189-198, 2000.

[36] F. Zhao and A. V. Virkar, "Dependence of polarization in anode-supported solid oxide fuel cells on various cell parameters," *Journal of Power Sources,* vol. 141, pp. 79-95, 2005.

[37] M. M. Hussain, X. Li, and I. Dincer, "Mathematical modeling of planar solid oxide fuel cells," *Journal of Power Sources,* vol. 161, pp. 1012-1022, 2006.

[38] W. A. Rogers, R. S. Gemmen, C. Johnson, M. Prinkey, and M. Shahnam, "Validation and application of a CFD-based model for solid oxide fuel cells and stacks," Rochester, NY, United states, 2003, pp. 517-520.

[39] K. An and K. L. Reifsnider, "A multiphysics modeling study of $(Pr_{0.7}Sr_{0.3})MnO_{3\pm\delta}$/8 mol % Yttria-stabilized Zirconia composite cathodes for solid Oxide fuel cells," *Journal of Fuel Cell Science and Technology,* vol. 2, pp. 45-51, 2005.

[40] D. Cui, L. Liu, Y. Dong, and M. Cheng, "Comparison of different current collecting modes of anode supported micro-tubular SOFC through mathematical modeling," *Journal of Power Sources,* vol. 174, pp. 246-254, 2007.

[41] Y. Shi, N. Cai, and C. Li, "Numerical modeling of an anode-supported SOFC button cell considering anodic surface diffusion," *Journal of Power Sources,* vol. 164, pp. 639-648, 2007.

[42] Y. Shi, N. Cai, C. Li, C. Bao, E. Croiset, J. Qian, Q. Hu, and S. Wang, "Modeling of an anode-supported Ni-YSZ|Ni-ScSZ|ScSZ| LSM-ScSZ multiple layers SOFC cell. Part II. Simulations and discussion," *Journal of Power Sources,* vol. 172, pp. 246-252, 2007.

[43] M. Iwata, T. Hikosaka, M. Morita, T. Iwanari, K. Ito, K. Onda, Y. Esaki, Y. Sakaki, and S. Nagata, "Performance analysis of planar-type unit SOFC considering current and temperature distributions," *Solid State Ionics,* vol. 132, pp. 297-308, 2000.

[44] R. E. Williford and L. A. Chick, "Surface diffusion and concentration polarization on oxide-supported metal electrocatalyst particles," *Surface Science,* vol. 547, pp. 421-437, 2003.

[45] M. Ni, M. K. H. Leung, and D. Y. C. Leung, "Parametric study of solid oxide fuel cell performance," *Energy Conversion and Management,* vol. 48, pp. 1525-1535, 2007.

[46] S. Giraud and J. Canel, "Young's Modulus of Some SOFCs materials as a function of temperature," *Journal of European Ceramic Society,* vol. 28, pp. 77-83, 2008.

[47] A. Nakajo, C. Stiller, G. Harkegard, and O. Bolland, "Modeling of thermal stresses and probability of survival of tubular SOFC," *Journal of Power Sources,* vol. 158, pp. 287-294, 2006.

[48] N. M. Sammes and Y. Du, "The Mechanical Properties of Tubular Solid Oxide Fuel Cells," *Journal of Materials Science,* vol. 38, pp. 4811-4816, 2003.

[49] A. Selcuk and A. Atkinson, "Elastic Properties of Ceramic Oxides Used in Soild Oxide Fuel Cells (SOFC)," *Journal of European Ceramic Society,* vol. 17, pp. 1523-1532, 1997.

[50] A. Selcuk, G. Merere, and A. Atkinson, "The influence of electrodes on the strength of planar zirconia solid oxide fuel cells," *Journal of Materials Science,* vol. 36, pp. 1173-1182, 2001.

[51] J. LeMasters, "Thermal Stress Analysis of LCA-Based Solid Oxide Fuel Cells," *Georgia Institute of Technology,* 2004.

[52] M. Liu, D. Dong, R. Peng, J. Gao, J. Diwu, X. Liu, and G. Meng, "YSZ-based SOFC with modified electrode/electrolyte interfaces for operating at temperature lower than 650 C," *Journal of Power Sources,* vol. 180, pp. 215-220, 2008.

[53] H. Helvajian, "Microengineering aerospace systems," *Technology & Engineering,* 1999.

[54] P. Bado, W. Clark, and A. Said, "Micromachining Handbook," *Clark-MXR, Inc.,* 2007.

[55] D. Hellrung, L.-Y. Yeh, F. Depiereux, A. Gillner, and R. Poprawe, "High-accuracy micromachining of ceramics by frequency-tripled Nd:YAG-lasers," San Jose, CA, USA, 1999, pp. 348-356.

[56] F. C. Dear, J. D. Shephard, X. Wang, J. D. C. Jones, and D. P. Hand, "Pulsed laser micromachining of yttria-stabilized zirconia dental ceramic for manufacturing," *International Journal of Applied Ceramic Technology,* vol. 5, pp. 188-197, 2008.

[57] L. Shah, J. Tawney, M. Richardson, and K. Richardson, "Femtosecond laser deep hole drilling of silicate glasses in air," *Applied Surface Science,* vol. 183, pp. 151-164, 2001.

[58] N. Kuriyama and Y. Ito, "Micro-hole drilling on glass plates by femtosecond laser pulses," Osaka, Japan, 2002, pp. 567-572.

[59] E. Barsoukov and J. Macdonald, "Impedance spectroscopy: theory, experiment, and applications," *Wiley-Interscience,* 2005.

[60] R. O'Hayre, S.-W. Cha, W. Colella, and F. B. Brinz, "Fuel cell fundamentals," *John Wiley & Sons, New York,* 2006.

[61] T. Suzuki, P. Jasinski, V. Petrovsky, H. U. Anderson, and F. Dogan, "Anode supported single chamber solid oxide fuel cell in CH4-air mixture," *Journal of the Electrochemical Society,* vol. 151, pp. 1473-6, 2004.

[62] A. Bieberle, "The electrochemistry of solid oxide fuel cell anodes: experiments, modeling, and simulations," *Ph.D. thesis, Swiss Federal Institute of Technology ZÜRICH,* 2000.

[63] K. J. Yoon, S. Gopalan, and U. B. Pal, "Performance analysis of single step co-fired Solid Oxide Fuel Cells (SOFCs)," Vienna, Austria, 2009, pp. 533-542.

[64] G. Wang, Y. Yang, H. Zhang, and W. Xia, "3-D model of thermo-fluid and electrochemical for planar SOFC," *Journal of Power Sources,* vol. 167, pp. 398-405, 2007.

[65] Fluent, Inc., "Fluent 6.3 User's Guide," 2006.

[66] W. Xia, Y. Yang, and Q. Wang, "Effects of operations and structural parameters on the one-cell stack performance of planar solid oxide fuel cell," *Journal of Power Sources,* vol. 194, pp. 886-898, 2009.

[67] F. Arpino, A. Carotenuto, N. Massarotti, and P. Nithiarasu, "A robust model and numerical approach for solving solid oxide fuel cell (SOFC) problems," *International Journal of Numerical Methods for Heat and Fluid Flow,* vol. 18, pp. 811-834, 2008.

[68] J. Yuan and B. Sunden, "Analysis of intermediate temperature solid oxide fuel cell transport processes and performance," *Journal of Heat Transfer,* vol. 127, pp. 1380-1390, 2005.

[69] Q. Wang, L. Li, and C. Wang, "Numerical study of thermoelectric characteristics of a planar solid oxide fuel cell with direct internal reforming of methane," *Journal of Power Sources,* vol. 186, pp. 399-407, 2009.

[70] J. Yuan, M. Rokni, and B. Sunden, "Three-dimensional computational analysis of gas and heat transport phenomena in ducts relevant for anode-supported solid oxide fuel cells," *International Journal of Heat and Mass Transfer,* vol. 46, pp. 809-821, 2003.

[71] K. Higashinakagawa, S. Sameshima, and Y. Hirata, "Preparation, microstructures and electrical properties of a Ni/Sm-doped ceria cermet as an anode material of a solid oxide fuel cell," *Journal of Ceramic Processing Research,* vol. 5, p. 84~88, 2004.

[72] H. Yoshida, H. Deguchi, K. Miura, M. Horiuchi, and T. Inagaki, "Investigation of the relationship between the ionic conductivity and the local structures of singly and doubly doped ceria compounds using EXAFS measurement," *Solid State Ionics, Diffusion & Reactions,* vol. 140, pp. 191-9, 2001.

[73] A. Esquirol, N. P. Brandon, J. A. Kilner, and M. Mogensen, "Electrochemical characterization of $La_{0.6}Sr_{0.4}Co_{0.2}Fe_{0.8}O_3$ cathodes for intermediate-temperature SOFCs," *Journal of the Electrochemical Society,* vol. 151, pp. 1847-55, 2004.

[74] D. Stover, H. P. Buchkremer, and S. Uhlenbruck, "Processing and properties of the ceramic conductive multilayer device solid oxide fuel cell (SOFC)," UK, 2004, pp. 1107-13.

[75] H. Yakabe, M. Hishinuma, M. Uratani, Y. Matsuzaki, and I. Yasuda, "Evaluation and modeling of performance of anode-supported solid oxide fuel cell," Switzerland, 2000, pp. 423-31.

[76] N. Lifang, L. Mingfei, Z. Yujun, and L. Meilin, "$La_{0.6}Sr_{0.4}Co_{0.2}Fe_{0.8}O_3$- cathodes infiltrated with samarium-doped cerium oxide for solid oxide fuel cells," *Journal of Power Sources,* vol. 195, pp. 4704-8.

[77] X. Lou, Z. Liu, S. Wang, Y. Xiu, C. P. Wong, and M. Liu, "Controlling the morphology and uniformity of a catalyst-infiltrated cathode for solid oxide fuel cells by tuning wetting property," *Journal of Power Sources,* vol. 195, pp. 419-424.

[78] X. Lou, S. Wang, Z. Liu, L. Yang, and M. Liu, "Improving $La_{0.6}Sr_{0.4}Co_{0.2}Fe_{0.8}O_3$ - cathode performance by infiltration of a $Sm_{0.5}Sr_{0.5}CoO_3$ - coating," *Solid State Ionics,* vol. 180, pp. 1285-1289, 2009.